national accelerator laboratory

NAL-Pub-73/74-EXP
2000.000

(Lectures at the Canadian Institute
of High Energy Physics,
McGill University 1973)

INELASTIC REACTIONS AT VERY HIGH ENERGIES

G. Giacomelli*
National Accelerator Laboratory, Batavia, Illinois

October 1973

*Permanent address: University of Padova, Italy
INFN, Sezione di Bologna

Operated by Universities Research Association Inc. Under Contract with the United States Atomic Energy Commission

INELASTIC REACTIONS AT VERY HIGH ENERGIES

G. Giacomelli

October 1973

INELASTIC REACTIONS AT VERY HIGH ENERGIES

G. Giacomelli
National Accelerator Laboratory
Batavia, Illinois

1. INTRODUCTION

It has been known for many years that high-energy collisions between two elementary particles are primarily inelastic leading to the production of many particles, most of which are pions. It is in this context that the word "pionization" was first used to denote the production of many pions with small transverse momenta.

The investigation of high energy inelastic interactions may be performed either by detecting one specific reaction channel or by looking only at one or a few of the produced particles. In the first case one speaks of exclusive reactions, in the second case of inclusive reactions. The inclusive reactions may be classified according to the number of observed final state particles, that is reactions of order one if only one particle (c) is observed:

$$a + b \rightarrow c + \text{anything} \qquad (1)$$

of order two if two particles (c, d) are observed

$$a + b \rightarrow c + d + \text{anything, etc.} \qquad (2)$$

We shall be mainly concerned with the simplest inclusive reaction (1). The cross section for this reaction is the sum of the cross sections of exclusive reactions where one or more c particles are produced. As the energy increases the number of allowed exclusive reactions increases and the cross

section for each exclusive channel becomes very small. Instead the cross section for inclusive reactions should stay finite and large.

The study of the inclusive reaction (1) was always one of the first to be performed at each new accelerator. These investigations, called survey experiments, were performed using complex nuclei as targets and, with few exceptions, did not attract much theoretical interest. One of the first experiments performed with a hydrogen target was a photon production experiment (62F1), which led to a revision of the simplest picture of the statistical model.

The recent theoretical incentive to the investigation of inclusive processes may be traced to the works of Feynman (69F1) and Benecke et al. (69B1), which stressed the fact that in spite of the complexities of the inelastic processes there should be rather simple properties of the inclusive reactions, regardless of the reaction mechanism. These were the scaling property of Feynman and the limiting fragmentation hypothesis of Benecke et al.: As the energy increases the cross sections for inclusive reactions become energy independent and one may speak of cross sections which have reached their limiting values.

The experimental interest in measuring single particle spectra increased considerably with the commissioning of the CERN-ISR which made accessible an entirely new energy region, where it is energetically possible to produce many particles, thus allowing the testing of the general ideas of scaling and limiting fragmentations. The same experimental interest is evident also at the NAL accelerator. Now we have a flood of data, at least in pp collisions,

from which we have already learned the main features of high energy inelastic interactions.

At very high energies one could hope that strong interactions become simpler since threshold effects of any sort should have disappeared and one should observe the real fundamental strong interaction, which could consist in the production of many mesons. In fact a first-order description of the inelastic processes at high energies seems to be simple and some general properties, like scaling, the exponential cut-off in the transverse momentum, the factorization, the logarithmic increase of the multiplicities with energy, etc. can be easily established. But as the experiments yield more complete and more precise data it also becomes evident that most of the above-mentioned properties are, at least at the present energies, only first-order approximations and that the reality is more complex.

In a simple-minded picture one may say that at high energies one studies phenomena in a small region of space (of radius $\simeq$ 1 fermi) where one achieves extremely high-energy densities, or because of the connection between energy and mass, where the mass densities reach fantastically large values.

In the interpretation of inelastic reactions one must distinguish between produced particles, like the pions in pp reactions and scattered or leading particles, like the protons in pp reactions. One must also bear in mind that in most cases the particles really produced are not the stable ones registered by our detectors, but are massive excited states, the unstable hadronic resonances, which decay, by a cascade of decays, into the more stable particles which are detected by our apparatus.

In the literature one finds many theoretical predictions for particle production in the framework of different theoretical ideas (73C3, 73C8, 73A11). There are also many semiempirical formulae (61C1, 71C2).

Since these lectures are at the phenomenological level, we shall only discuss some of the features of the models. Our main concern will be on specific examples of particle production experiments at the ISR and NAL, to study the invariant cross sections for the simplest inclusive reactions as function of (a) the transverse momentum, (b) longitudinal variables, (c) energy (approach to scaling). A discussion on multiplicities, average transverse momenta, leading particle effects and correlations will follow. Most of the data refer to pp interactions. We shall only make a brief comparison with other types of initial states. There will be no attempt to give a complete review of all the results on inclusive reactions, but to concentrate on the results obtained at the highest energies, quoting mainly those results where a complete particle identification was made.

An extensive list of experimental references with high-energy data measured after 1971 is given in the reference section. For previous references the reader is referred to the Landolt-Börnstein compilation (72D2). Since the number of theoretical papers and also review papers on the subject is now very large, these papers will not be quoted in the literature. The reader is referred to the latest high energy conference reports, for instance (72G1), (72J1), to the theoretical review paper (73C3), and to the other lectures of this school (73A11), (73C8) for a comprehensive list of theoretical references.

2. EXPERIMENTS WITH SINGLE-ARM SPECTROMETERS

Inclusive reactions have been measured with magnetic spectrometers, total-absorption calorimeters, and bubble chambers. We shall speak of an "almost inclusive" reaction if there is any sort of requirement on observing any other product of the reaction. Figure 1 sketches three types of spectrometers.

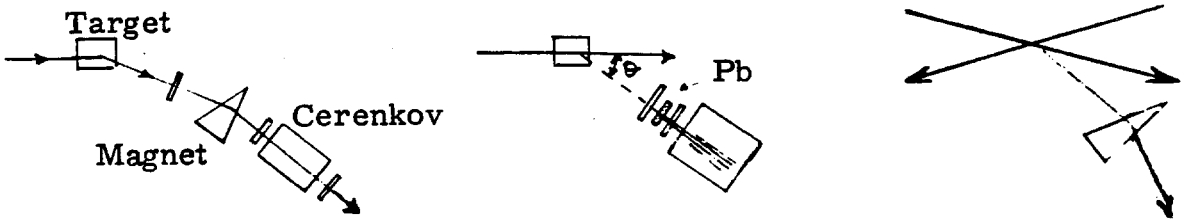

(a) (b) (c)

Fig. 1. Illustration of three types of spectrometers.
(a) A magnetic spectrometer for charged particle production at a conventional accelerator. Particles are detected in counter spark chambers and mass analyzed by time of flight and/or Cerenkov counters.
(b) A total absorption spectrometer for γ-rays. These are converted into e^+-e^- pairs in the Pb converter; the pair is counted in the subsequent counter and the electromagnetic shower is contained in the lead-glass Cerenkov counter. The anticounter placed before the converter ensures that charged particles are not counted.
(c) A magnetic spectrometer at the CERN-ISR.

In a magnetic spectrometer (Fig. 1a) the momentum p, and the angle θ of the wanted particle are measured by a combination of counters and spark chambers. The identification of the particle requires the measurement of its velocity, which may be achieved with a time-of-flight measurement at low momentum and by means of a number of Cerenkov counters at higher momenta.

Total absorption spectrometers are usually employed to detect neutral particles (Fig. 1b); these are converted into charged particles which are

counted in one or two scintillation counters; then follows a large detector (the calorimeter) where the produced particles deposit most of their energy. This method allows the simultaneous measurement of all the particles produced within an angle $\Delta\theta$. When this method is used for photons the rejection of other particles is good and the energy resolution improves with increasing energy, reaching a few per cent (or better) at the energies of the NAL accelerator.

Figure 1c illustrates the use of a magnetic spectrometer at an intersecting storage ring machine.

The bubble chamber is very useful to observe multiprong events (see Fig. 2), to measure exclusive channels and the inclusive production of K^o and

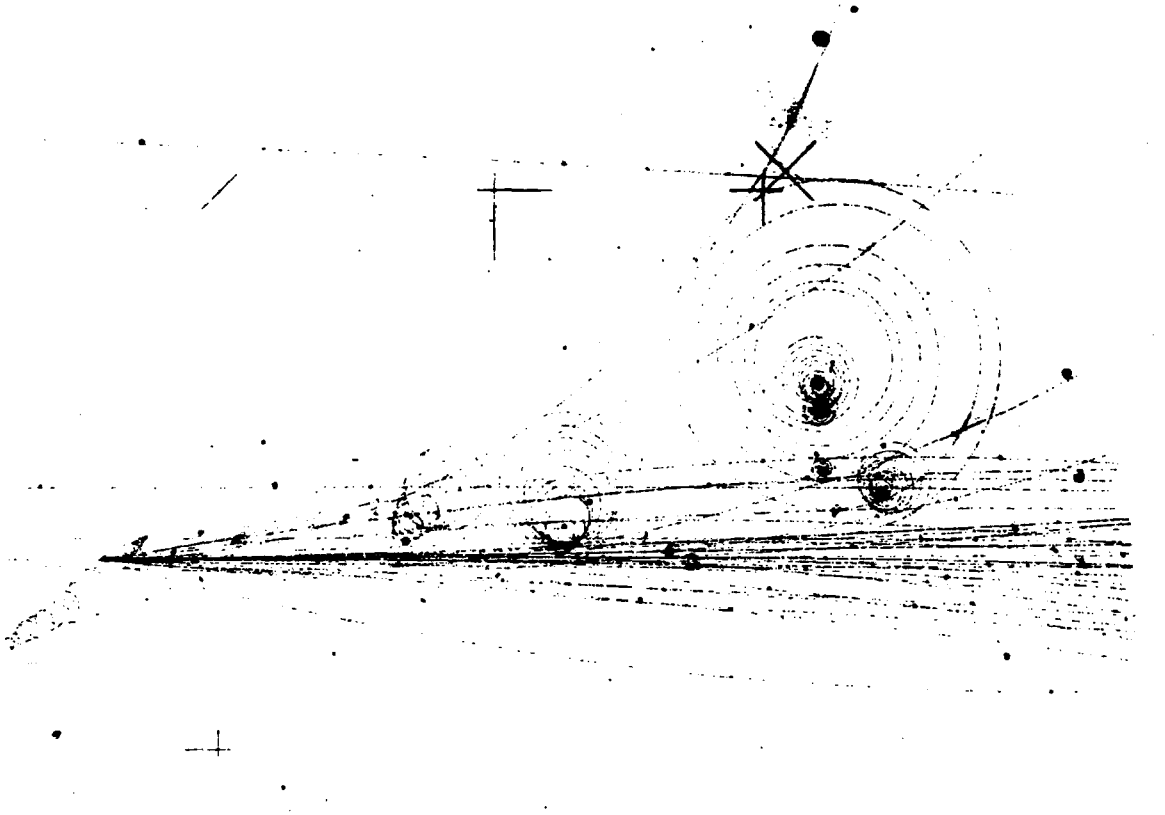

Fig. 2. A 32-prong event observed in a 400-GeV/c proton exposure of the ANL/NAL 30-in. hydrogen bubble chamber.

Λ^o. On the other hand the identification of charged particles with momenta larger than ~1 GeV/c is difficult.

2.1 Inclusive Experiments at the CERN-ISR.

2.1.1 The CERN-ISR.

Experiments at a storage ring machine are closely connected with the machine, much more so than for conventional accelerators. The ISR is made of two concentric rings--which intersect eight times--where protons are stacked and move in opposite directions. At the end of the stacking procedure there is in each ring a circulating beam in the form of a ribbon with approximate transverse dimensions of 3-5 cm horizontally and 0.5-0.8 cm vertically. As shown in Fig. 3 collisions can take place in eight intersecting regions, which are in principle independent of one another. The two beams collide at an angle of 15°, so that the source of the collisions has a "diamond" shape. As indicated in Table I, the ISR is operated for physics at four energies which cover the range between 23 and 53 GeV in the center of mass. The top energy of 62 GeV requires acceleration of the protons in the ISR itself and it became operational only recently.

The total collision rate in each intersection is given by

$$N = L\,\sigma_{tot} \qquad (3)$$

where σ_{tot} is the pp total cross section and L is the luminosity. Since $\sigma_{tot}(pp) \simeq$ 39 mb and $L \simeq 3 \times 10^{30}$ cm^{-2} sec^{-1} the total collision rate is about 10^5 interactions per second per intersection region. The average multiplicity

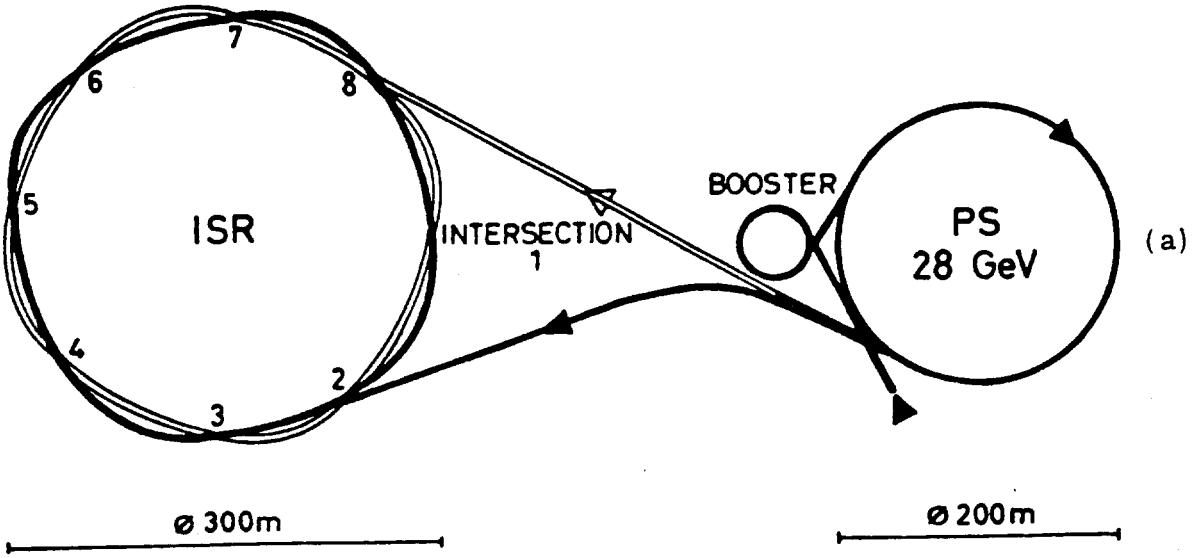

(a)

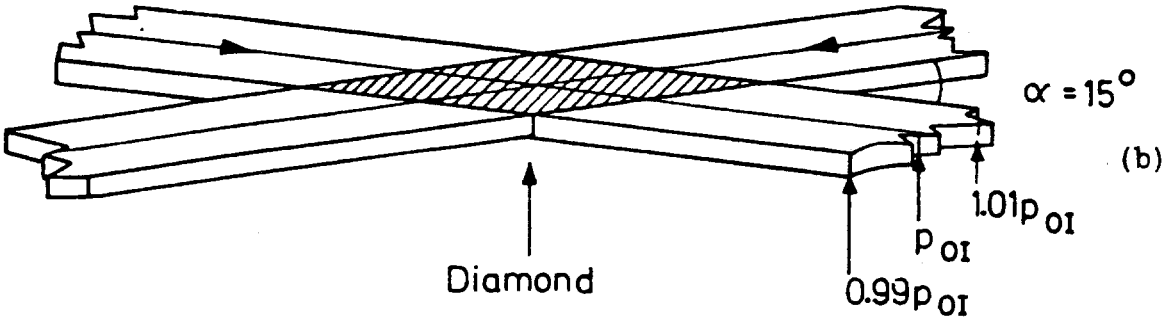

(b)

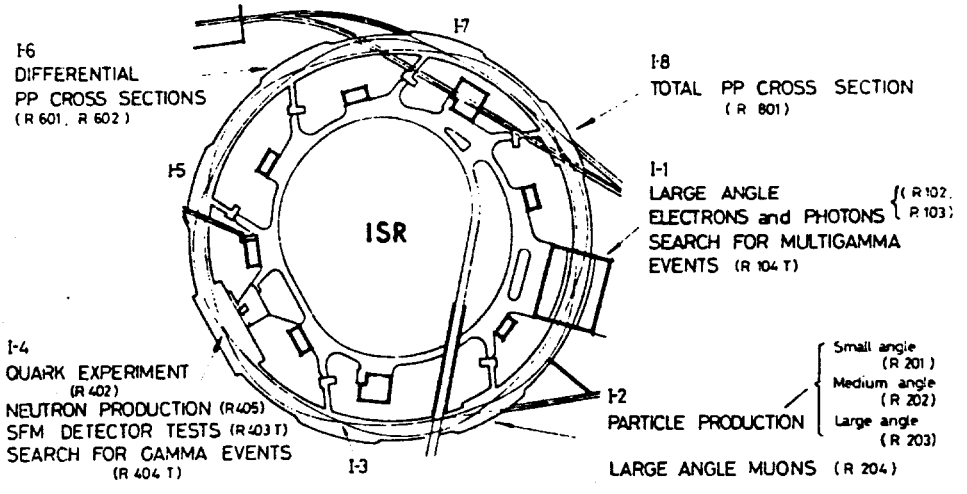

(c)

Fig. 3(a). A schematic plan of the CERN-ISR showing (c) the arrangement of experiments in the eight-intersection regions (I-1 ÷ I-8); (b) illustrates the intersecting of the two proton beams.

Table I. Some Parameters of the CERN-ISR and Present Operation for Physics.

Beam momenta		11 - 31 GeV/c, $\Delta p/p \approx 2\%$
Crossing angle		15°
Beam lifetime	2A	~ 1 month
	10A	~ 1 day
Average pressure		$\lesssim 2 \times 10^{-10}$ torr
Pressure in intersections		$\lesssim 5 \times 10^{-11}$ torr
Design luminosity		4×10^{30} cm^{-2} s^{-1}
Transverse beam dimensions	horizontal	~ 3-5 cm
	vertical	~ 0.5 cm

Beam Momenta	c.m. Energy	$s = E_{cm}^2$	Equivalent Lab. Momenta	Present Average Luminosities
GeV/c	GeV	GeV^2	GeV/c	10^{30} cm^{-2} s^{-1}
11.8/11.8	23.4	548	291	0.3
15.3/15.3	30.4	924	491	1
22.4/22.4	44.4	1971	1053	3
26.5/26.5	52.6	2767	1474	3
31.4/31.4	62.3	3881	2062	0.3

of the produced particles at E_{cm} = 53 GeV is 18; thus about 2×10^6 particles/sec are produced. The measurement of the luminosity is one of the most crucial measurements at the ISR, since on it depends the knowledge of the absolute values of the cross sections.

Finally it should be noted that since the two beams collide at a small angle (15°), the ISR laboratory system is, to a good approximation, equal to the center-of-mass system.

2.1.2 The Spectrometers at the CERN-ISR.

A schematic plan of the ISR is shown in Fig. 3, with the eight intersection regions, six of which are used for physics at the present time. This review deals mainly with the results obtained from three single-arm spectrometers in Intersection 2 and two spectrometers in Intersection 1. In fact there have been nine experiments on inclusive reactions, four with magnetic spectrometers, one with a muon calorimeter, three with photon total absorption lead glass counters, and one with a neutron calorimeter.

The three spectrometers in Intersection 2 cover almost the whole angular range. The wide-angle spectrometer installed by the British-Scandinavian collaboration is shown in Fig. 4. It consists of a large platform

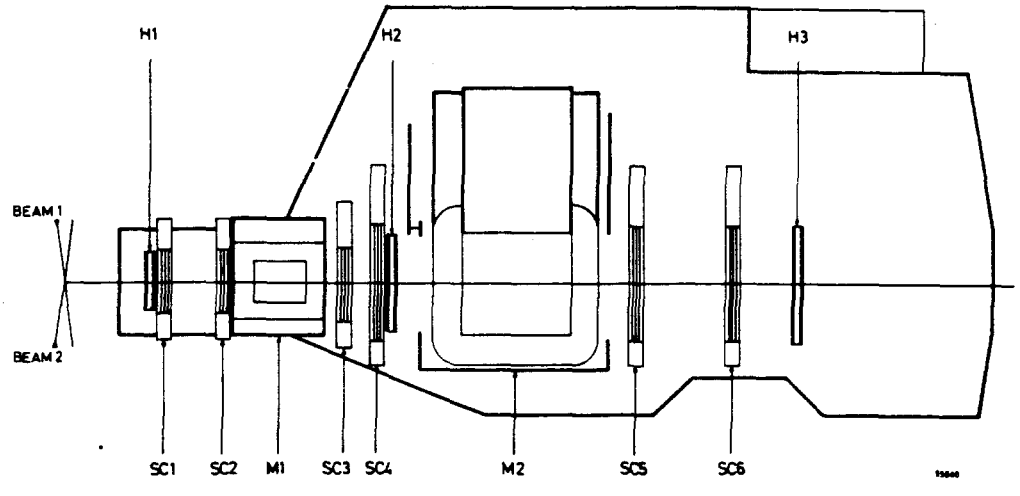

Fig. 4. Plan view of the wide-angle spectrometer in I-2 showing the two bending magnets M_1 and M_2 used in conjunction with the magnetostrictive wire spark chambers SC_{1-6} and scintillation counter hodoscopes H_1-H_4 (73A5).

which can be rotated within the angular range of 30-90°. With the configuration shown, momentum analysis was made with two bending magnets using wire spark chambers for track reconstruction. Particle separation π, K, and

proton was possible up to about 1.5 GeV/c by time of flight. For particle identification at higher momenta the configuration was changed to include two gas Cerenkov counters.

The intermediate-angle spectrometer shown in Fig. 5, used by an

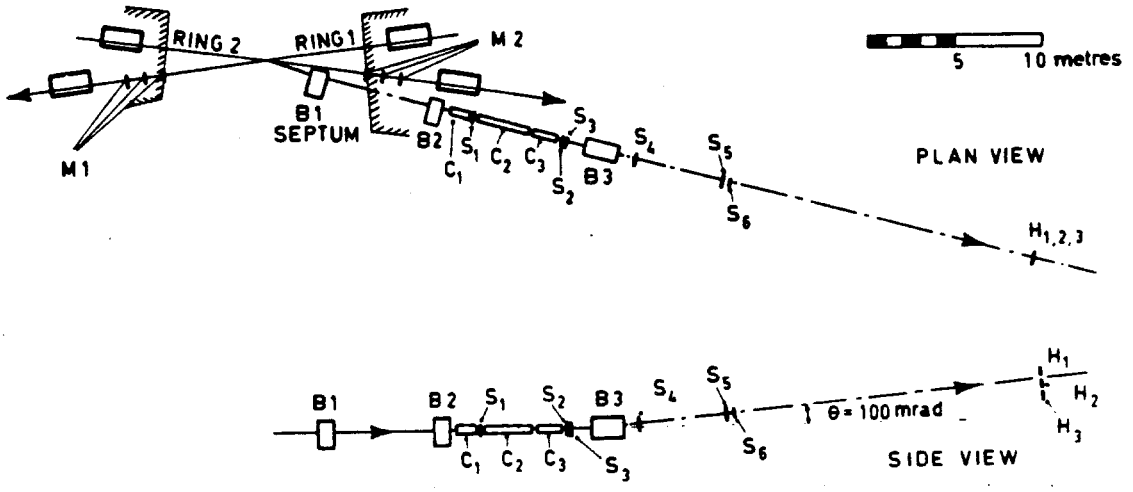

Fig. 5. Plan and elevation view of the medium-angle spectrometer; B_1 is a septum magnet; B_2 is a bending magnet used to compensate the effect of B_1; B_3 a bending magnet for momentum determination; S_{1-6} are triggering scintillation counters and $H_{1,2,3}$ a counter hodoscope (72B2).

Argonne-Bologna-CEN-CERN-Michigan-Riverside collaboration, was the simplest. It covered the angular range 80-350 mrad by adjustment of the septum magnet B_1 and magnet B_2. The momentum determination was made using the magnet B_3 which bent in the vertical plane. Three gas Cerenkov counters C_{1-3} were used for particle identification; also time-of-flight data was taken. Kaon-spectra were measured with a shortened spectrometer up to S_6 to avoid large corrections for decays. Background coming from beam-gas collisions was estimated taking data with only beam 2 in the ISR; it was small (2-20%) because of the very low pressure at the intersection region and the directionality of the spectrometer.

The small-angle spectrometer of the CERN-Holland-Lancaster-Manchester collaboration is shown in Fig. 6. This spectrometer is mounted above the machine magnets in order to reach small angles and to make use of the small ISR beam height. Measurements have been made in the angular range of 35-200 mrad. The bending magnets BM_{1-3} provide a momentum measurement with $\Delta p/p \leq \pm 1\%$ and the three Cerenkov counters together with time-of-flight measurements allow particle separation over a wide-momentum range.

In intersection region I1 there is now what may be called a second generation double-arm spectrometer resulting from the combination of the equipment of two groups [CERN-Columbia-Rockefeller (Fig. 7)-Saclay collaboration]. The spectrometer has two simple bending magnets placed at 90° with respect to the circulating beams, on each side of the intersection. The magnets are complemented on each side by two arrays of lead glass Cerenkov counters, the first being a dE/dx array, the second a total absorption calorimeter. The equipment covers a considerable solid angle and allows the detection of γ-rays and electrons besides $\pi^{\pm}$, $K^{\pm}$, p, and $\bar{p}$.

Intersection region I4 is now surrounded by a large number of wire proportional chambers immersed in the dipole field of the Split Field Magnet (Fig. 8). The chambers contain a total of about 80,000 wires and the equipment may be triggered in a variety of ways by several experimenters. The reconstruction of the paths of the charged particles in the relatively complex field of the magnet will require a considerable amount of computer time. The equipment has been just put into place and is being tested now. It clearly

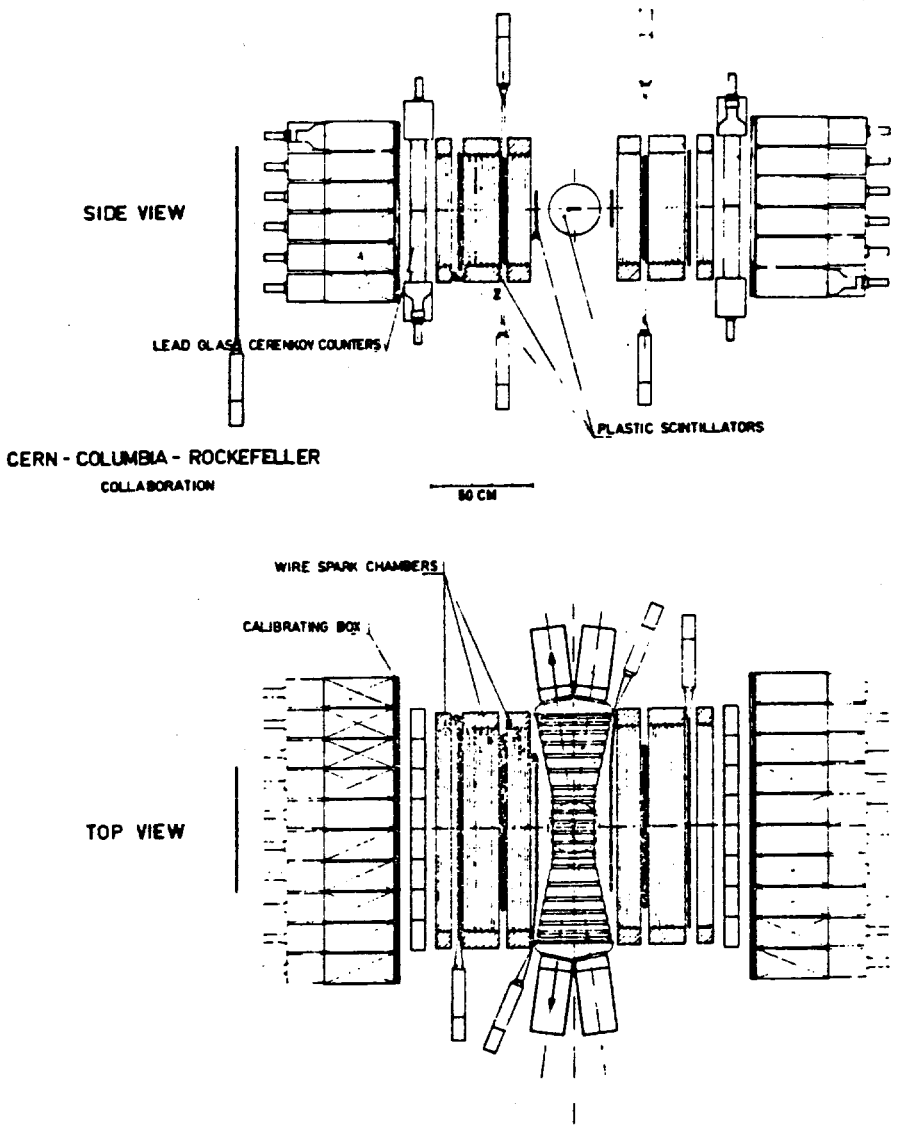

Fig. 7. Plan and elevation views of the double-arm spectrometer in I-1. The smaller size lead glass Cerenkov counters are for dE/dx measurements, while the larger blocks are for total energy measurements (73C5).

represents a second- or third-generation step and can allow much more than the study of simple inclusive reactions.

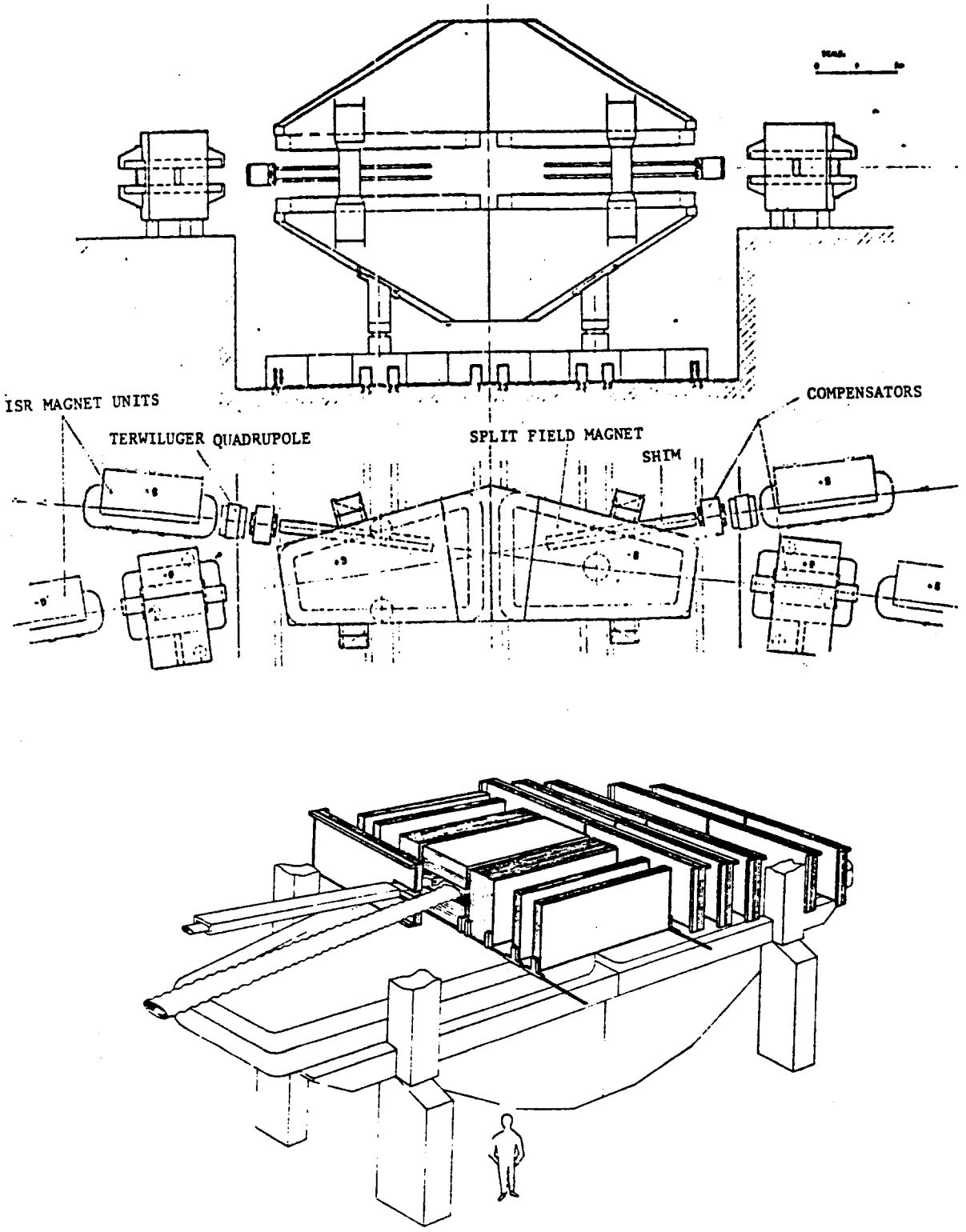

Fig. 8. General view of the split-field magnet located at intersection I-4 of the CERN-ISR.

In Fig. 9 it is shown a neutron calorimeter employed with success at the CERN-PS and at the ISR. The neutrons are converted into **charged particles** in the converter, which is followed by a lead block where γ-rays are absorbed (73E1).

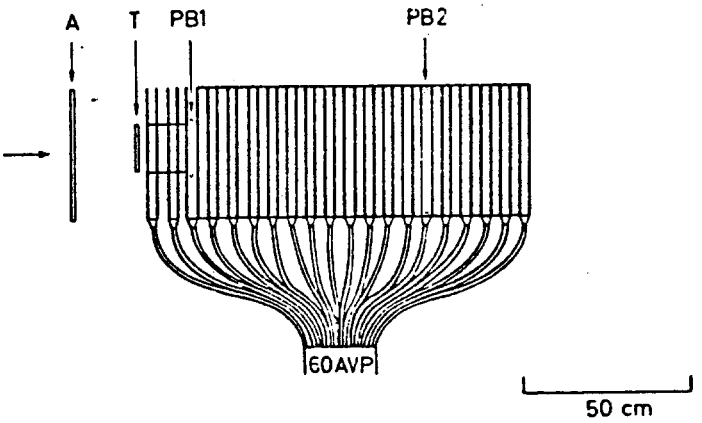

Fig. 9. The neutron calorimeter used by the CERN-Karlsruhe collaboration (73E1), (73E2).

2.2 Inclusive Experiments at NAL.

A large number of single-arm spectrometers (including survey-type experiments) are at various stages of construction or of data taking at NAL. Figure 10 shows the focusing spectrometer facility which is being installed in the Meson Area of the 200-400 GeV NAL accelerator. The spectrometer will have a momentum resolution of ±0.03% and a solid-angle acceptance of 60 μsr at 60 GeV/c and 15 μsr at 200 GeV/c. Changes in the production angle of particles accepted by the spectrometer will be accomplished by steering some combination of the incident and outgoing beam elements. Particle identification is achieved with differential and threshold Cerenkov counters in both the incident beam and the spectrometer. A comparison of this NAL spectrometer

DESIGN PARAMETERS FOR FOCUSSING SPECTROMETER

Momentum Range	**20 to 200 GeV/c**
Momentum Bite	**± 2.0%**
Momentum Resolution at 200 GeV/c	± 0.03% Δp/p
Momentum Dispersion at p focus	3.0 cm per %
Angular Resolution	± 0.1 mrad
Horizontal Acceptance	± 5.0 mrad
Vertical Acceptance	± 1.0 mrad
Solid Angle at 200 GeV/c	~ 15 μsterad
(at 60 GeV/c)	~ 40 μsterad)
Angular Divergence at Diff. Č	± 0.2 mrad
Expected Beam Spot Size at Target	1.0 mm diameter
Overall Spectrometer Length	150 m

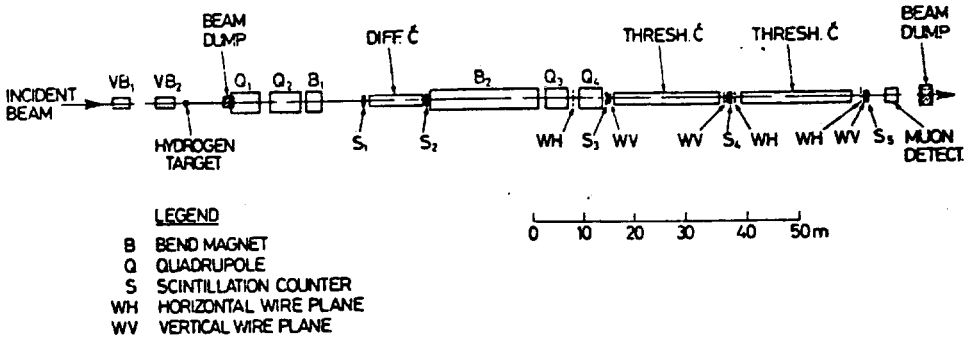

Fig. 10. The focusing spectrometer facility placed in the beam number 6 of the meson area at NAL.

with the previous ISR ones shows the large difference in length of the spectrometers, the difference arising from working in the laboratory system in one case and in the center-of-mass system in the other case.

Figure 11 shows a typical layout of a recoil proton spectrometer used in conjunction with an external proton beam (it will also be used with the internal beam hitting the supersonic gas jet target). Low energy recoil protons are detected through their energy loss and range in solid-state detectors,

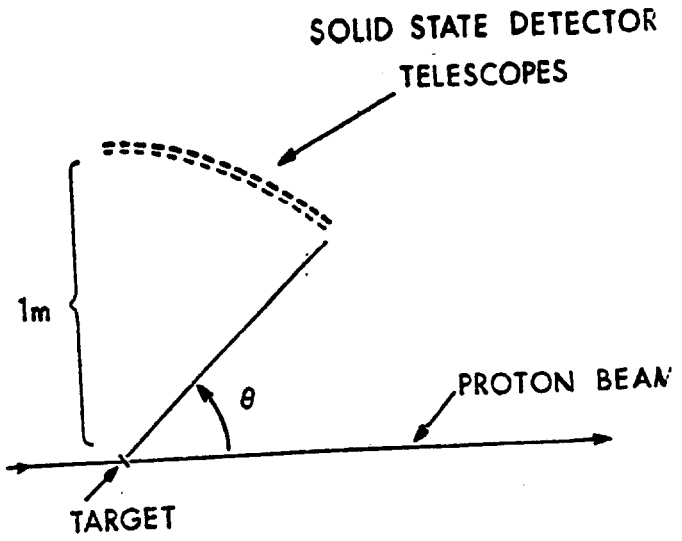

Fig. 11. Proton recoil spectrometer used at NAL with an external proton beam. It will be installed in the internal target area and may be used with the supersonic gas jet target. Recoil protons are analyzed in the first layer of solid state detectors (which measure dE/dx) and then either stop in the second layer (measurement of the total energy), or give a second determination of dE/dx (73C2).

which also measure their angles. The first layer of thin detectors measures dE/dx; in the example of Fig. 11 these detectors are made of 500 μ depleted silicon surface-barrier detectors. The second layer of thick detectors measures either the total kinetic energy for kinetic energies smaller than 30 MeV or again dE/dx for higher energy protons, which do not stop in the detectors. These counters are 500 μ thick lithium drifted silicon detectors.

2.3 Experimental Uncertainties.

It is appropriate to conclude a presentation of technical equipment with a discussion of the precisions of the measurements. The inclusive cross sections for the production of $\pi^{\pm}$, p, n, and γ are typically affected by statistical errors of 1-10% (depending on the transverse momentum); for kaons and antiprotons the statistical errors are typically 4-15%. The uncertainties arising from the corrections (absorption, decay, multiple scattering, etc.) are typically 2-5% (larger for kaons because of their decays). These

uncertainties may be added in quadrature, thus giving errors of 3-10%. A systematic scale error must also be considered; at the ISR it arises mainly from the luminosity determination and may be estimated to be at least ±5%. (One year ago it was 10-15%.) These uncertainties are comparable for experiments with any type of high-energy accelerators.

3. NOTATIONS

In this section we shall recall some kinematical relations. For the simplest inclusive reaction

$$a + b \rightarrow c + X, \tag{4}$$

which is illustrated in Fig. 12, we have to specify the frame of reference, the number and types of variables, and the cross sections. p_a, p_b, and p_c are the

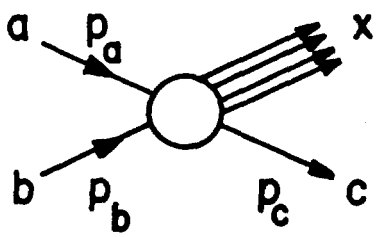

Fig. 12. Illustration of the notation for an inclusive reaction.

four momenta of particles a, b, c, while $\vec{p}_a$, $\vec{p}_b$, and $\vec{p}_c$ are the corresponding three momenta. The metric is chosen such that $p_i^2 = m_i^2$. We shall often refer to particle a as the incident particle, to particle b as the target particle (at rest in the laboratory frame).

3.1 The Lorentz Frames.

Commonly used are the laboratory (lab), antilaboratory (antilab), and center-of-mass (c.m.) frames. Sometimes in works on Regge-Muellerism the rest frame of particle c is also used. Quantities in the lab system will

be denoted with a subscript lab, while c.m. quantities will usually not have any subscripts.

3.2 Independent Variables.

Three independent variables are needed for the kinematical description of reaction (4). We shall often refer to them as energy, transverse, and longitudinal variables. Among the many different choices we shall discuss the following (see Table II).

(i) For the energy variable we shall use either the laboratory momentum of the incoming particle, $p_{a\ lab}$, the total c.m. energy, E_{cm}, or its square

$$s = (p_a + p_b)^2 = E_{cm}^2. \tag{5}$$

(ii) For the transverse variable we shall mostly use the transverse momentum of particle c:

$$p_t = p_{tc} = p\ \sin\theta = p_{c\ lab}\ \sin\theta_{c\ lab} \tag{6}$$

where p and θ are the c.m. momentum and production angle of particle c; $p_{c\ lab}$ and $\theta_{c\ lab}$ are the corresponding quantities in the lab system.

The invariant four-momentum transfer is:

$$t = (p_b - p_c)^2. \tag{7}$$

It may be written as

$$t = -2m_p\ T_{c\ lab} \tag{8}$$

when particles b and c are protons; $T_{c\ lab}$ is the laboratory kinetic energy of particle c.

The longitudinal mass (often improperly called the transverse mass) is

$$m_\ell = m_{\ell c} = E_c^2 - p_{\ell c}^2 = p_t^2 + m_c^2. \tag{9}$$

(iii) For the Longitudinal variable there is an even more ample choice (all quantities refer to particle c, whose subscript will be omitted)

Longitudinal c.m. momentum $$p_\ell = p\cos\theta \tag{10}$$

Feynman x variable $$x = \frac{p_\ell}{p_{\ell\,max}} \xrightarrow{s>>} \frac{2\,p_\ell}{\sqrt{s}} \tag{11}$$

c.m. rapidity variable $$y_c = \frac{1}{2}\,\ell n\,\frac{E + p_\ell}{E - p_\ell} \tag{12}$$

$$\xrightarrow[p_t^2 >> m_c^2]{} - \ell n\,\mathrm{tg}\,\frac{\theta}{2} \tag{13}$$

laboratory rapidity $$y_{lab} = y_{ac} = y_a - y_c \tag{14}$$

y_a is the c.m. rapidity of the incoming particle a. Under a Lorentz transformation along the z axis, taken as the axis of the momentum of particle a in the lab system, the rapidities change by an additive constant [$y' = y - u = y - 1/2\,\ell n\,(1+\beta)/(1-\beta)$]. Thus the relative rapidities, defined in (14), are invariant under this kind of Lorentz transformation.

The range of variability of the x variable is always

$$-1 < x < 1. \tag{15}$$

Thus the x variable is useful for comparing data and different energies. The range of variability for the laboratory rapidity is

$$\ln \frac{m_{\ell c}}{m_a} \lesssim y_{ac} \lesssim \ln \frac{s}{m_b\, m_{\ell c}} \tag{16}$$

and for the c.m. rapidity

$$y_a + \ln \frac{m_{\ell c}}{m_a} \lesssim y_c \lesssim y_b + \ln \frac{m_b}{m_{\ell c}}. \tag{17}$$

Formulae (16) and (17) are valid in the limit of large s values. One sees [from (16)] that the range of rapidities of the observed particle c is of the order of ($\ln$ s), increasing logarithmically with s. Sometimes one introduces the reduced rapidity in order to have a range of variability fixed, independent of energy.

(iv) The missing mass (sometime classified as a longitudinal variable) in reaction (4) is given by:

$$m_X^2 = \left(E_X^2 - \vec{p}_X^{\,2}\right) = (p_a + p_b - p_c)^2 \tag{18}$$

$$= s + m_c^2 - 2m_b\, m_{\ell c} \cosh y_{ca} - 2m_a\, m_{\ell c} \cosh y_{bc}. \tag{19}$$

In the lab system when a, b, c are protons and b is at rest:

$$m_X^2 = m_p^2 + 2\, |\vec{p}_{a_{lab}}|\, |\vec{p}_{c_{lab}}| \cos\theta_{a\,lab}\, T_{c\,lab}\, (E_{a\,lab} + m_p)\ . \tag{20}$$

In the c.m. system when a, b, c are protons:

$$m_X^2 = s + m_p^2 - 2\sqrt{s}\, E_c. \tag{21}$$

(v) For future use we shall recall a few relations among the various variables.

The energy variable s may be expressed in terms of rapidities as follows:

$$s = m_a^2 + m_b^2 + 2m_a m_b \cosh y_{ba} \tag{22}$$

$$\sqrt{s} \xrightarrow[s>>]{} m_b \exp(-y_b) \simeq m_a \exp(y_a). \tag{23}$$

The x variable expressed in terms of rapidities is equal to

$$x_c = \frac{2m_{\ell c}}{\sqrt{s}} \sinh y_c \tag{24}$$

$$\xrightarrow[s>>]{} \frac{m_{\ell c}}{m_a} [1 - \exp(-2\, y_c)] \exp(-y_{ac}) \tag{24a}$$

$$\xrightarrow[s>>]{} \frac{m_{\ell c}}{m_b} [\exp(2\, y_c) - 1] \exp(-y_{cb}). \tag{24b}$$

The relation between missing mass and other variables, when a, b, c are protons, is given by

$$\frac{m_X^2 - m_p^2}{s} = 1 - \frac{2\, E_c}{\sqrt{s}} \xrightarrow[x\simeq 1]{} 1 - X. \tag{25}$$

For $x \simeq 1$ the four-momentum transfer when a, b, c are protons is given by ($T_{c\ lab}$ is small, c is emitted close to 90° in the lab and is not relativistic):

$$t \xrightarrow[x\simeq 1]{} - p_{c\ lab}^2 \simeq - p_t^2. \tag{26}$$

Taking the z axis along the direction of the projectile momentum $\vec{p}_a$, we can write in an arbitrary frame of reference

$$p_a = (m_a \cosh y_a,\ 0,\ 0,\ m_a \sinh y_a) \tag{27}$$

$$p_b = (m_b \cosh y_b,\ 0,\ 0,\ m_b \sinh y_b) \tag{28}$$

$$p_c = (m_{\ell c} \cosh y_c,\ p_c \cos\phi_c,\ p_c \sin\phi_c,\ m_{\ell c} \sinh y_c). \tag{29}$$

We shall mainly use the set of variables (x, p_t) and (y, p_t). The variables x and y may be considered as complementary in the sense that each one is better suited for exploring a different range in the phase space of the inclusive reactions considered.

Table II. Frames of Reference and Set of Variables Often Used for the Analysis of Inclusive Reactions.

Frames	Set of Variables
Target or Lab Frame (rest frame of particle c)	$p_{a\,lab}$, $\theta_{c\,lab}$, $p_{c\,lab}$
	$p_{a\,lab}$, p_t, $y_{c\,lab}$
Projectile or Antilab Frame (rest frame of particle a)	symmetric of lab frame
c.m. Frame	E_{cm}, θ_c, p_c
	s, p_t, p_c
	s, p_t, x
	s, p_t, y
	s, t, M^2
Rest frame of particle c	

3.3 Cross Sections.

The differential one particle inclusive cross section is given by:

$$\frac{d\sigma}{dp} = \frac{1}{\gamma(s)} \sum_k k \int \delta^4 (p_a + p_b - \sum_{i=1}^{n} p_i) \frac{|M_k|^2}{k!} \prod_{i=2}^{n} (dp_i) = \sum_k k\, \sigma_k . \quad (30)$$

(30) gives the inclusive cross section as the sum over each exclusive cross section σ_k where particle c is produced k times. M_k is the relevant matrix element (including 2π factors); k! is the permutation factor which gives the right counting of the final states; $\gamma(s)$ is the incident flux

$$\gamma(s) = \left[\left(s-m_a^2-m_b^2\right)^2 - 4m_a^2 m_b^2\right]^{1/2} \xrightarrow[s>>]{} s \qquad (31)$$

dp_i denotes the invariant phase space element

$$dp_i = \delta\left(p_i^2 - m^2\right)d^4p_i = \frac{d^3p_i}{2E_i}. \qquad (32)$$

The inclusive cross section will be usually presented in the invariant form:

$$f = E\frac{d^3\sigma}{d^3\vec{p}} = \frac{E}{p^2}\frac{d^2\sigma}{d\Omega dp} = \frac{E}{\pi}\frac{d^2\sigma}{dp_\ell dp_t^2} = \frac{1}{\pi}\frac{d^2\sigma}{dy\,dp_t^2} = \frac{s}{\pi}\frac{d^2\sigma}{dt\,dM^2} = \frac{2E}{\pi\sqrt{s}}\frac{d^2\sigma}{dx dp_t^2}. \qquad (33)$$

3.4 Scaling and Limiting Fragmentation.

The statement of Feynman scaling is written in the c.m. frame

$$f(s,\ p_t,\ x) \xrightarrow[s\to\infty]{} f(p_t,\ x) \qquad (34)$$

with $f(p_t,\ x=o)$ finite. Thus in the asymptotic limit for large s the inclusive distribution depends on p_t and on the scaling variable x. Eq. (34) should be valid for the whole domain of x, that is $-1 < x < 1$.

The limiting fragmentation hypothesis of Benecke et al. is written in the lab system as:

$$f(s,\ p_t,\ p_{\ell c\ lab}) \xrightarrow[s\to\infty]{} f(p_t,\ p_{\ell c\ lab}) \qquad (35)$$

where $p_{\ell c\ lab}$ is the longitudinal laboratory momentum of particle c. Particle c is considered a fragment of the target b. A similar statement holds in the rest frame of the projectile; then c is considered a fragment of the projectile a. The limiting fragmentation hypothesis of Benecke et al. is stated for x close to ± 1;

no statement is made for $x \simeq o$. We shall in general ignore these detailed considerations and shall refer to scaling or to limiting distributions when the cross sections have become energy independent.

3.5 Factorization.

Many theoretical models assume or obtain the factorization property in either (p_t, x) or (p_t, y_{lab}). Factorization in (p_t, y_{lab}) means that the invariant cross section may be written as product of two independent functions of p_t and y_{lab}:

$$f(s, p_t, y_{lab}) \simeq F(p_t)\, G(y_{lab}). \tag{36}$$

3.6 Simple Pictures of Multiparticle Production.

Before discussing the experimental data it may be worthwhile to sketch a few simple-minded graphs in order to give an intuitive idea of what is happening.

Because at all energies the cross section is confined to small values of the transverse momentum, the distribution of secondaries must become more and more elongated in the longitudinal momentum as the energy increases. In a (p_t, p_ℓ) plot (Peyrou-plot), the contours of constant cross sections should therefore behave as follows

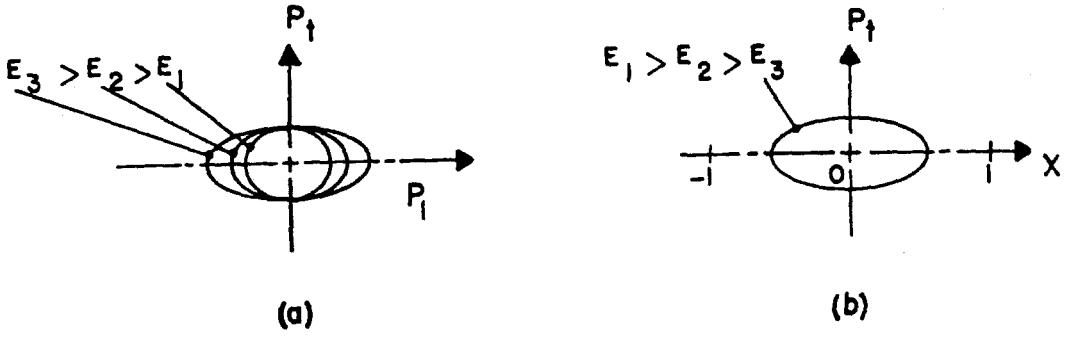

Fig. 13. Contours of constant cross sections in a (p_ℓ, p_t) plot.

The scaling hypothesis states that at high energy the contours of constant invariant cross sections do not depend on the energy, but are functions of p_t and x only (Fig. 13b).

In a (p_t, y) plot there is a situation similar to that in the (p_t, p_ℓ) plot; the range where the invariant cross section is different from zero is essentially a rectangle, whose base length is kinematically limited as given by Eq. (17), while its height is limited by the experimental cutoff in p_t to values of ~500 MeV/c. One can separate the single particle spectra in the rapidity plot in different regions, making the hypothesis of the existence of a certain correlation length L (hypothesis of short-range order). One assumes that two particles produced in a high-energy interaction are uncorrelated if their relative rapidity is larger than L. One can then define the following three regions (see Fig. 14a)

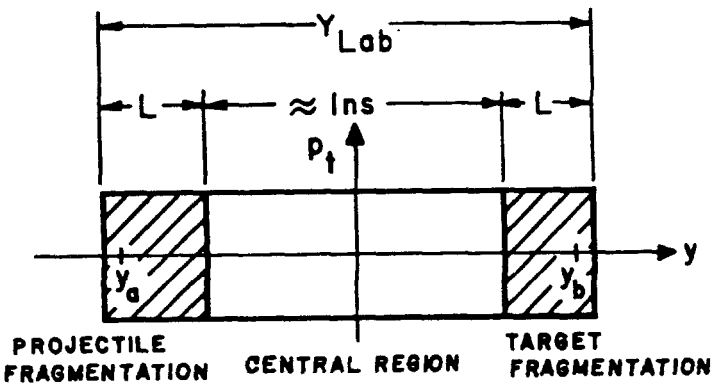

Fig. 14(a). Illustration of the central and fragmentation regions i plane.

Target fragmentation of fixed length L about y_b;

Projectile fragmentation of fixed length L about y_a;

Central region of length ≈ ln s.

A simple picture of the above definitions may be obtained thinking in terms of central and peripheral collisions, as shown in Fig. 14b. The central

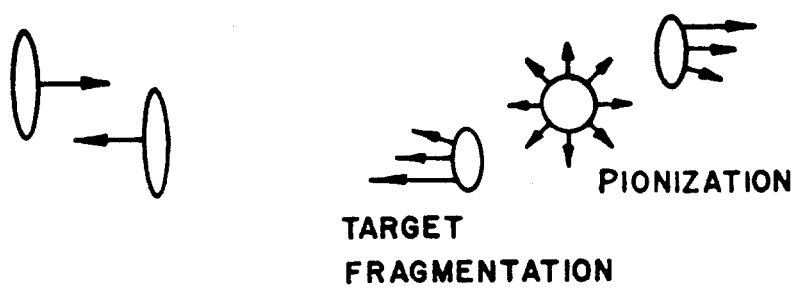

Fig. 14(b). A naive picture of the collision where the incoming particles are represented as contracted spheres and the outgoing particles originate from the different spatial regions.

region arises from the central part of the collision, while the two fragmentation regions arise from the peripheral parts of the collisions.

The experiments on particle correlation indicate that the correlation length is about $L \simeq 2$. This means that the central region starts to develop only for laboratory momenta larger than 100 GeV/c. At lower energies one has only fragmentation of the in-going particles.

4. ANALYSIS OF THE EXPERIMENTAL DATA IN INCLUSIVE pp COLLISIONS

We shall discuss the experimental data on pp collisions measured at the CERN-ISR and at NAL, analyzing first the invariant cross sections as function of one variable, keeping the others constant.

4.1 $f = f(p_t)$.

4.1.1 Shape of the p_t-Distributions.

Phenomenologically the p_t-distribution may be subdivided into three regions (see Fig. 15):

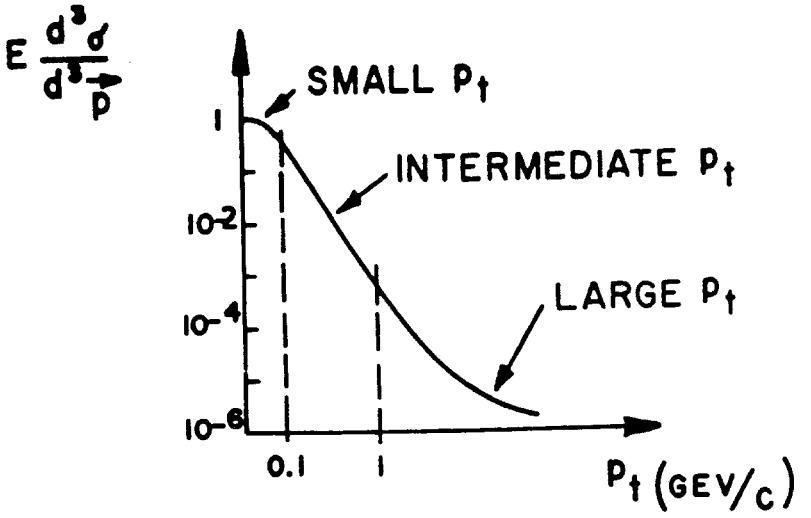

Fig. 15. Illustration of the shape of the p_t distribution.

(i) Small p_t region, for $p_t < 0.1$ GeV/c. Very little is known about this region. Lower energy data and general analytic considerations suggest that the invariant cross section has a weak p_t dependence for very small values of p_t.

(ii) Intermediate p_t region, for $0.1 < p_t < 1$ GeV/c. The bulk of the experimental data refers to this region. It is from these data that one can establish the approximate exponential dependence on p_t, that the average transverse momentum is about 350 MeV/c for pions, ~450 MeV/c for kaons and 500 MeV/c for nucleons.

(iii) Large p_t region, for $p_t > 1$ GeV/c. The cross sections become very small in this region. The experimental data suggest that $f(p_t)$ decreases slower than an exponential. It is hoped that data on this region will yield some information on the inner structure of the elementary particles.

The p_t distribution may be studied globally, that is for all events, or differentially by keeping constant the x or the y_{lab} variables. For each of

these choices one tries to see if the p_t dependence is simple in p_t, p_t^2, m_l, or m_l^2. For this purpose the data in the intermediate p_t region are fitted to functions of the type:

$$f = E \frac{d^3\sigma}{d^3\vec{p}} = A \exp(-B\, p_t) \tag{37}$$

$$f = C \exp\left(D\, p_t^2\right) \tag{38}$$

$$f = E \exp\left[F\left(m^2 + p_t^2\right)\right] . \tag{39}$$

The results of some of the fits are given in Table III.

Figures 16-21 show experimental data obtained at the CERN-ISR on transverse momentum distributions in the intermediate p_t region (73C4). Inspection of the figures and of Table III indicates the following:

(i) The p_t distributions obtained at fixed x or y_{lab} are exponential in p_t for all particles with the exception of the protons, whose distributions are exponential for small values of x and gradually become exponential in p_t^2 as x becomes large.

(ii) All curves are better represented by exponentials when the data refer to y_{lab} = constant than x = constant.

(iii) The slopes are larger for pions (slope B = 6 $(GeV/c)^{-1}$); smaller for kaons (B = 5.5) and still smaller for proton and antiprotons (B = 4). The π^+ slopes are just a bit smaller than the ones for π^-.

(iv) The slopes F of Eq. (39) for pions and kaons are equal (see Fig. 20).

(v) The p_t dependence for the data taken at a constant c.m. angle does not have a simple form (see Fig. 21). In fact, it is an exponential for pions, while

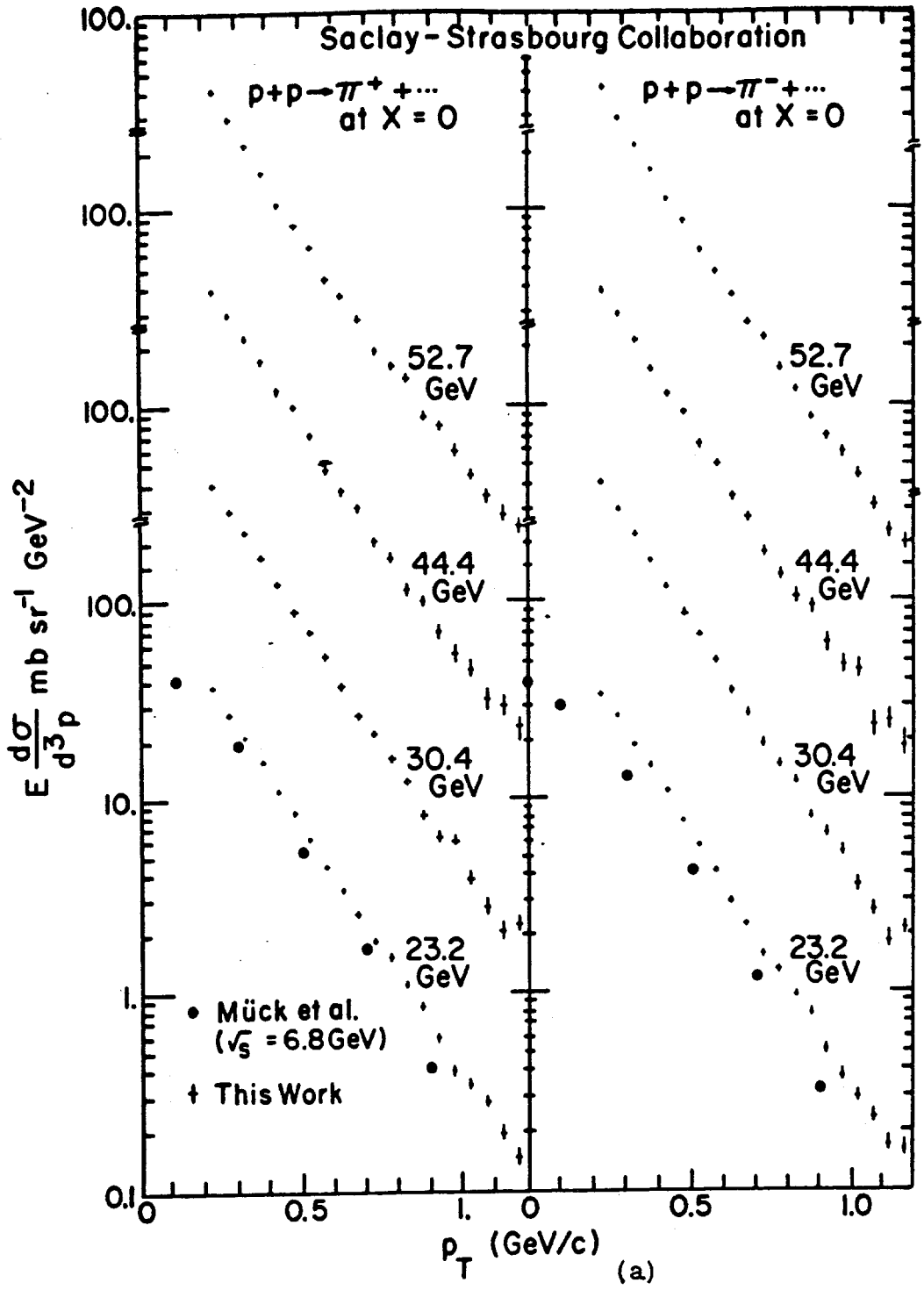

Fig. 16. The invariant cross section for the production of π^- and π^+ in proton-proton collisions at fixed values of (a) x=0 (73B2) and (b) x=0.08, 0.16, 0.32, and 0.48 (73C4) plotted versus the transverse momentum for several ISR energies.

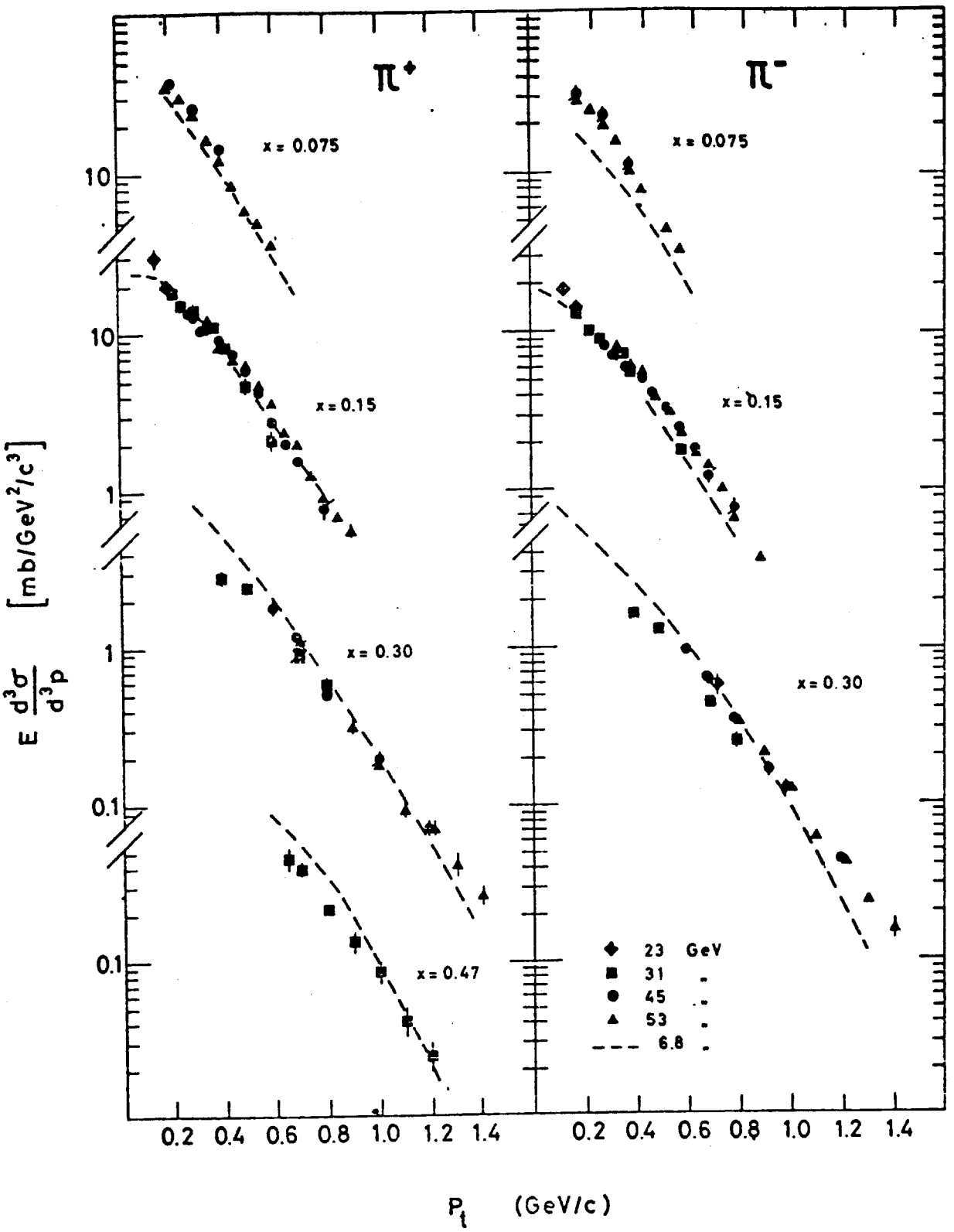
π+
π−
x = 0.075
x = 0.15
x = 0.30
x = 0.47
23 GeV
31 "
45 "
53 "
6.8 "
E d³σ/d³p [mb/GeV²/c³]
P_t (GeV/c)
10
1
0.1
0.2 0.4 0.6 0.8 1.0 1.2 1.4

Fig. 16(b)

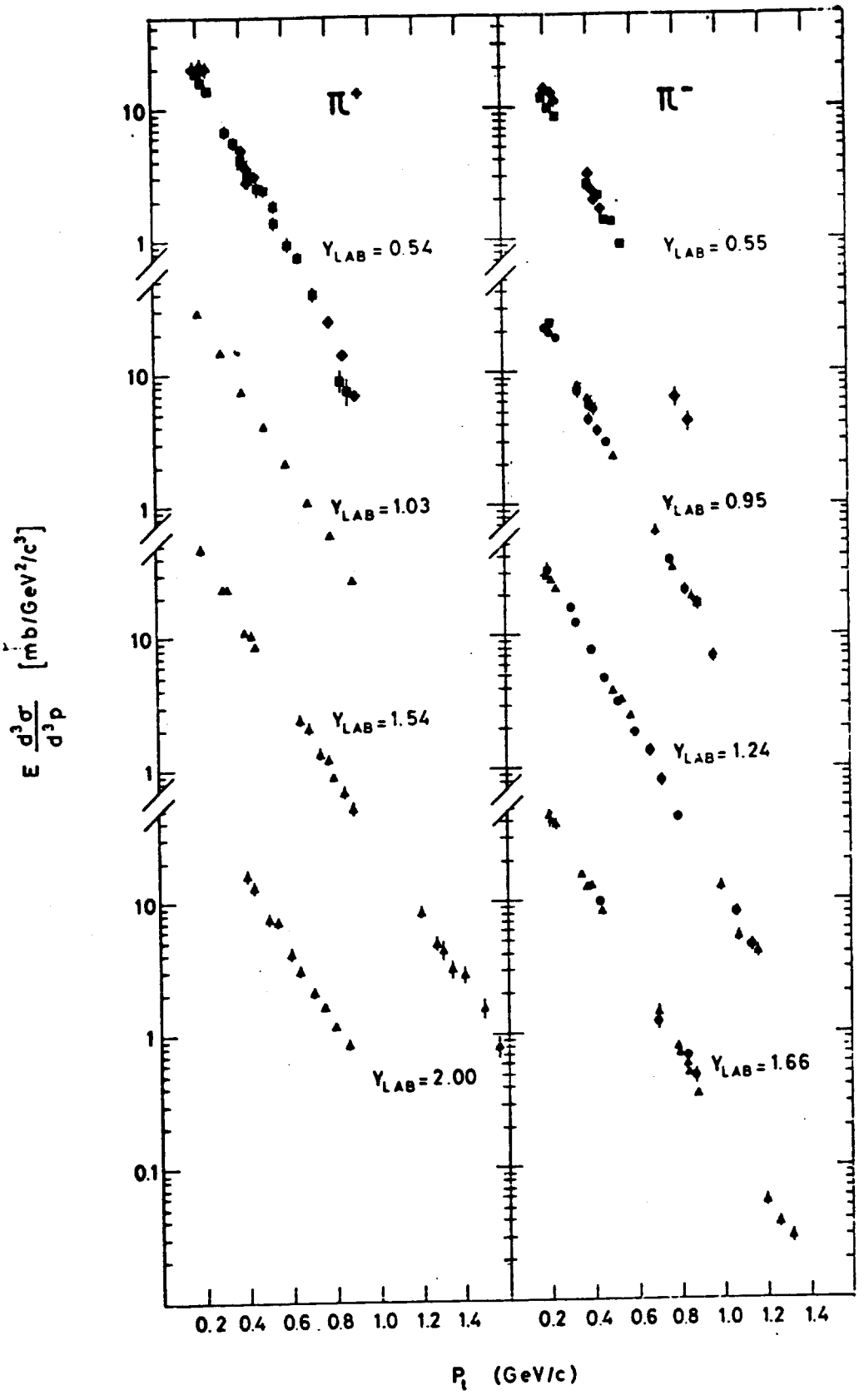

Fig. 17. The invariant cross sections for π^- and π^+ production at the values y_{lab}=0.5, 1, 1.5, and 2 plotted versus p_t (73C4).

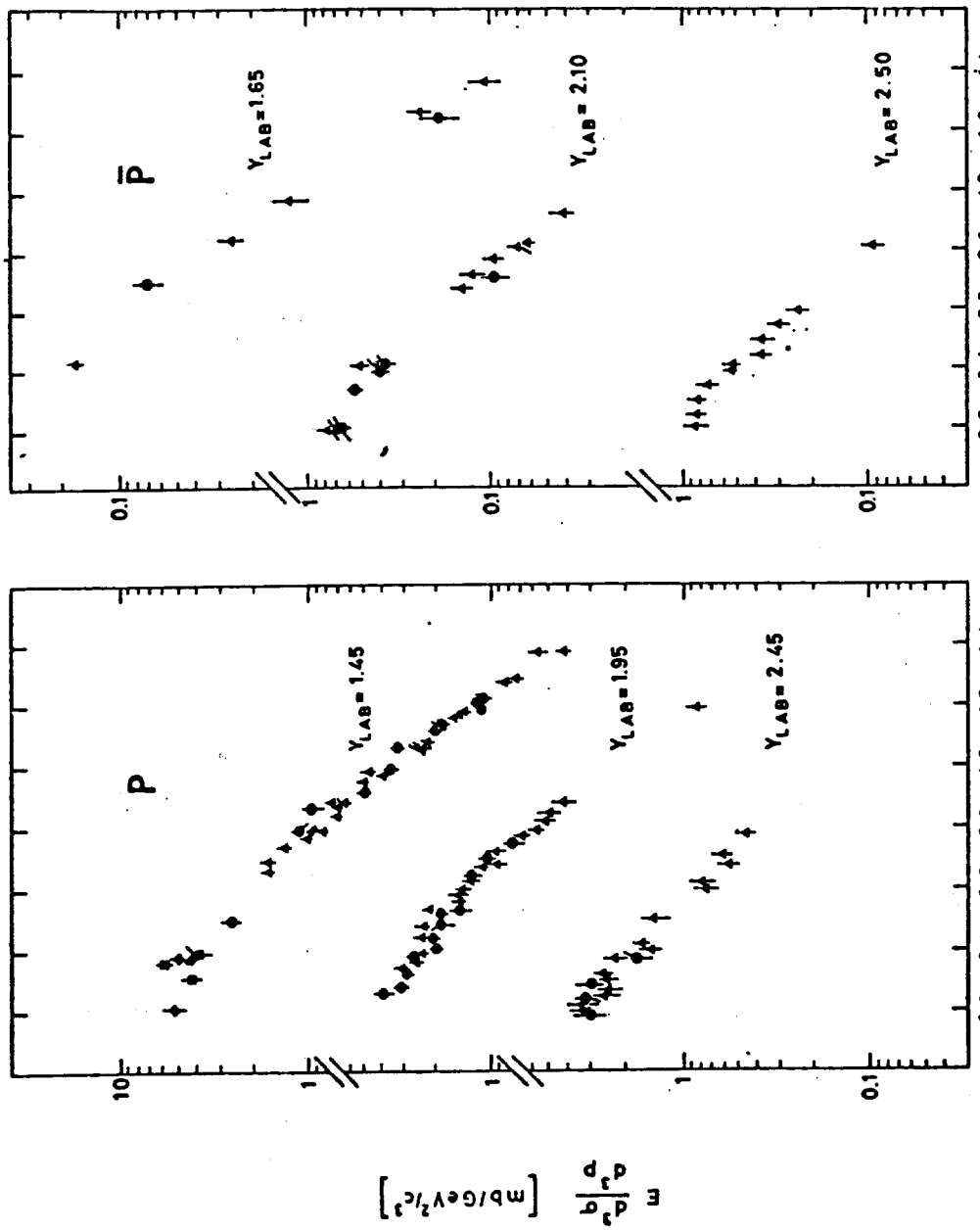

Fig. 18. The invariant cross section for proton and $\bar{p}$ production at the values y_{lab}=1.5, 2, and 2.5 plotted versus p_t (73C4).

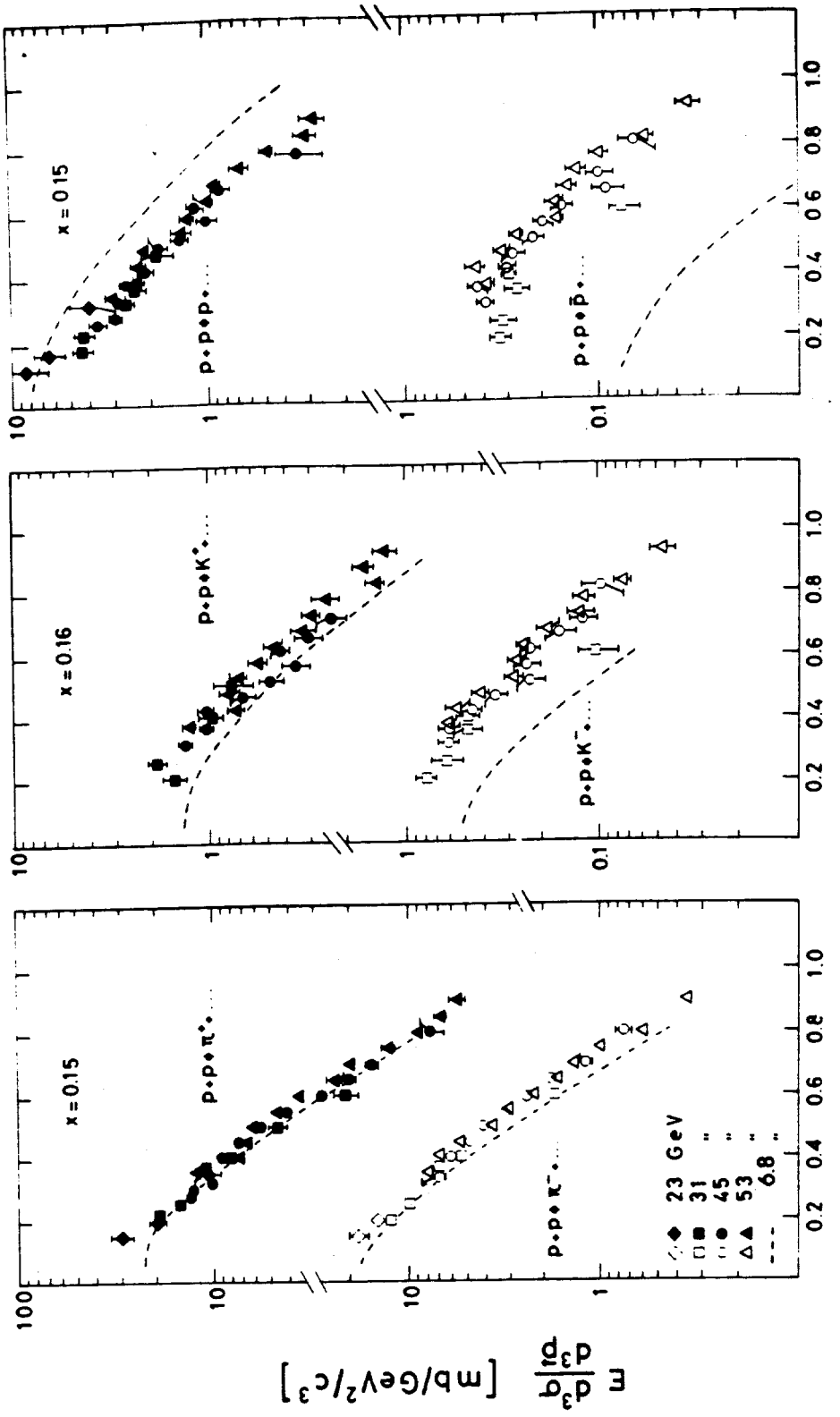

Fig. 19. The invariant cross sections for π^-, π^+, K^-, K^+, $\bar{p}$, and p production at x=0.15 plotted versus p_t (73C4). The dashed lines represent interpolations through data taken at E_{cm}=6.8 GeV (72A1).

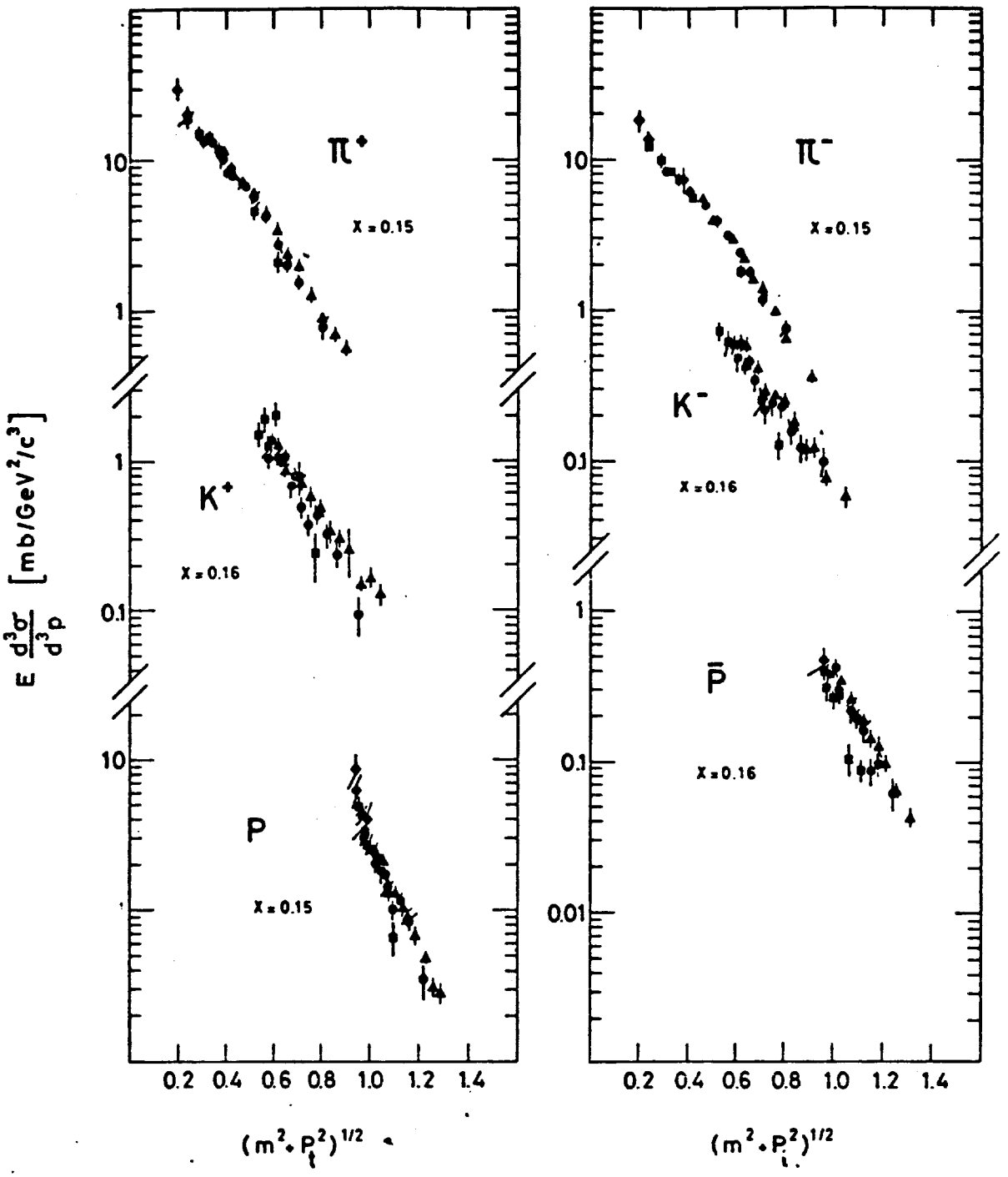

Fig. 20. The invariant cross sections for π^-, π^+, K^-, K^+, $\bar{p}$, and p production at x=0.15 plotted versus the longitudinal mass (73C4).

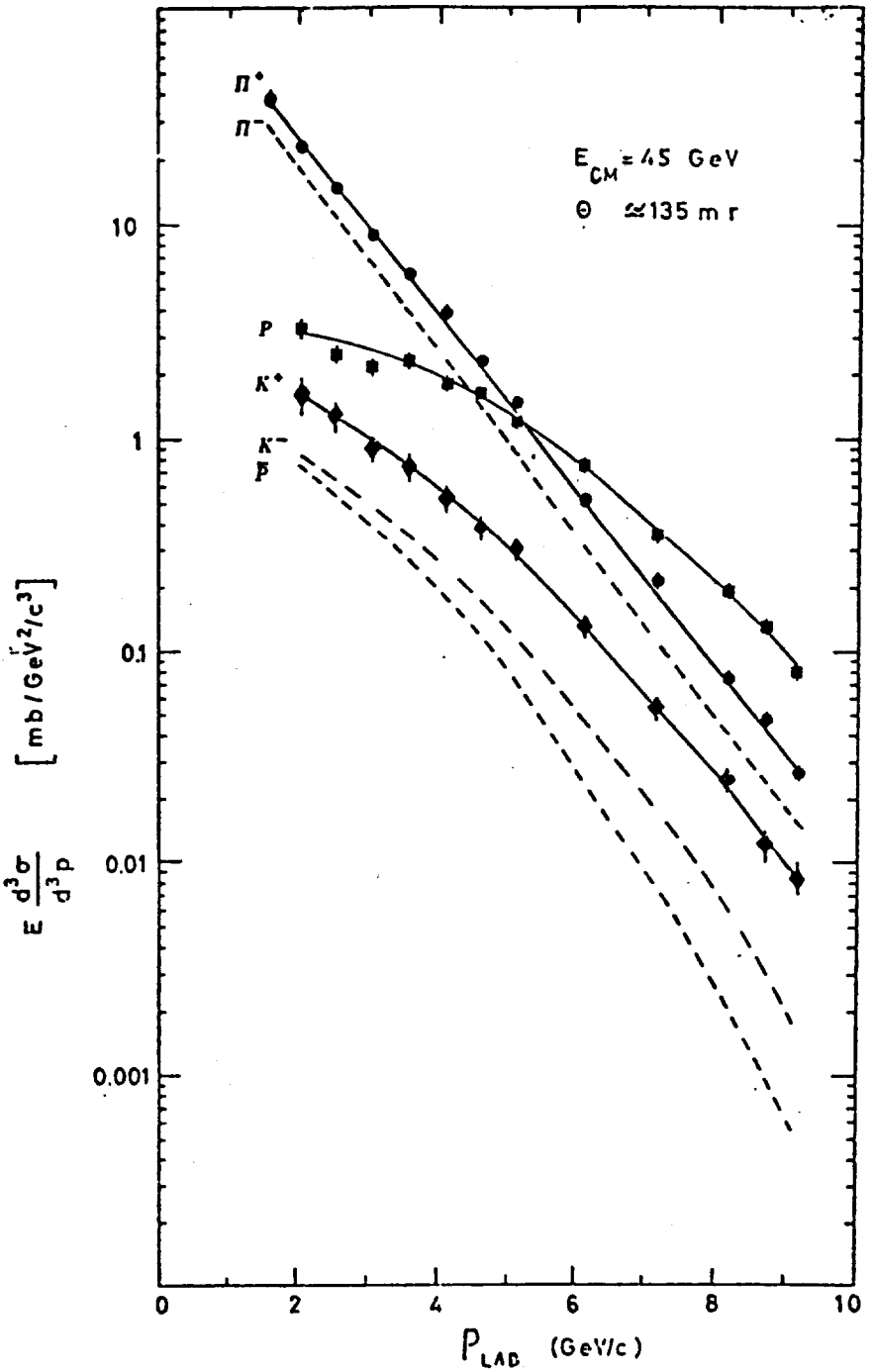

Fig. 21. The invariant cross sections at the fixed angle of 135 mrad in the ISR frame of reference (73C4).

it is more complex for kaons and nucleons. This fact is easily explained: for pions, a fixed angle means a fixed rapidity according to Eq. (13), while this is not so for the other particles, at least at low p_t. Thus if the dependence on p_t is simple when the data are taken at fixed y_{lab}, this is not anymore so for data at a fixed angle.

Table III. Results of Fitting the Invariant Cross Sections at Fixed y_{lab} to the Expressions (37), (38), and (39) (73C4).

				$A\,e^{-Bp_t}$		$C\,e^{-Dp_t^2}$		$E\,e^{-F\left(m^2+p_t^2\right)^{1/2}}$	
Particle	$\sqrt{s}$ (GeV)	y_{lab}	p_t-Range (GeV/c)	B $(GeV/c)^{-1}$	χ^2/DF	D $(GeV/c)^{-2}$	χ^2/DF	F $(GeV/c)^{-1}$	χ^2/DF
π^+	23-31	0.54	.20- .97	7.80±.09	2.08			8.10±.10	1.49
	53	1.03	.20- .90	6.57±.12	.26			6.86±.13	.41
	53	1.54	.20-1.56	6.34±.07	.77			6.49±.07	1.13
	53	2.00	.40- .83	6.31±.30	.23			6.47±.23	.70
π^-	23-31	0.55	.20- .86	8.53±.11	2.71			8.87±.14	1.42
	31-53	0.95	.20- .97	7.31±.08	1.14			7.62±.08	1.30
	45-53	1.24	.20-1.17	6.94±.06	1.26			7.19±.06	1.19
	45-53	1.66	.20-1.32	6.79±.07	1.47			7.02±.08	1.97
K^+	31-53	1.44	.21-1.27	4.79±.10	1.20	3.19±.10	2.83	5.93±.13	.86
	45-53	1.64	.21-1.46	4.91±.17	1.00	2.86±.20	4.60	5.84±.24	1.16
	53	1.95	.21- .93	4.53±.19	.80	3.89±.19	2.09	6.22±.28	1.13
K^-	45-53	1.45	.37-1.27	5.59±.12	.78	3.47±.12	5.07	6.73±.16	1.47
	45-53	1.64	.21-1.25	5.49±.15	1.82	3.48±.18	3.11	6.79±.22	1.19
	53	2.00	.21- .93	4.94±.20	.97	4.26±.22	1.11	6.81±.30	.55
p	23-53	1.45	.21-1.38			2.60±.03	1.61	6.97±.07	.97
	45-53	1.95	.26-1.19			2.88±.09	.74	6.73±.17	.67
	45-53	2.45	.19- .78	3.38±.18	.61	3.53±.23	1.04	7.63±.28	.87
$\bar{p}$	45-53	1.65	.43-1.36			3.14±.12	1.26	8.29±.26	.71
	45-53	2.10	.20- .92			3.73±.15	.70	8.36±.32	.47
	53	2.50	.20- .81	3.79±.23	.80	3.84±.31	.78	8.39±.25	.58

4.1.2 Average Transverse Momentum.

The average transverse momentum for the production of particle c may be defined as

$$\langle p_t \rangle_x = \int p_t f \, dp_t^2 / \int f \, dp_t^2 \qquad (40)$$

where the subscript x means that the computation was performed using invariant cross sections at fixed x values. Thus $\langle p_t \rangle_{y_{lab}}$ means that the computation is performed for a fixed laboratory rapidity.

The practical computation of the average transverse momentum may be performed using directly the definition (40). If the cross section is exponential in p_t one has simply

$$\langle p_t \rangle_y = \int p_t e^{-Bp_t} \, dp_t^2 / \int e^{-Bp_t} \, dp_t^2 = \frac{2}{B}. \qquad (41)$$

Since there are few data for $p_t < 0.1$ GeV/c and $p_t > 1.5$ GeV/c, one needs extrapolations of the cross sections in order to compute the average values of the transverse momentum for different particles. The procedure may yield an error of a systematic nature which may be estimated to be between 5 and 10% of $\langle p_t \rangle$.

Figures 22 and 23 show the average values of the transverse momentum for $\pi^{\pm}$, $K^{\pm}$, p, and $\bar{p}$ computed for fixed values of x and y_{lab} and plotted versus the two variables (73C4).

With the exception of protons, $\langle p_t \rangle_x$ is smallest at x = 0, then increases with x and reaches an approximately constant value for $x > 0.2$. This is sometimes referred to as "seagull effect".

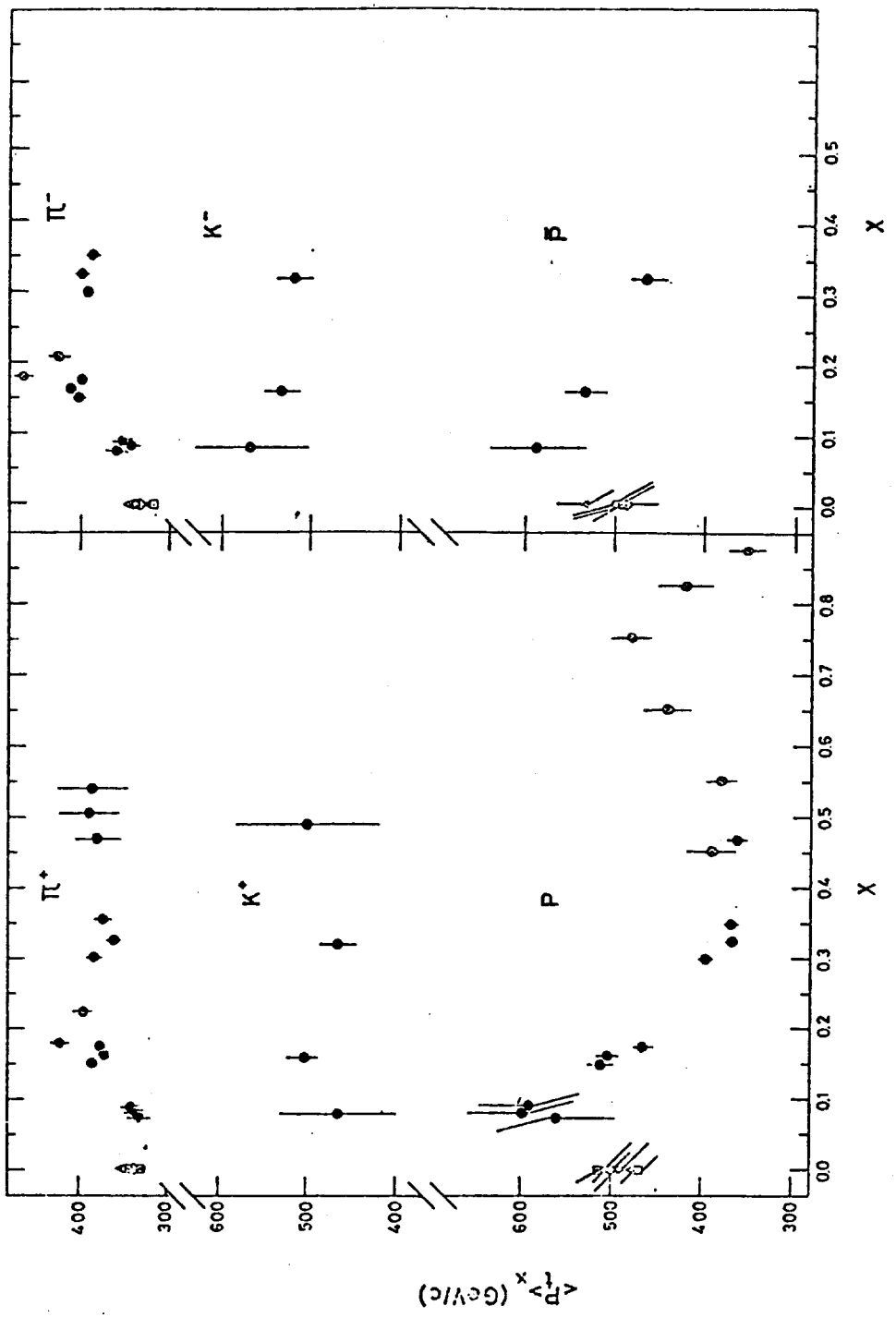

Fig. 22. Average values of the transverse momentum of $\pi^{\pm}$, $K^{\pm}$, and $p^{\pm}$ computed for fixed values of the x variable ($<p_t>_x$) plotted versus x (73C4).

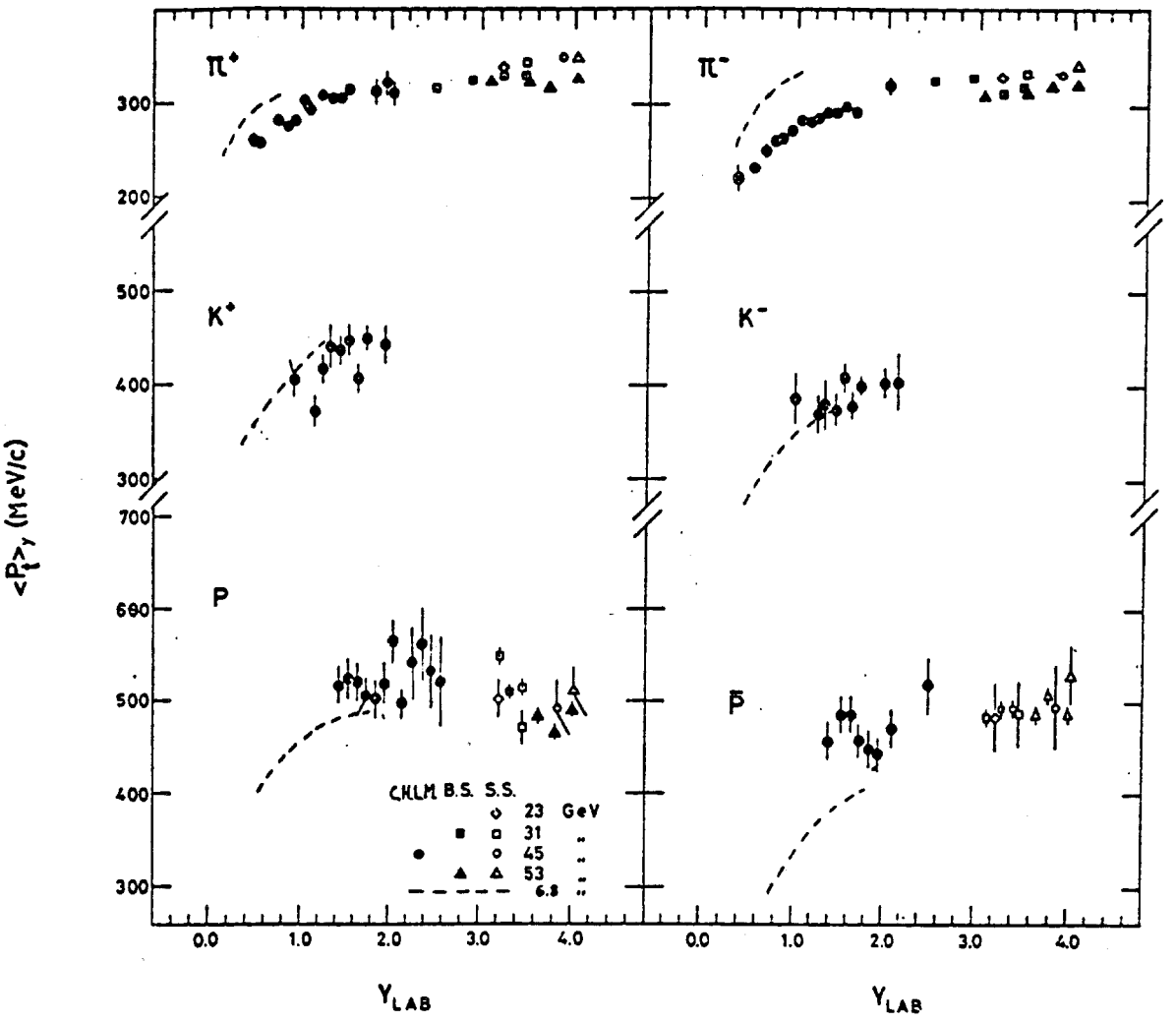

Fig. 23. Average values of the transverse momentum of $\pi^{\pm}$, $K^{\pm}$, and $p^{\pm}$ computed for fixed values of the y_{lab} variable $\left(\langle p_t \rangle_{y_{lab}}\right)$ plotted versus y_{lab} (73C4).

The precision of kaon and antiproton data is not really adequate to establish the seagull effect, though the data are consistent with it. For protons the situation is more complex: at small values of x, $\langle p_t \rangle_x$ increases with x, reaches a maximum, then decreases and has a broad maximum.

The results of Figs. 23 and 24 on $\langle p_t \rangle_{y_{lab}}$ plotted versus y_{lab} lead to the following picture for pions:

(i) For small y_{lab}, $\langle p_t \rangle_{y_{lab}}$ is very small and increases quickly. This rapid change for $y_{lab} < 1$ is a kinematical effect, since in this region one simply cannot produce large transverse momenta. For $y_{lab} > 2$, $\langle p_t \rangle_{y_{lab}}$ increases slowly with y_{lab}. This means that there is no factorization of the invariant cross section as function p_t and y_{lab}, and thus that Eq. (37) is only a first-order approximation even for large y_{lab}.

(ii) The shapes of the $\langle p_t \rangle_{\pi^+, y_{lab}}$ and $\langle p_t \rangle_{\pi^-, y_{lab}}$ are quite similar, the π^+'s having a slightly larger value of the average transverse momentum.

(iii) The results from different energies superimpose one on the other on a kind of "universal curve", which may be explored completely only at the highest energies. If this is correct, it is clear that the integration of $\langle p_t \rangle_{y_{lab}}$ over y_{lab} will yield average values which increase slowly with energy.

Within their larger errors, the average transverse momentum of kaons behaves as for pions, but the "plateau" is at about 450 and 400 MeV/c for K^+ and K^- respectively.

For protons and antiprotons the average transverse momentum is about 500 MeV/c, the antiproton one being somewhat smaller.

4.1.3 The Production of Large Transverse Momentum Particles.

At large transverse momenta, the cross section for pion production decreases more slowly than an exponential, leading to values about 100 times

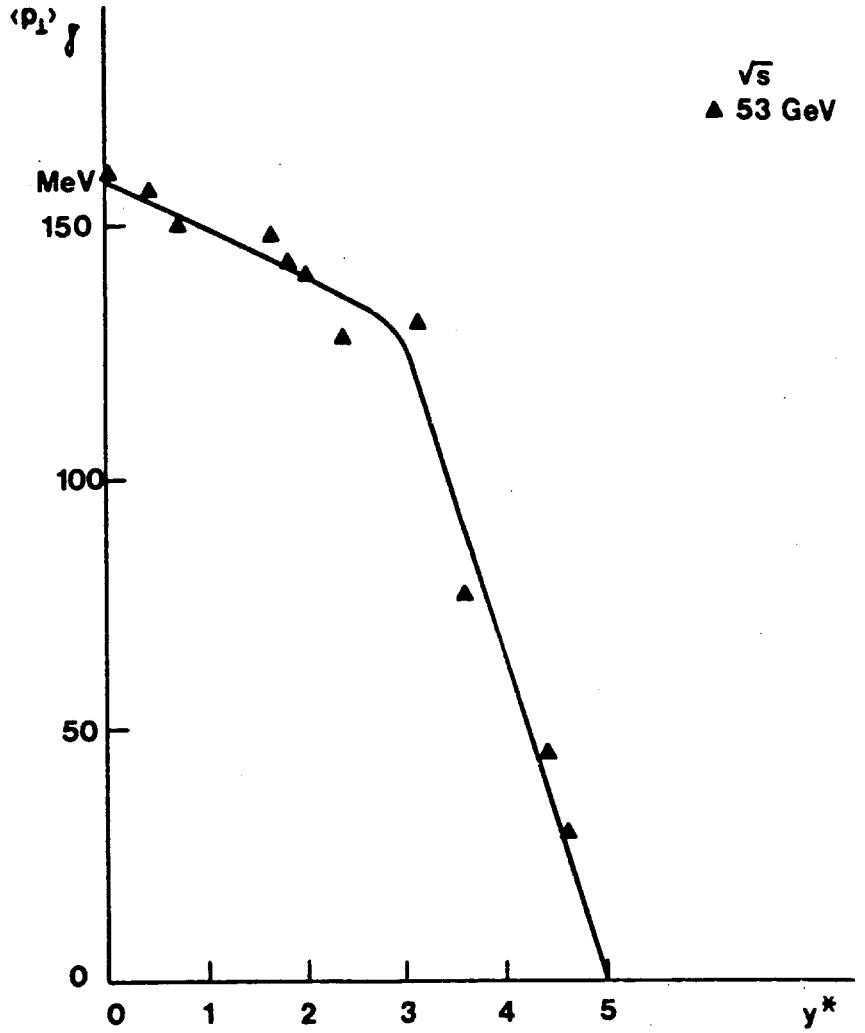

Fig. 24. Average values of the transverse momentum of γ-rays at fixed y_{lab} values (72N1). The line represents the prediction of the thermodynamical model.

larger than from an exponential fall off at $p_t \simeq 4$ GeV/c (see Fig. 25). Some of the data shown in Fig. 5 are not yet final. The cross sections to be measured are very small, thus many precautions have to be taken. For instance some of the data of Fig. 25 were taken with an "almost inclusive" trigger in order to reduce the background. This could lead to some biases at large p_t. The experiments agree on the shapes of the distributions, but there is some disagreement on the energy dependence, some claiming there is none (73A6),

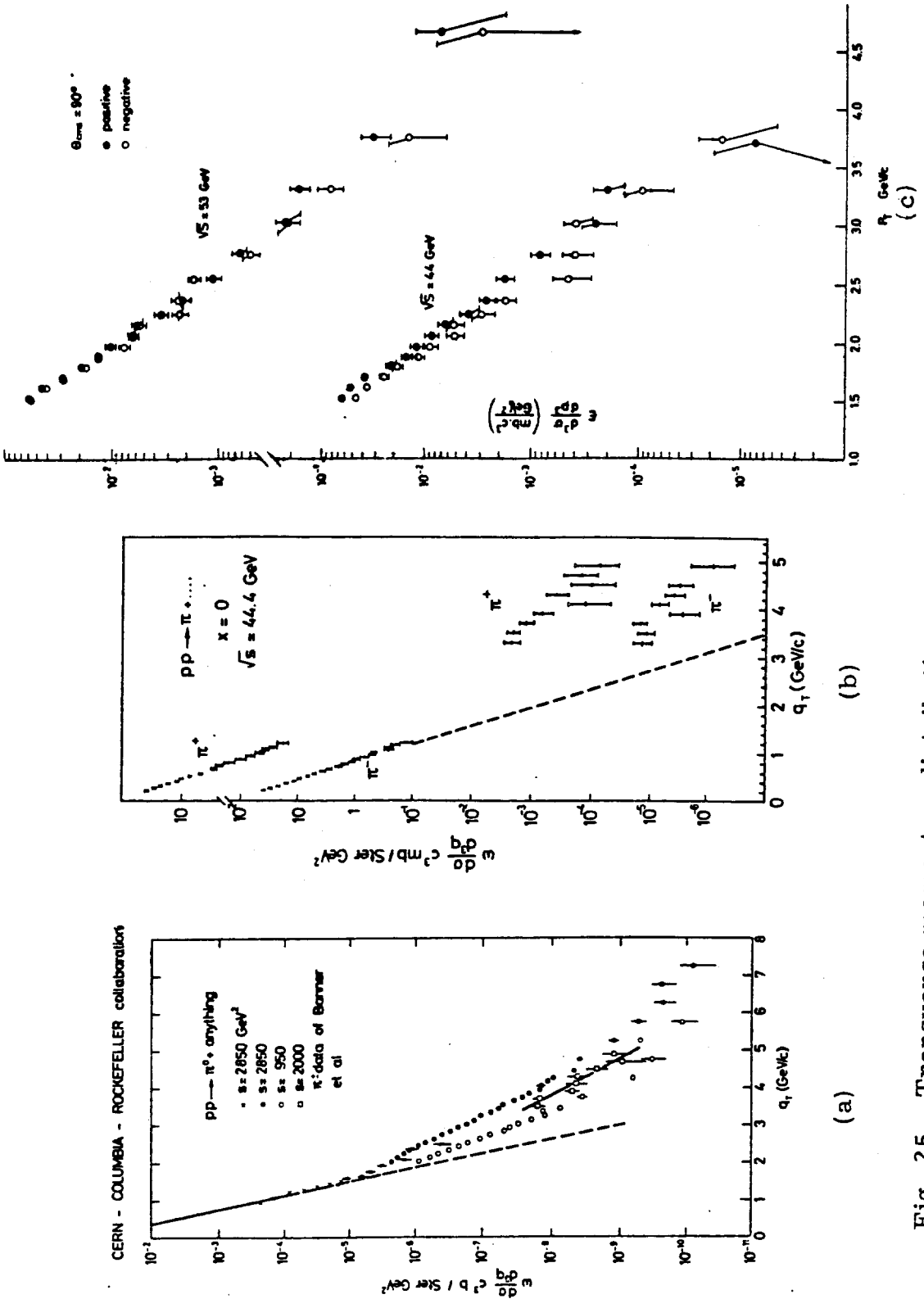

Fig. 25. Transverse momentum distributions at x≈0 and for large p_t for (a) π^0 (73C5), (b) π^+, π^- (73B2), (c) charged particles (73A6), (d) γ-rays (73C1), and (e) charged positive particles (73C8).

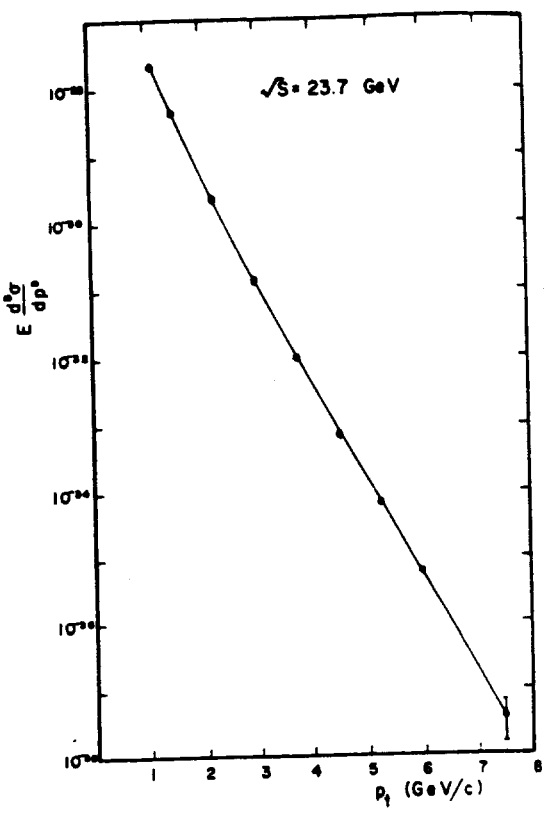

(d)

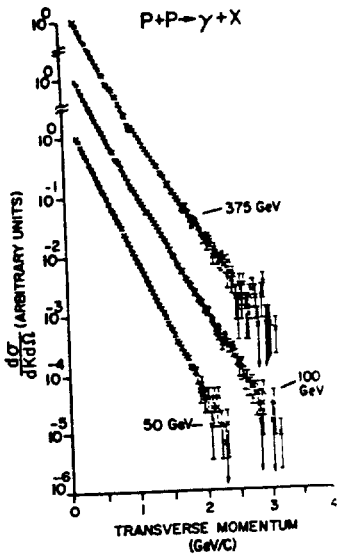

(e)

Fig. 25

while most of the others claim a large s dependence. It would be somewhat surprising if there is no energy dependence at such large values of p_t, in view of the high thresholds for such processes. The photon production experiment of NAL (73C1) observe that their distributions start deviating from exponentials at an energy around 100 GeV.

At large p_t, the number of π^+'s is considerably larger than the number of π^-'s.

The events at large-momentum transfer could arise from a number of mechanisms. One mechanism could be the point-like interaction expected if the proton interaction is in reality due to a parton-parton (or quark-quark) interaction. Another mechanism could arise from the decay of some unstable

massive particles. A third mechanism would be a sort of multiple scattering inside the nucleons. The experimental information is not yet adequate to establish which is the mechanism. In order to gain more insight, one probably has to study the secondaries emitted in the collisions which give rise to the particle with large p_t.

4.2 Dependence on the Longitudinal Variables.

We shall discuss the dependence of the invariant cross section on the variables y_{lab} and x for data taken at fixed p_t values.

4.2.1 $f = f(y_{lab})$.

It may be worthwhile to recall briefly what we may expect for the behavior of the invariant cross section as function of y and of y_{lab}. Figure 26

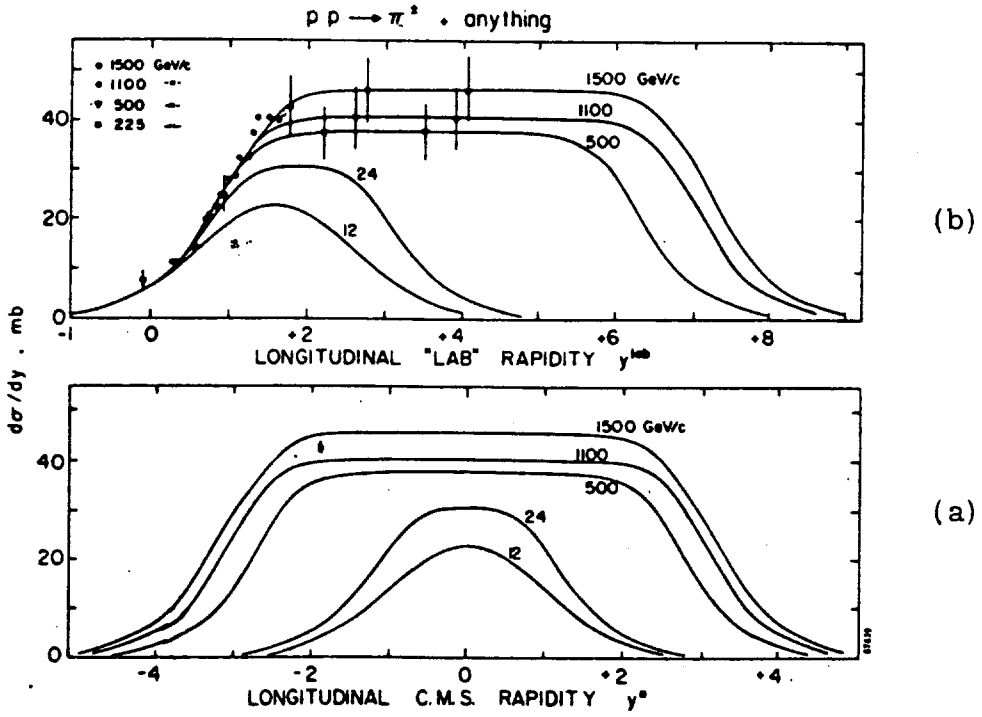

Fig. 26. Illustration of the behavior of the invariant cross section plotted versus y and y_{lab}.

illustrates these dependences for the production of pions at five values of the incident lab momentum. In the case of pp collisions, the inclusive particle production cross section f is symmetric around y = 0 [see Fig. 26(a)]. At ISR energies the cross section has a plateau at small y (central region) and falls off to zero at large y values (fragmentation regions). In Fig. 26(b) the same behavior is observed, but the horizontal scale is shifted (remember that $y_{lab} = y_{max} - y$). Let us consider only the first half of each curve. Figure 26(b) illustrates that the invariant cross sections tend to superimpose one on the other for small values of y_{lab}. If this illustration represents the truth, then it is clear that a representation in terms of y_{lab} may be simpler and of a deeper physical content. It would in fact say that the limiting distributions are necessarily reached at relatively low energies in the fragmentation region and later in the central region. If a kind of "universal curve" exists, data at different energies explore different parts of this curve. One must be cautioned against these simple-minded explanations since many times physicists have dreamed of universal curves, only to find out that they are first approximations of a more complex picture.

Figure 27 shows a compilation of data at different ISR energies for the production of $\pi^{\pm}$, $K^{\pm}$, p, and $\bar{p}$ versus the laboratory rapidity. Because of the symmetry existing in pp collisions, we only show one half of the curve. All the data were taken at a transverse momentum of 0.4 GeV/c (73A8). The dotted lines represent interpolations through the data at a laboratory momentum of 24 GeV/c. For pions the picture seems to be the one discussed at the beginning of this section: all the data taken at different energies superimpose

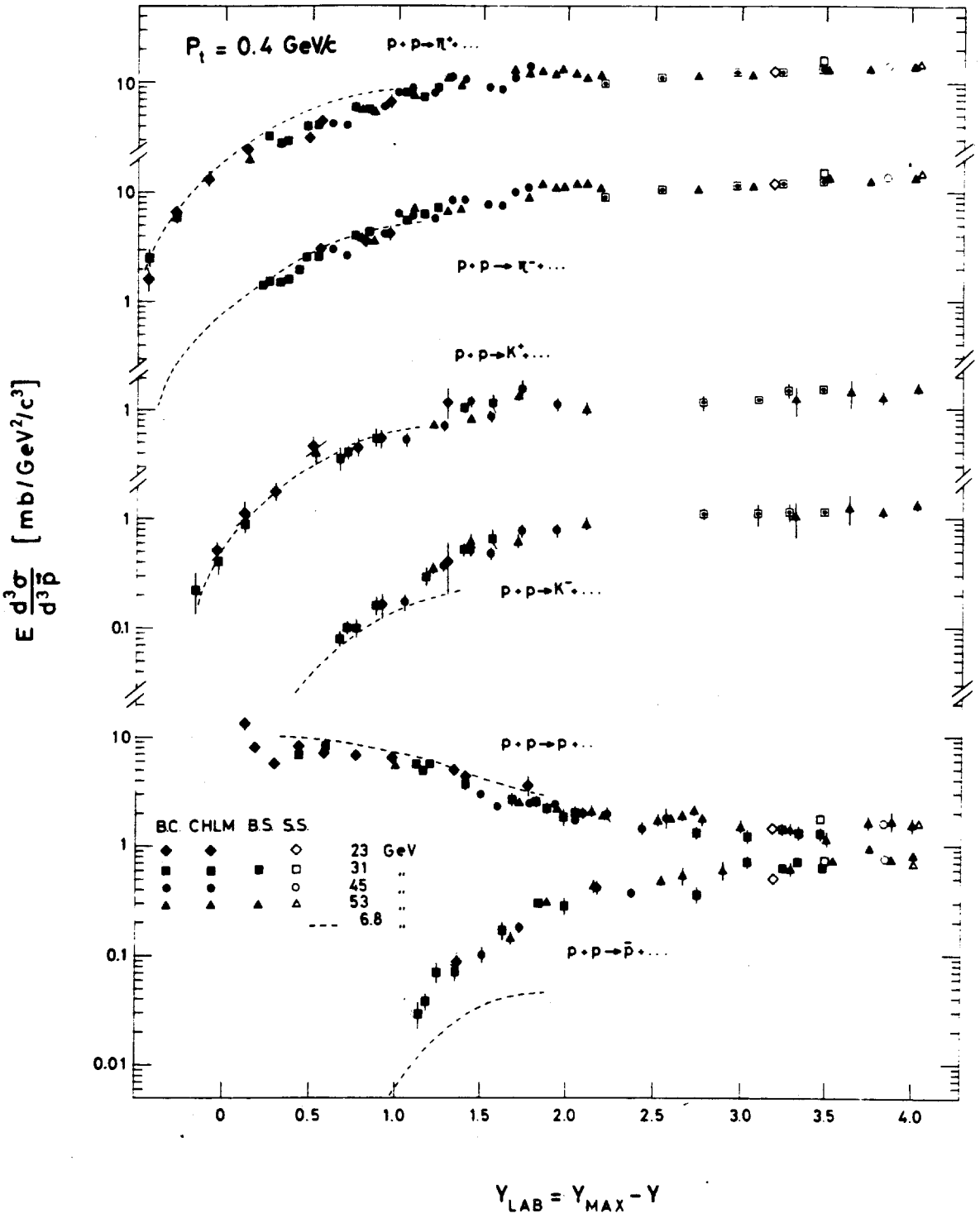

Fig. 27. The invariant cross section for $\pi^{\pm}$, $K^{\pm}$, and $p^{\pm}$ production in pp collisions plotted versus the laboratory rapidity for p_t=0.4 GeV/c (73A8). The dashed lines represent interpolations through the 24-GeV/c data of Allaby et al (72A1). The points are data at different ISR energies.

on a single curve, which has the appearance of Fig. 26 (b), but the "flat" part for $y_{lab} > 2$ is probably slowly rising with y_{lab}, by about 10% in 2 units of rapidity. This means that the scaling region has not quite been reached even at the highest ISR energies.

The shape of $f = f(y_{lab})$ at fixed p_t is essentially the same for $\pi^{\pm}$, $K^{\pm}$, and $\bar{p}$. Only the protons have a different shape, which reflects their leading particle nature. All the ISR data taken at different energies superimpose on the same curve; the data at the laboratory momentum of 24 GeV/c are considerably lower for $\bar{p}$, just a little bit lower for K^- and just a little higher for protons. This emphasizes the different ways in which the scaling region is reached, though the variations are modest when the data are plotted versus y_{lab}, which minimizes the nonscaling effects.

Figure 28 shows the cross section, divided by the inelastic cross section, for photon production at various ISR energies and for different values of the transverse momentum (72N1).

4.2.2 $f = f(x)$.

Figure 29 gives a compilation of data for the production of $\pi^{\pm}$, $K^{\pm}$, p, and $\bar{p}$ in pp collisions at 19 GeV/c (72A1) and of Λ^0 and K^0 at NAL (73D3). All cross sections have the same shape with the exception of protons.

Figure 30 shows the production cross sections of $\bar{p}$ at different ISR energies and for different transverse momenta (73A8). The dashed lines are interpolations of the 24-GeV/c data. Large differences exist between the production of antiprotons at the ISR and at 24 GeV/c.

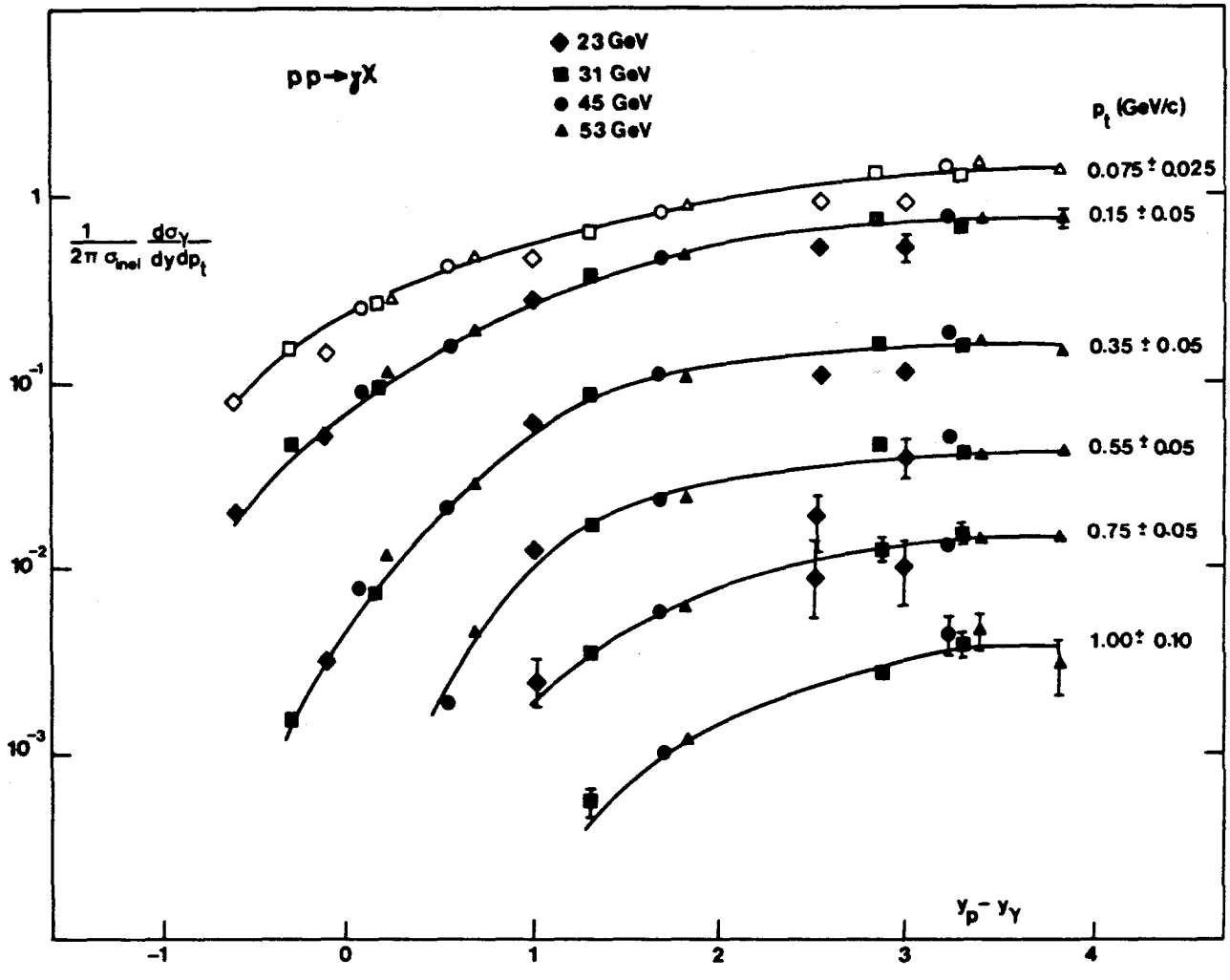

Fig. 28. The invariant cross section for photon production in pp collisions versus y_{lab} at different p_t values (7N1). The lines are eyeball interpolations of the data.

4.3 Particle Ratios.

Particle ratios, that is the ratio of the invariant cross sections for the production of different particles, are affected by larger statistical errors, but much smaller systematic errors than for the invariant cross sections themselves. In fact the corrections arising from absorption, multiple scattering,

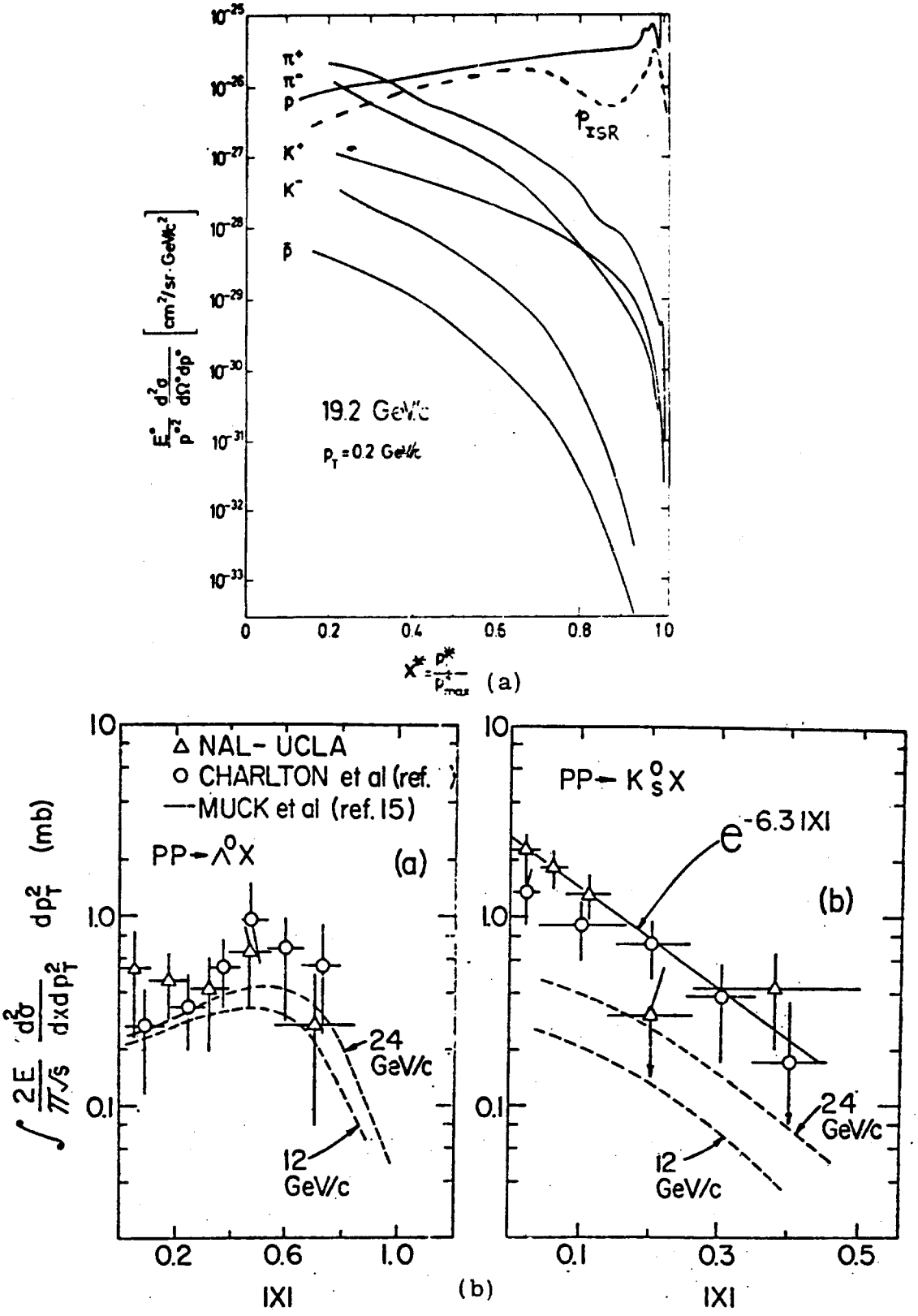

Fig. 29(a). Illustration of the x dependence of the invariant cross section for the production of $\pi^{\pm}$, $K^{\pm}$, and $p^{\pm}$ in pp collisions at 19.2 GeV/c and p_t=0.2 GeV/c. The situation at ISR energies is similar, apart from protons (dashed line) and from the increased number of K^- and $\bar{p}$. (b) The x dependence of Λ^0 and K^0 production at NAL energies.

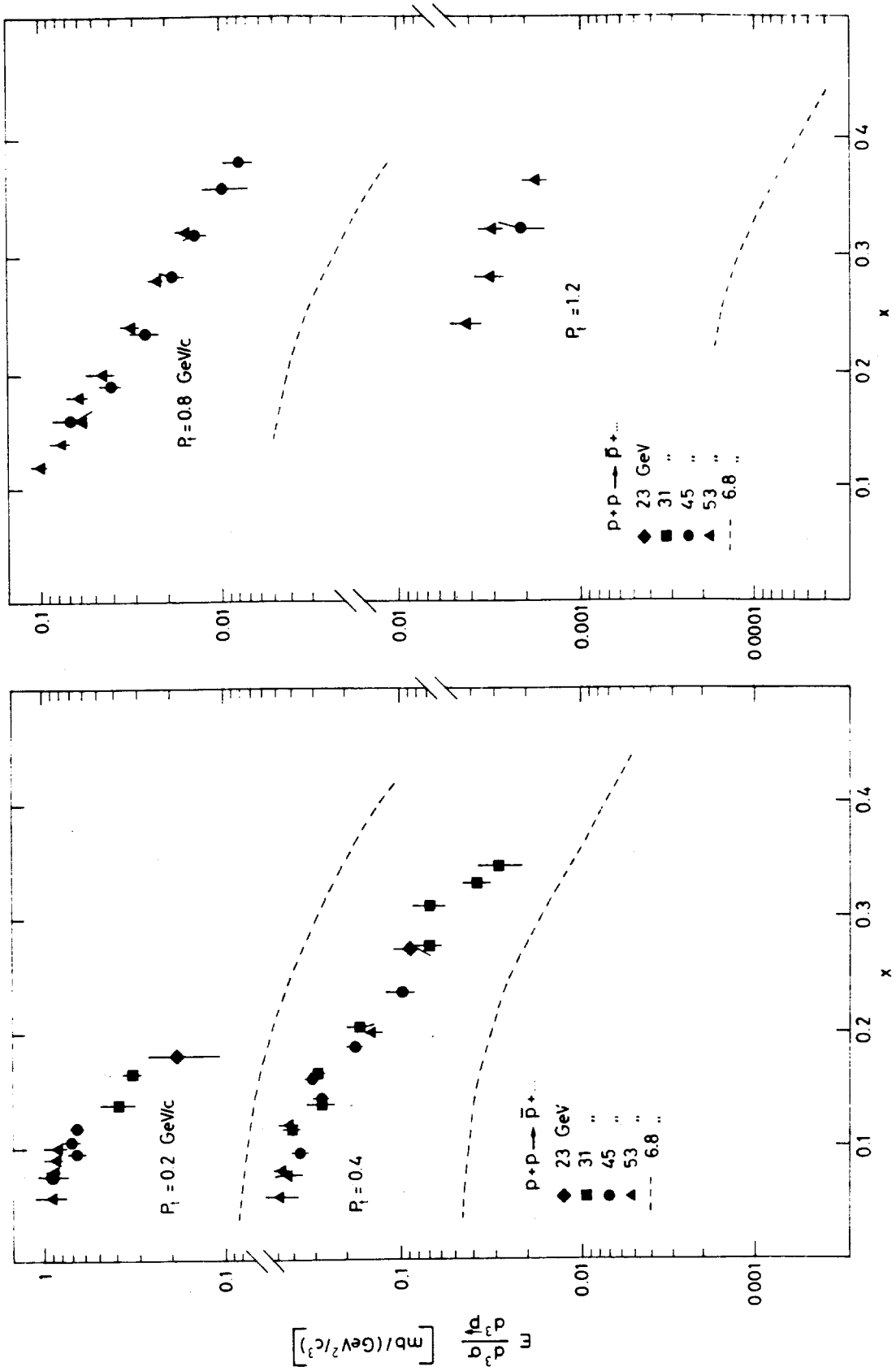

Fig. 30. The invariant cross section for p production in pp collisions at ISR energies and at p_t=0.2, 0.4, 0.8, and 1.2 GeV/c (73A8). The dashed lines are interpolations through 24-GeV/c data (72A1).

decay, etc. are smaller; moreover at the ISR, if the ratios are measured during the same beam stacks, there is no error arising from the luminosity determination.

Figure 31 shows the particle-to-antiparticle ratios at p_t = 0.4 GeV/c

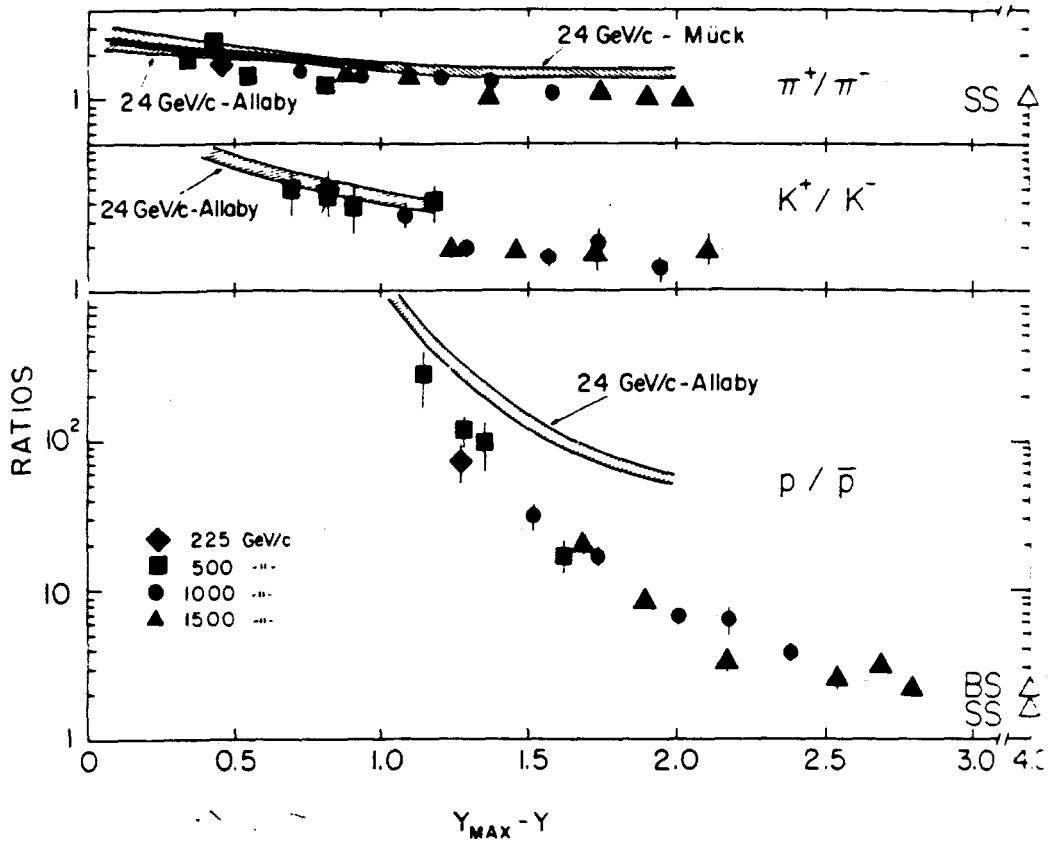

Fig. 31. The ratios of the invariant cross sections at p_t=0.4 GeV/c for π^+/π^-, K^+/K^-, and $p/\bar{p}$ for particle production in pp collisions plotted versus the laboratory rapidity (73A8). The dashed lines are the data at a laboratory momentum of 24 GeV/c (72A1).

plotted versus the laboratory rapidity. Figure 32 shows the particle-to-pion ratios plotted versus the x variable (73A8). All particle-to-antiparticle ratios decrease towards 1 as y_{lab} goes to the maximum value. (The asymptotic value should be 1.) The particle-to-pion ratios tend to a value around 0.1-0.2 as x goes to zero.

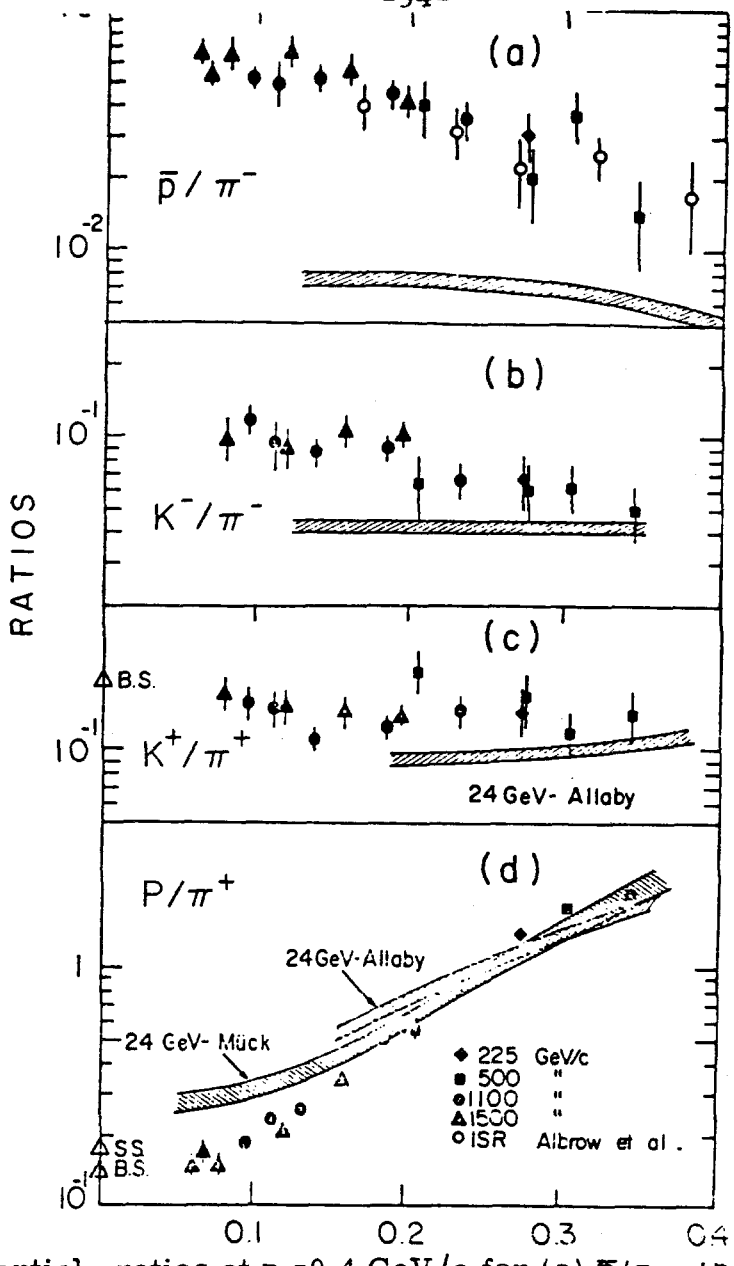

Fig. 32. Particle ratios at p_t=0.4 GeV/c for (a) $\bar{p}/\pi^-$, (b) K^-/π^-, (c) K^+/π^+, and (d) p/π^+ plotted versus the x variable (73A8). Dashed bands are data at p_{lab}=24 GeV/c (72A1), (72M2).

4.4 Energy Dependence - the Approach to Scaling.

The energy dependence of the invariant cross section is best studied with the internal target facility at NAL using the main beam on the jet gas target while the acceleration cycle is on. In this way one has available, in a continuous fashion, all laboratory momenta from 10 to 400 GeV/c. Figure 33

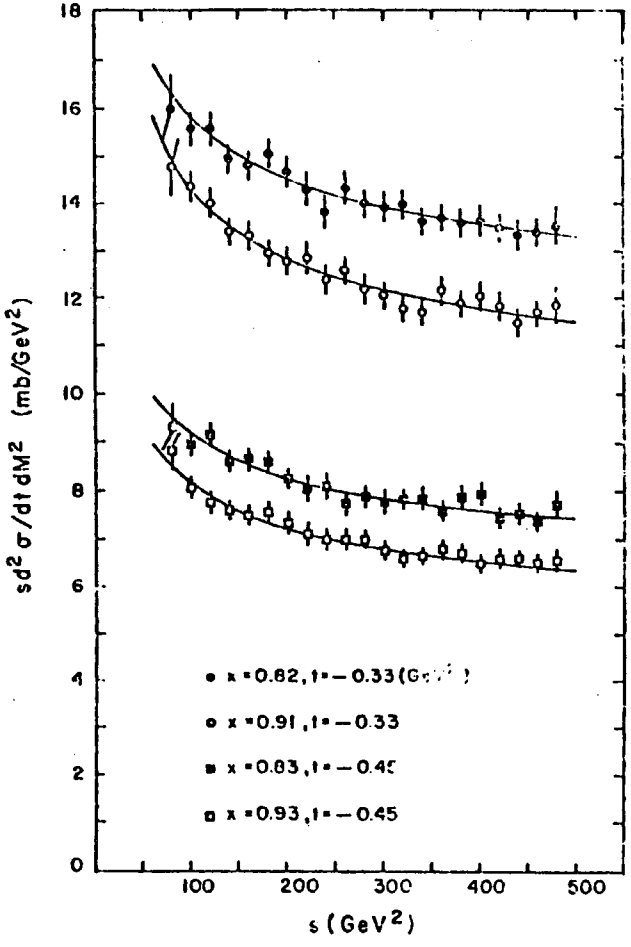

(a)

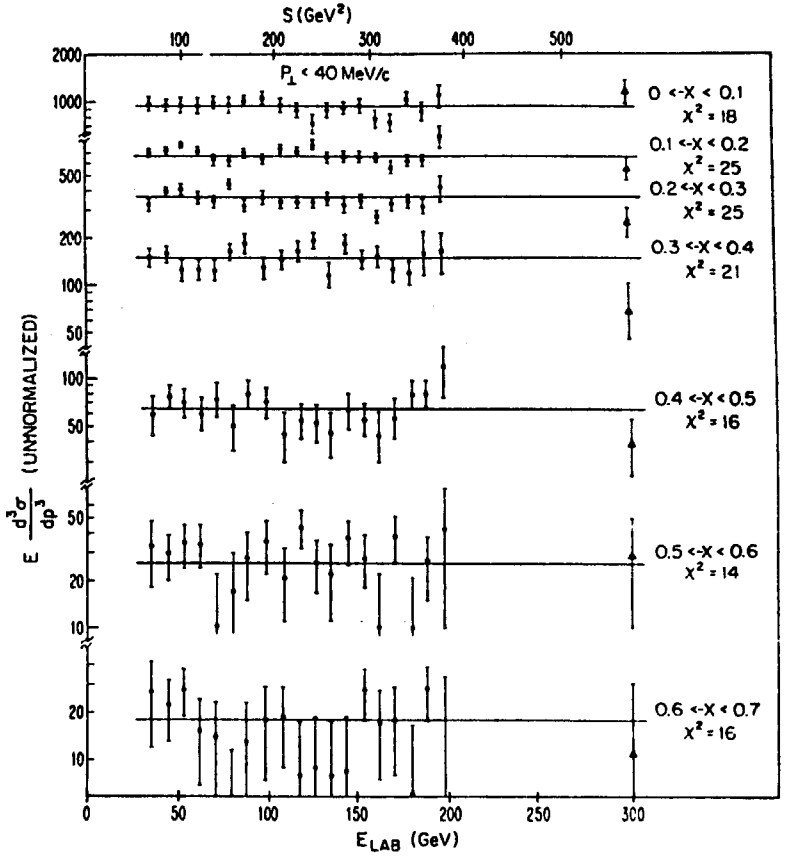

(b)

Fig. 33(a). The invariant cross section for proton production as function of s at two values of t and two values of x (73S1). The curves are fits to the data with a dependence a $(1+bs^{-1/2})$. (b) The invariant cross section for γ-ray production as function of laboratory momentum (72P1).

shows the invariant cross section for proton production at two values of t and two values of x (73S1). The cross section is decreasing while the energy increases, and the energy dependence slows down at higher energies. Only the cross section for the production of protons shows such a decreasing trend; for all other particles, the cross section increases with energy (see Fig. 34) until the energy dependence becomes weaker.

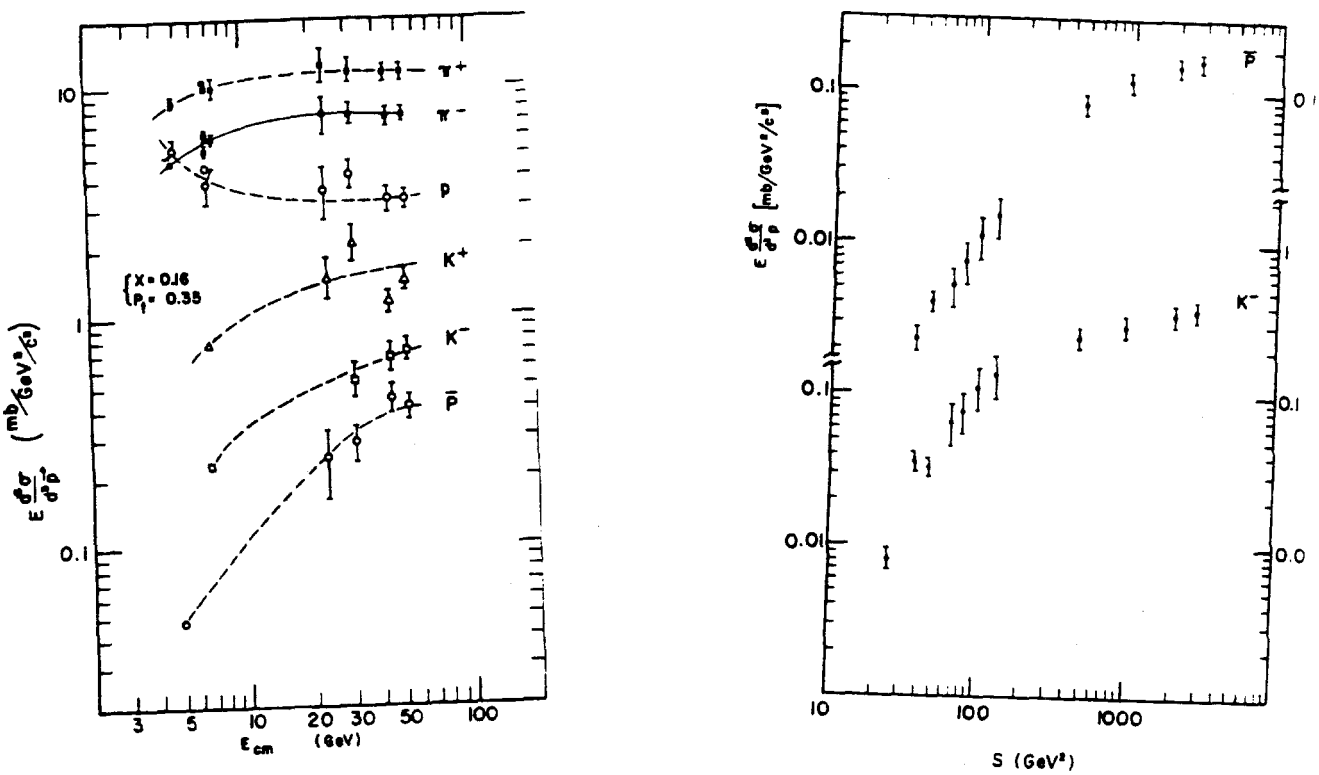

Fig. 34. The invariant cross section for $\pi^{\pm}$, $K^{\pm}$, p, and $\bar{p}$ production as a function of s at fixed values of x and p_t.

There are many ways to parametrize the energy dependence of the cross sections. Many authors quote formulae of the type

$$f = f(s) = a\left[1 + b\, s^{-1/2}\right]. \qquad (42)$$

Others prefer a ($s^{-1/4}$) dependence. At present one cannot really discriminate among the various energy dependences suggested. The importance of the problem lies in the fact that one could in principle discriminate among the various models of particle productions.

The analysis of the information presented indicates that:

(i) At ISR energies there is only a weak-energy dependence for all types of particles. Assuming that this is an indication of having almost reached the scaling region one may add:

(ii) the limiting distributions are reached at lower energies for pions and at higher energies for protons, kaons, and antiprotons;

(iii) the limiting distributions are reached first in the fragmentation region and later in the central region;

(iv) the limiting distributions are reached from below, with the exception of the leading particle;

(v) the average transverse momentum for each type of particle increases slowly with energy. The average transverse momentum for all particles combined grows a little bit faster because of the increased percentage contribution of heavier particles at higher energies (Fig. 35).

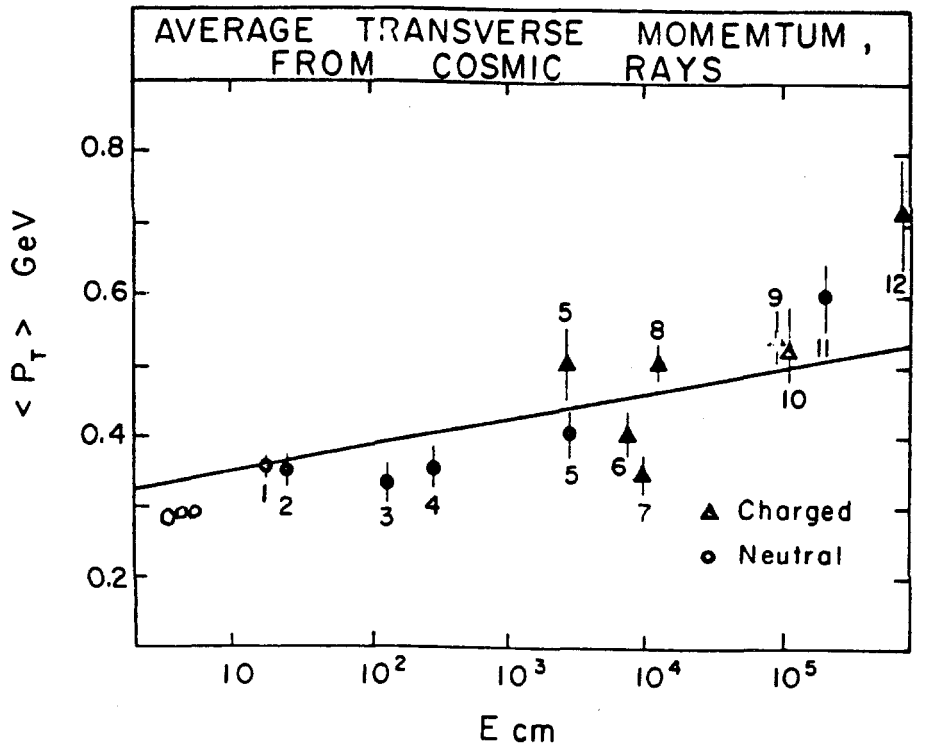

Fig. 35. The average transverse momentum as function of $\sqrt{s}$ (72M4).

4.5 Leading Particle Effects.

The protons produced in proton-proton collisions exhibit many features which arise from the fact that the incoming particles are protons. We have already mentioned several times the peculiarities of the proton spectra; here we shall summarize and complement these features.

4.5.1 The x-Distribution.

Figure 27 shows that the invariant cross section for proton production at ISR energies has a broad maximum between x = 0.3 and 0.7. Figure 36 shows that there is also a peak at x ≃ 0.99, very close to the elastic peak (73A3). In fact the separation of inelastic events from elastic ones is non-trivial; it is done by requiring noncollinearity with the proton on the other side of the proton whose angle and momentum are measured. The asymmetric

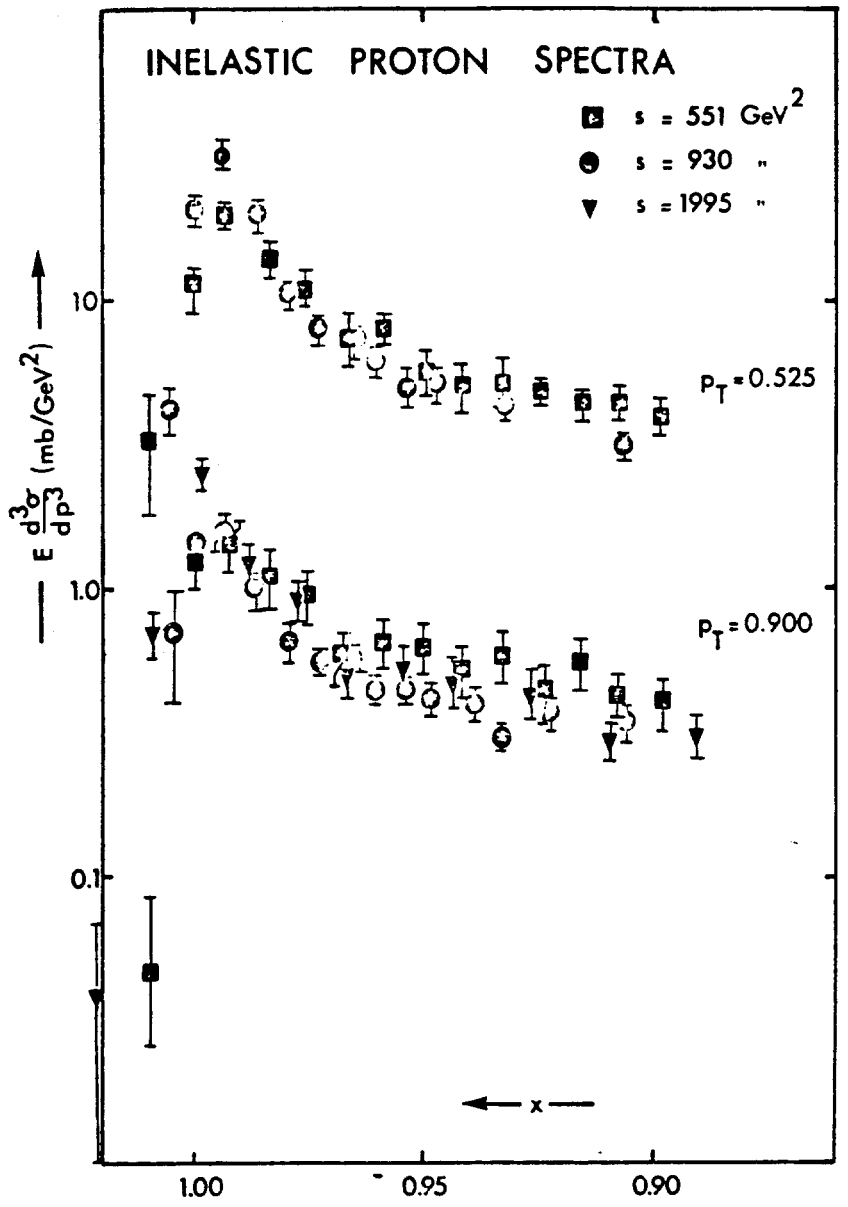

Fig. 36. The invariant cross section for proton production versus x (for x>0.9) (73A2), (73A3). The experimental resolution function was not unfolded.

shape of the peak of Fig. 37 reflects the spectrum of masses produced in the "opposite" hemisphere [according to the relation (25)]. Apart from minor differences suggesting that the range of masses produced grows with increasing s, the spectra at different energies look alike (see Fig. 36). In fact all known isobar masses would be in one bin, the top one, suggesting that either

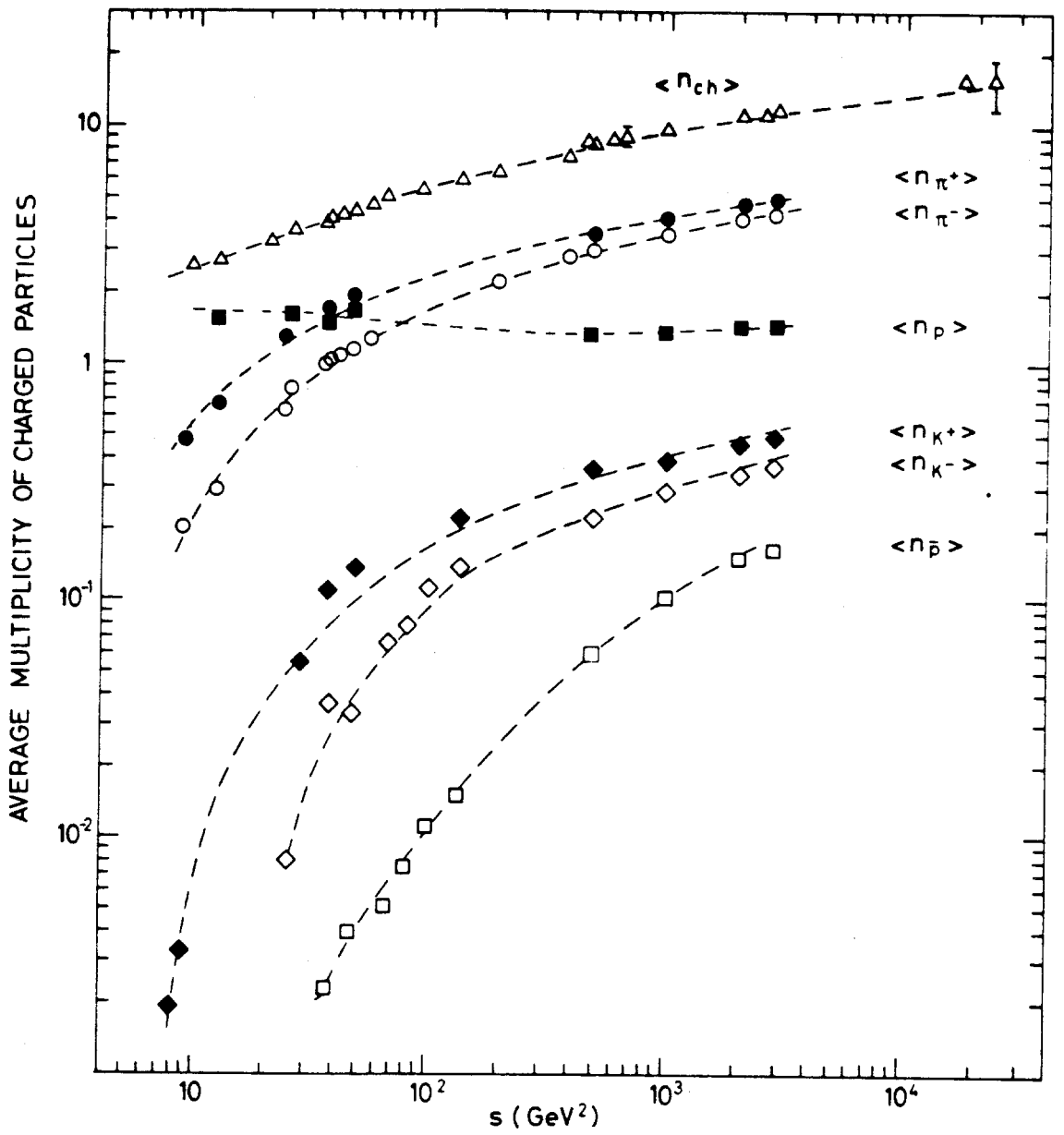

Fig. 37. The average multiplicity of π^-, π^+, K^-, K^+, $\bar{p}$, p, and $<n_{ch}>$ as a function of s (73A1). The dashed lines represent the results of the fits according to Eqs. (50) and (51).

one is exploring a large range of new masses or that one sees a new phenomenon. This last interpretation is favored in the triple-Regge exchange picture.

One may call the cross section under the peak diffractive, in the sense that it arises from the diffraction excitation of one nucleon. The value of this cross section for the single excitation of one of the two nucleons is about 5 mb

(and probably it grows by 0.5 mb between lowest and ISR energies). Thus it is as large as the elastic cross section. The cross section for the excitation of both nucleons can be estimated through factorization to be of the same size $\left(\sigma_D^2 \simeq \sigma_{DD}\sigma_{EL}\right)$. In order to obtain more information, one has to explore this mass region in greater detail with a much higher resolution, such as that provided by some NAL experiments. What one can say is that there may be interesting structure and that the slope of the differential cross section for these diffracted events is less steep than for the elastic ones (72I1).

4.5.2 The energy dependence for the low x region (Fig. 33) is anomalous compared to the other produced particles since the limiting distribution is reached from "above" and not from "below". Also the energy dependence of the peak at $x \simeq 0.99$ is anomalous, since the peak develops for laboratory momenta larger than 50 GeV/c.

4.5.3 The transverse momentum distributions are exponential for smaller x values and become gaussian for larger values of x. (See paragraph 4.1.1.) Also the average transverse momentum distribution is anomalous (see Fig. 22).

4.6 Multiplicities.

We shall define the multiplicity of particle c as the average number of particles c produced per interaction. Multiplicities may be computed either (a) from the direct measurement of the particles produced in each interaction or (b) by integration of single particle spectra in inclusive reactions. Case (a) is typical of bubble-chamber measurements. The multiplicity for the production of particle c is given by:

$$\langle n_c \rangle = \frac{\Sigma_k \, k \sigma_k(c)}{\sigma_{in}} \tag{43}$$

where σ_k (c) is as in Eq. (30) the exclusive cross section for producing k times the c particle; σ_{in} is the inelastic cross section. The total multiplicity $\langle n \rangle$ is then

$$\langle n \rangle = \langle n_{ch} \rangle + \langle n_n \rangle = \sum_c \langle n_c \rangle \tag{44}$$

where $\langle n_{ch} \rangle$ and $\langle n_n \rangle$ are the total charged and neutral multiplicities respectively; $\langle n_{ch} \rangle$ may be obtained more simply as

$$\langle n_{ch} \rangle = \frac{\sum_{n=1}^{n_{max}} n\sigma_n}{\sigma_{in}} \tag{45}$$

where σ_n is the topological cross section for the production of events with n-charged secondaries.

In the method (b) one has to integrate single-particle spectra. The multiplicity for each type of particles is now

$$\langle n_c \rangle = \frac{1}{\sigma_{in}} \int f \frac{d^3p}{E} . \tag{46}$$

If factorization in (p_t, y_{lab}) holds the computation of (46) becomes particularly simple:

$$f(y, p_t) \simeq g(y)\, h(p_t) \simeq G(y) \exp(-Bp_t) \tag{47}$$

from which

$$\langle n_c \rangle \simeq \frac{\pi}{\sigma_{in}} \int_0^{\infty} \exp(-Bp_t) \, dp_t^2 \int_{y_{min}}^{y_{max}} G(y)dy = \frac{4\pi}{\sigma_{in} B^2} \int_0^{y_{max}} G(y)dy . \qquad (48)$$

We know that the average transverse momentum changes with y_{lab} [and that $f = f(y_{lab})$ is not constant, particularly at small y_{lab}]. Thus Eq. (47) is not exact; however, it may still be used as an empirical formula and still yields reasonable results if average values of the transverse momentum are used (by averaging for instance in the graphs of Fig. 23). Since the y_{lab} distributions at $p_t = 0$ are not known, we have to use those at $p_t = 0.4$ GeV/c, thus modifying Eq. (48) to

$$\langle n_c \rangle \simeq \frac{4\pi}{\sigma_{in} B^2} \int_0^{y_{max}} \frac{f(y, p_t=0.4)}{\exp(-0.4B)} \, dy. \qquad (49)$$

The integral in (49) is computed numerically, using $\sigma_{in} \simeq 32$ mb independent of energy (in view of rising total cross sections also this number has to be changed and made energy dependent). Even with these limitations, the multiplicities are accurate to $\pm 10 \div \pm 15\%$; one has to check a posteriori if the computations yield results in agreement with charge conservation.

Figure 37 shows the multiplicities of π^-, π^+, K^-, K^+, $\bar{p}$, p, and the total charged multiplicity as function of s (73A1). $\langle n_{\pi^o} \rangle$ falls between $\langle n_{\pi^+} \rangle$ and $\langle n_{\pi^-} \rangle$ (72N1).

Most theoretical models predict that the energy dependence of the multiplicities is of the ($\ln$ s) type in the high-energy region, while at low energies

it should be of a power type, s^{α}. Many types of formulae combining both the $\ln s$ and s^{α} dependences have been used to fit the multiplicities over the complete range of energies. We shall discuss only dependence of the types:

$$\langle n_c \rangle = A + B \ln s + C s^{-1/2} \tag{50}$$

$$\langle n_c \rangle = A' + B' \ln s + C' s^{-1/2} \ln s. \tag{51}$$

The results of the fits are shown in Table IV.

Table IV. Results of the Least Squared Fitting of the Multiplicities to the Formulae (50) and (51).

	A (A')	B (B')	C (C')	X^2/D_oF	Eq.
$\langle n_{\pi^+} \rangle$	-1.7 ±0.3	0.84 ±0.07	1.0 ±0.5	0.3	(50)
$\langle n_{\pi^-} \rangle$	-2.6 ±0.2	0.87 ±0.05	2.7 ±0.4	0.4	(50)
$\langle n_{K^+} \rangle$	-0.50 ±0.03	0.13 ±0.01	0.65 ±0.05	1.1	(50)
$\langle n_{K^-} \rangle$	-0.52 ±0.04	0.11 ±0.01	0.80 ±0.06	0.7	(50)
$\langle n_p \rangle$	-2.0 ±4.0	0.4 ±0.5	4.0 ±4.0	0.2	(51)
$\langle n_{\bar{p}} \rangle$	-1.2 ±0.1	0.15 ±0.02	1.1 ±0.1	0.3	(51)
$\langle n_p \rangle$	-0.33 ±0.04	0.059 ±0.006	0.75 ±0.10	1.2	(50)
$\langle n_{ch} \rangle$	-3.8 ±0.4	1.88 ±0.07	6.4 ±0.7	1.9	(50)

Slightly better fits were generally obtained with Eq. (50), except for protons and antiprotons. The proton fits yield large errors because of their flat behavior in the present energy range; on the other hand, the fit is physically meaningful because it anticipates an increase of the multiplicity at high energies.

From the analysis of the multiplicities and of the fits we can make the following comments:

(i) The average multiplicity $\langle n_{\pi^+} \rangle$ is larger than $\langle n_{\pi^-} \rangle$. The difference between ($\langle n_{\pi^+} \rangle$ and $\langle n_{\pi^-} \rangle$ is constant, $\langle n_{\pi^+} \rangle - \langle n_{\pi^-} \rangle \simeq 0.6$), thus the percentage difference is decreasing with increasing energy. The same trend exists for K^+ and K^- with ($\langle n_{K^+} \rangle - \langle n_{K^-} \rangle$) $\simeq$ 0.1.

(ii) The proton multiplicity has a small energy dependence. Starting with the threshold value, it decreases with increasing energy, reaches a minimum, and then increases logarithmically. This behavior may again be considered a leading particle effect. The difference in proton multiplicity between the lowest and highest ISR energies is roughly accounted for by the increase in the number of antibaryons, in particular of antiprotons.

(iii) Except for protons, the increase of multiplicities at low energies is faster than a $\ln s$ behavior. This "threshold effect" is taken into account with equations like (50) and (51). Both formulae seem to fit well the multiplicities over the explored range of energy.

(iv) The coefficient B of the logarithmic term in Eq. (50) decreases with the increasing mass of the observed particle, with the exception of protons; particles and antiparticles seem to have the same values of B.

(v) The energy dependence of the average charged multiplicity $\langle n_{ch} \rangle$ is better represented by Eq. (50) than Eq. (51).

(vi) At a total c.m. energy of 53 GeV ($p_{lab} \simeq 1500$ GeV/c) the total multiplicity is:

$$\langle n \rangle = \langle n_{ch} \rangle + \langle n_n \rangle \simeq 12 + 6 \simeq$$

$$\simeq 5\pi^+ + 4.6\pi^0 + 4.3\pi^- + 0.5K^+ + 0.4K^- + 1.4p + 0.2\bar{p} + 0.8n + 0.04\Lambda^0 + 0.04Y^{\pm} + \ldots \qquad (52)$$

The total multiplicity is not as large as energy conservation would allow. Moreover even at $E_{cm} = 53$ GeV/c, the average number of each type of particle, excluding pions, is small; one cannot really apply statistical considerations.

4.7 Topological Cross Sections.

A considerable amount of information may be obtained by studying topological cross sections for charged particle production in a bubble chamber. At a single energy, one may measure:

(i) The average number of charged prongs $\langle n_{ch} \rangle$, defined in Eq. (45);

(ii) Higher order absolute moments

$$\langle n_{ch}^2 \rangle, \langle n_{ch}^3 \rangle, \ldots, \langle n_{ch}^k \rangle. \tag{53}$$

(iii) The C parameters

$$C_k = \frac{\langle n_{ch}^k \rangle}{\langle n_{ch} \rangle^k}. \tag{54}$$

(iv) The central moments of the distribution

$$\mu_k = \langle (n_{ch} - \langle n_{ch} \rangle)^k \rangle. \tag{55}$$

(v) The width of the distribution

$$D = \left(\langle n_{ch}^2 \rangle - \langle n_{ch} \rangle^2 \right)^{1/2} = \sqrt{\mu_2}. \tag{56}$$

(vi) The asymmetry of the distribution, measured by the skewness.

$$\gamma_1 = \frac{\mu_3}{D^3}. \tag{57}$$

(vii) Other parameters like

$$\langle n_{ch}(n_{ch}-1)\rangle, \text{ etc.} \tag{58}$$

The moments of the distribution and the related parameters are sensitive to the tails of the multiplicity distribution. It is thus reasonable to define also other parameters which are more sensitive to the location of the center of the distribution. The moments of the multiplicity spectrum are important because they give a measure of any correlation which occur in the production of the charged particles.

Figure 38 shows the energy dependence of the topological cross sections

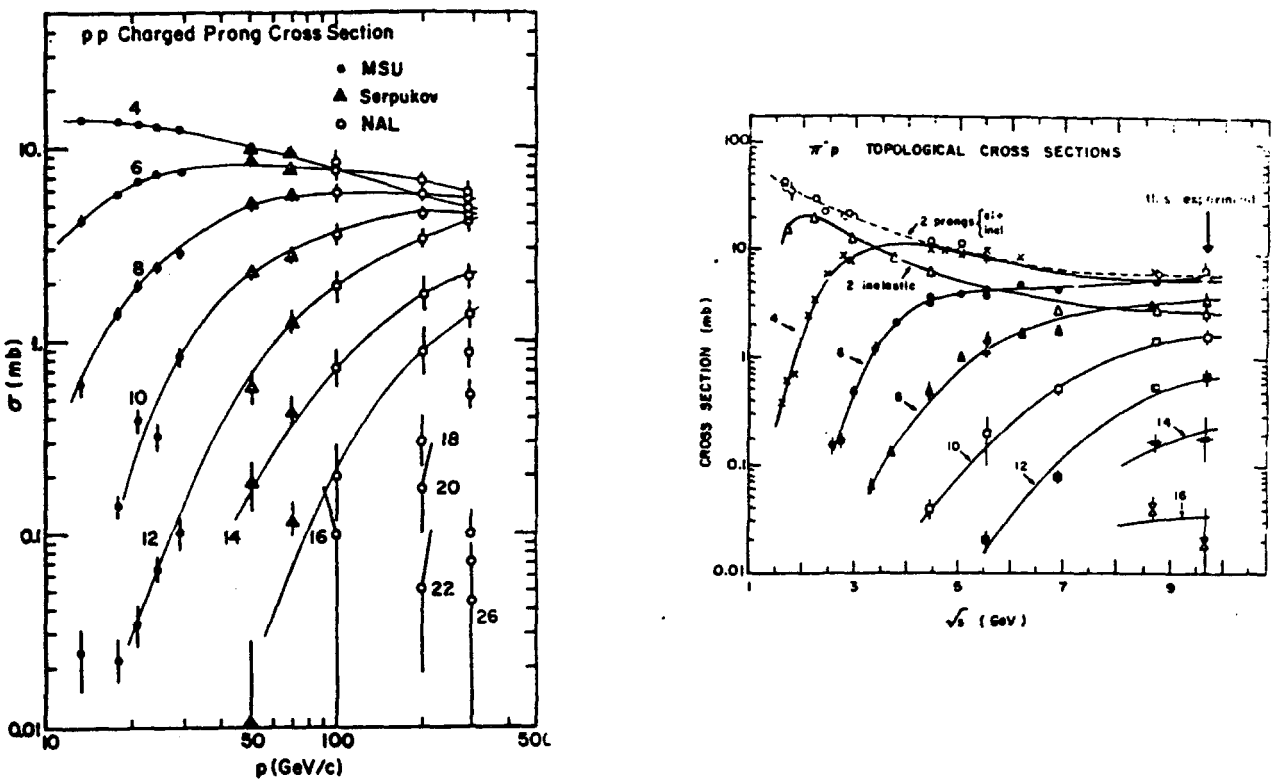

(a) (b)

Fig. 38. Charged prong cross section as function of laboratory momentum for pp and π^- p collisions (72J1), (73A9).

for different numbers of final charged particles (72J1). With increasing energy, the final state increases in complexity, with high multiplicity cross sections becoming more important than lower multiplicity ones. The energy dependence of the topological cross sections for a fixed number of prongs seems first to grow with energy, reaches a broad maximum, and then decreases. It is still an open question whether the topological cross sections will decrease to zero or reach some limiting non-zero values.

The rise of the large multiplicity cross sections and the slow fall of the low multiplicity cross sections yield a broadening of the multiplicity distribution. This was known to be somewhat narrower than a Poisson distribution in the $10 < p_{lab} < 30$ GeV/c range, while at 300 GeV/c it has become broader, as can be observed in Fig. 39 (73D3), (73D6). The energy dependence of the broadening may be summarized by the variation with energy of the coefficient

$$f_2 = \langle n_{ch}(n_{ch}-1)\rangle - \langle n_{ch}\rangle^2. \qquad (59)$$

f_2 should be zero for a Poisson distribution. Technically, one computes f_2^- on the basis of the negative tracks only. Figure 40(a) shows f_2^-, Fig. 40(b) shows the quantity

$$\frac{\langle n\rangle}{D} = \frac{\langle n_{ch}\rangle}{\left(\langle n_{ch}^2\rangle - \langle n_{ch}\rangle^2\right)^{1/2}} \qquad (60)$$

plotted versus energy. With increasing energy, $(\langle n\rangle/D)$, decreases towards a limiting value of $\simeq 2$. f_2^- starts up negative, crosses zero around 60 GeV/c, and then becomes positive. Finally, Fig. 40(c) shows various moments of

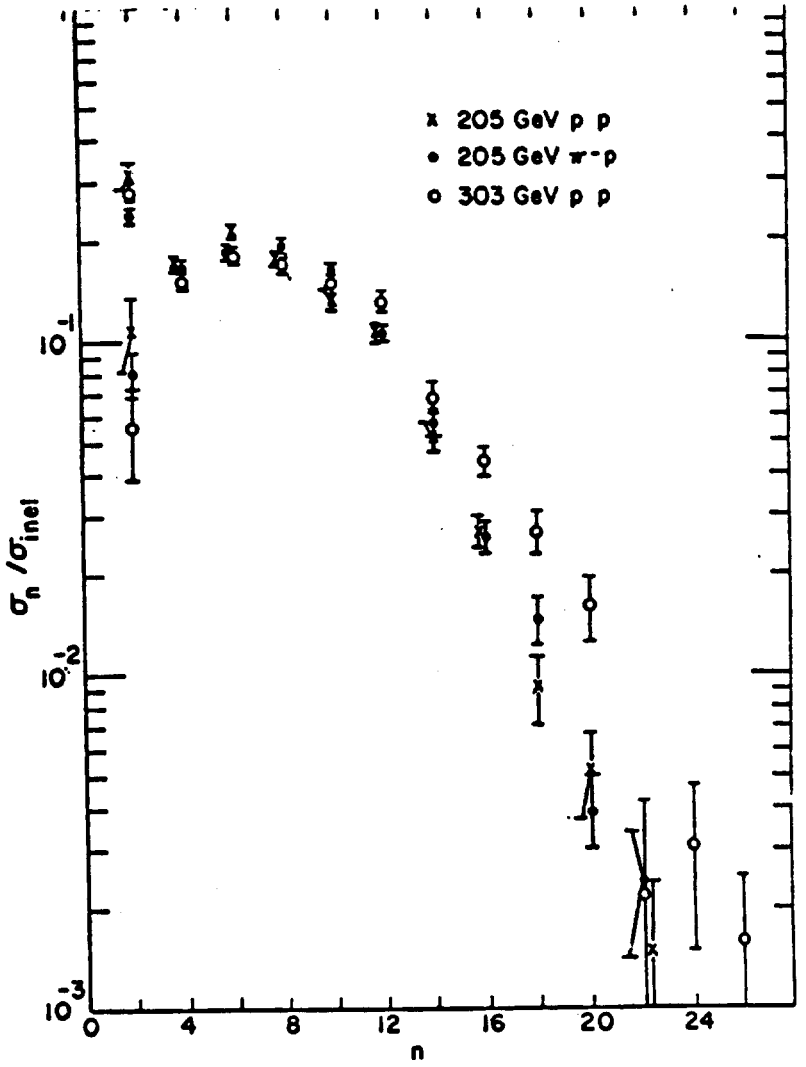

Fig. 39. Topological cross sections divided by σ_{in} for pp interactions at 205 and 303 GeV/c and $\pi^- p$ at 205 GeV/c. For n=2 the figure shows both the total and the inelastic two-prong cross sections.

n_{ch}. The experimental data from 4 to 300 GeV/c are consistent with the formula $D = (0.576 \pm 0.008)(\langle n_{ch} \rangle - 1)$.

There are in the literature many empirical formulae which fit the charged multiplicity distribution better than a Poisson distribution. Without entering into the technical aspects of the problem, we shall recall only the formula of Czyzewski and Rybicki.

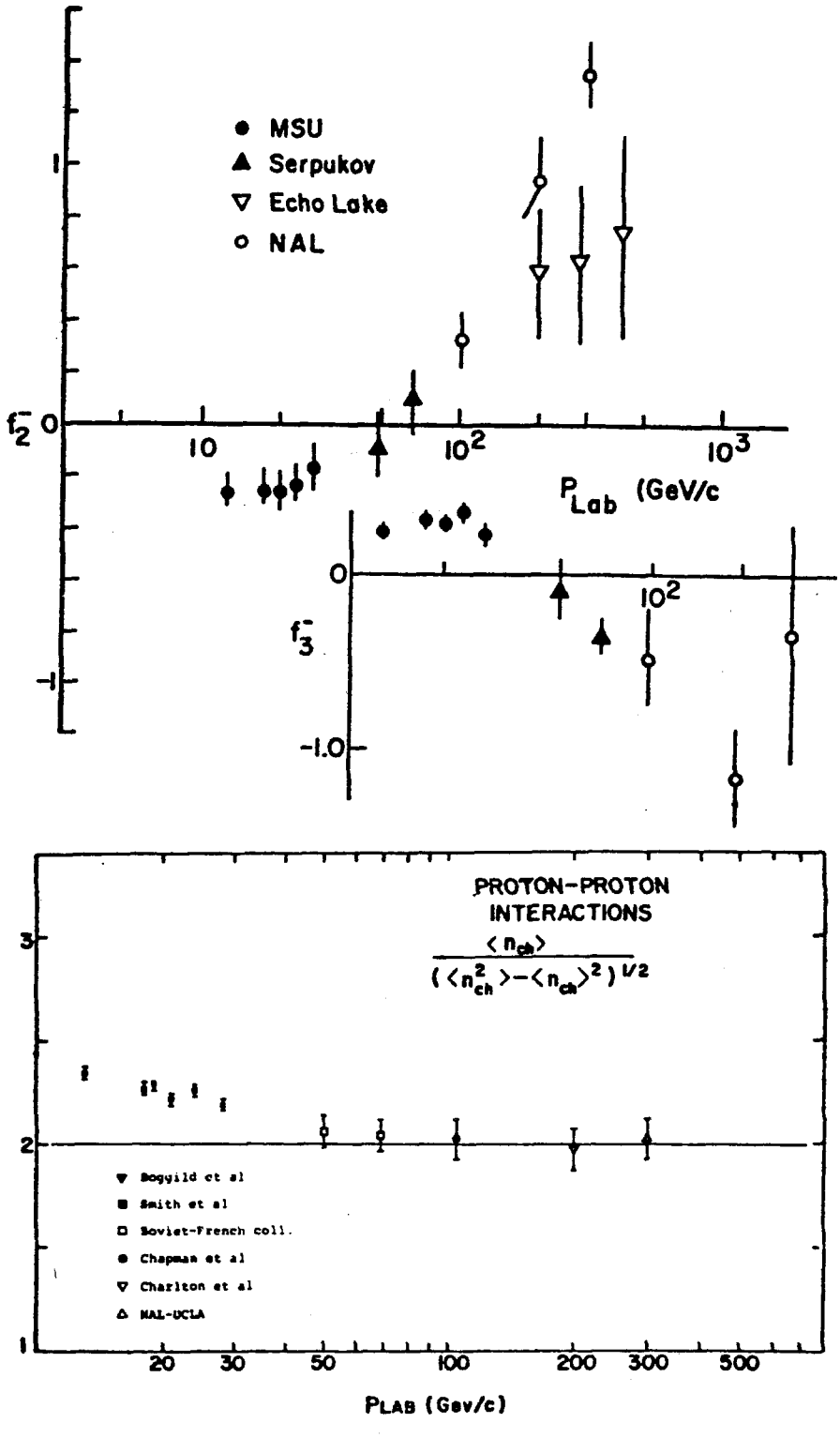

(a)

(b)

Fig. 40(a). Energy dependence of f_2^- and f_3^- (72J1). These coefficients were computed from the number of negative tracks. (b) Energy dependence of the mean charged multiplicity to the dispersion of the multiplicity distribution as a function of energy (72J1). (c) Energy dependence of $\langle n_- \rangle$, $\langle n_-^2 \rangle$, $\langle n_-^3 \rangle$, $\langle n_-^4 \rangle$, and $\langle n_-^5 \rangle$.

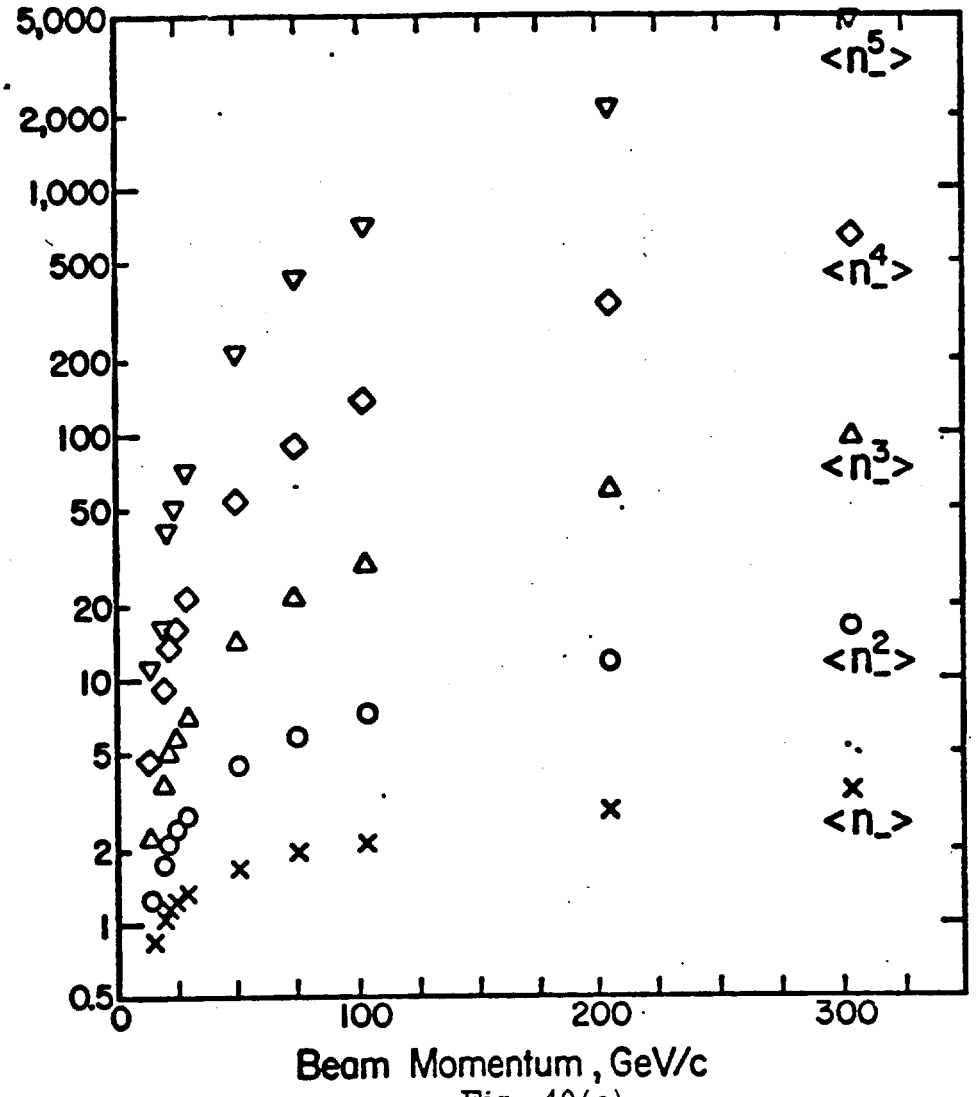

$$P_n = \frac{d^{2(2h-1)}}{\Gamma(h)} e^{-d^2} \tag{61}$$

where

$$h = d\frac{n_{ch}}{D} - d\frac{\langle n_{ch}\rangle}{D} + d^2 + 1. \tag{62}$$

$\langle n_{ch}\rangle$ and D are taken from the experimental results and d is the only parameter to be fitted ($d \simeq 1.7$ for pp interactions and $d \simeq 2.2$ for πp interactions).

Koba, Nielsen, and Olesen proposed a kind of a scaling law (KNO scaling) for the topological cross sections. In the limit of high energies one should have

$$\frac{\sigma_{n_{ch}} \langle n_{ch} \rangle}{\sigma_{in}} = \text{Function of } \left(\frac{n}{\langle n_{ch} \rangle} \right) \tag{63}$$

independent of energy. Figure 41 shows that Eq. (63) is well verified from

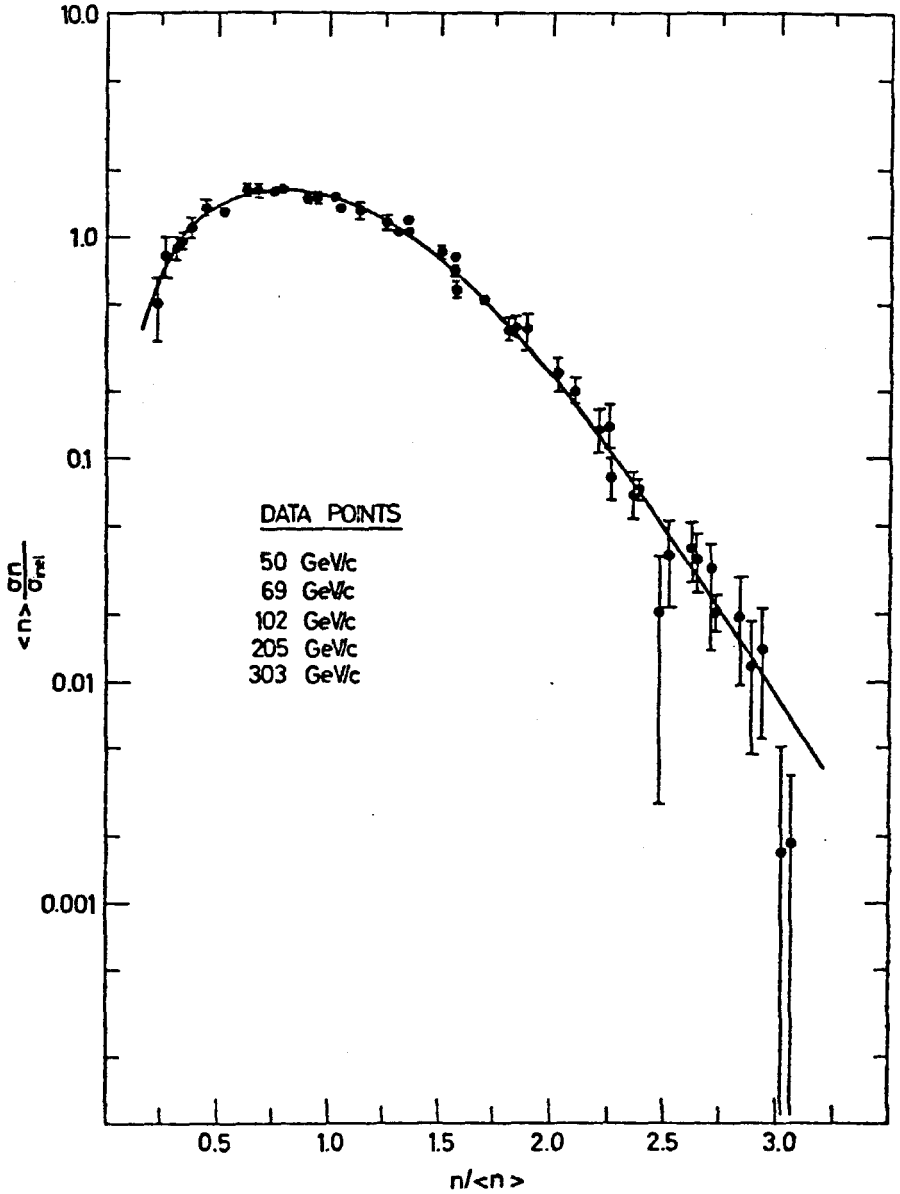

Fig. 41. Plot of $\langle n_{ch} \rangle \sigma_n/\sigma_{inel}$ versus $(n/\langle n \rangle)$ for charged particle production in pp collisions at incident laboratory momenta of 50, 69, 102, 205, and 303 GeV/c (72J1). The curve is an empirical fit to the data.

50 to 300 GeV/c. Eq. (63) is verified even when topological cross sections pertinent to a certain solid angle are considered. In fact, Eq. (63) is obtained assuming that scaling holds for semi-inclusive reactions, thus leading to a relation of the type

$$\langle n^q \rangle = C_q \langle n \rangle^q. \tag{64}$$

Such simple features as those discussed here are interesting, but as of now they do not lead to definite conclusions about which type of correlation dominates at high energy.

4.8 Correlations.

The study of correlations is a very large field of research, since the number of independent variables grows so much with the number of observed particles. In these lectures, we shall restrict ourselves to a superficial study of two-particle correlations in inclusive reactions at the very highest energies.

In analogy with the cross section for one particle inclusive distributions, Eq. (30), one has for the inclusive two-particle distributions

$$f^{(2)}(p_1, p_2) = \frac{1}{\gamma(s)} \sum_k k(k-1) \int \delta^4\left(p_a + p_b - \sum_{i=1}^{k} p_i\right) \frac{|M_k|^2}{k!} \prod_{i=3}^{k} (dp_i) \tag{65}$$

where p_1, p_2 are the four momenta of the two observed particles and the other symbols have the same meaning as in Eq. (30). From the above definitions one gets:

$$\iint f^{(2)}(p_1, p_2)\, dp_1 dp_2 = \langle n_{ch}(n_{ch}-1) \rangle \sigma_{in} \tag{66}$$

which may be considered to be the analog of Eq. (46) for one-particle distributions.

Sometimes it is more convenient to use inclusive densities defined as:

$$\rho^{(1)}(p_1) = \frac{f^{(1)}(p_1)}{\sigma_{in}} \tag{67}$$

for one-particle distributions and

$$\rho^{(2)}(p_1, p_2) = \frac{f^{(2)}(p_1, p_2)}{\sigma_{in}} \tag{68}$$

for two-particle distributions. From these one defines correlation functions as

$$C^{(2)}(p_1, p_2) = \frac{\rho^{(2)}(p_1, p_2) - \rho^{(1)}(p_1)\,\rho^{(1)}(p_2)}{\rho^{(1)}(p_1)\,\rho^{(1)}(p_2)} \tag{69}$$

$$C = \frac{\frac{1}{\sigma_{in}}\frac{d^2\sigma}{dy_1 dy_2} - \frac{1}{\sigma_{in}^2}\frac{d\sigma}{dy_1}\frac{d\sigma}{dy_2}}{\frac{1}{\sigma_{in}^2}\frac{d\sigma}{dy_1}\frac{d\sigma}{dy_2}} . \tag{70}$$

We shall only discuss the experimental results obtained at the CERN-ISR by the Pisa-Stony Brook collaboration (73B3). They measured charged particle production, measuring only angles. There is no knowledge of momenta nor of the sign or mass of the particles. The final state is thus somewhat poorly known, but in a sense this is an advantage because it reduces the number of independent variables to be used for the analysis. The polar angle of each particle may be related to the rapidity using the approximate formula (13). Thus correlation studies in "rapidity" may be performed.

It was found that the doubly differential cross section $d^2\sigma/dy_1\, dy_2$ scales at ISR energies.

Figure 42 gives the average multiplicity of the particles going inside a certain counter hodoscope in the direction of beam 1 (right) versus the multiplicity observed in the opposite direction. The graph suggests an almost flat distribution indicating that the forward going proton fragments in a way almost

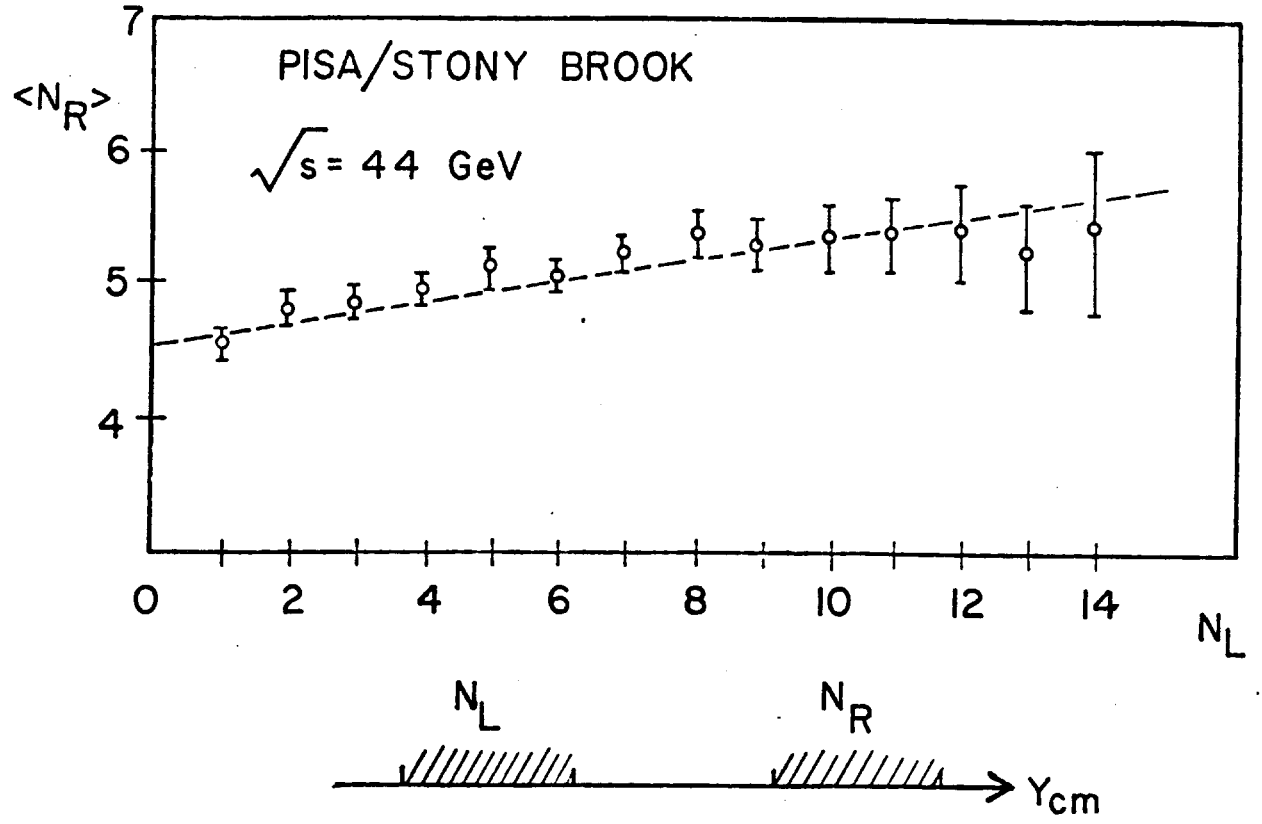

Fig. 42. In the c.m. the secondaries from pp collisions may be separated in two separate groups, those moving in the direction of beam 1 (right) and those moving in the direction of beam 2 (left). Here the average multiplicity of the first group, $<n_r>$, is plotted versus the multiplicity observed in the opposite direction, n_l (73B3).

independent of the backward proton. Of course, the same is true for the backward-going proton. C has a weak dependence on event multiplicity.

Figure 43 shows the "rapidity" correlation between the charged

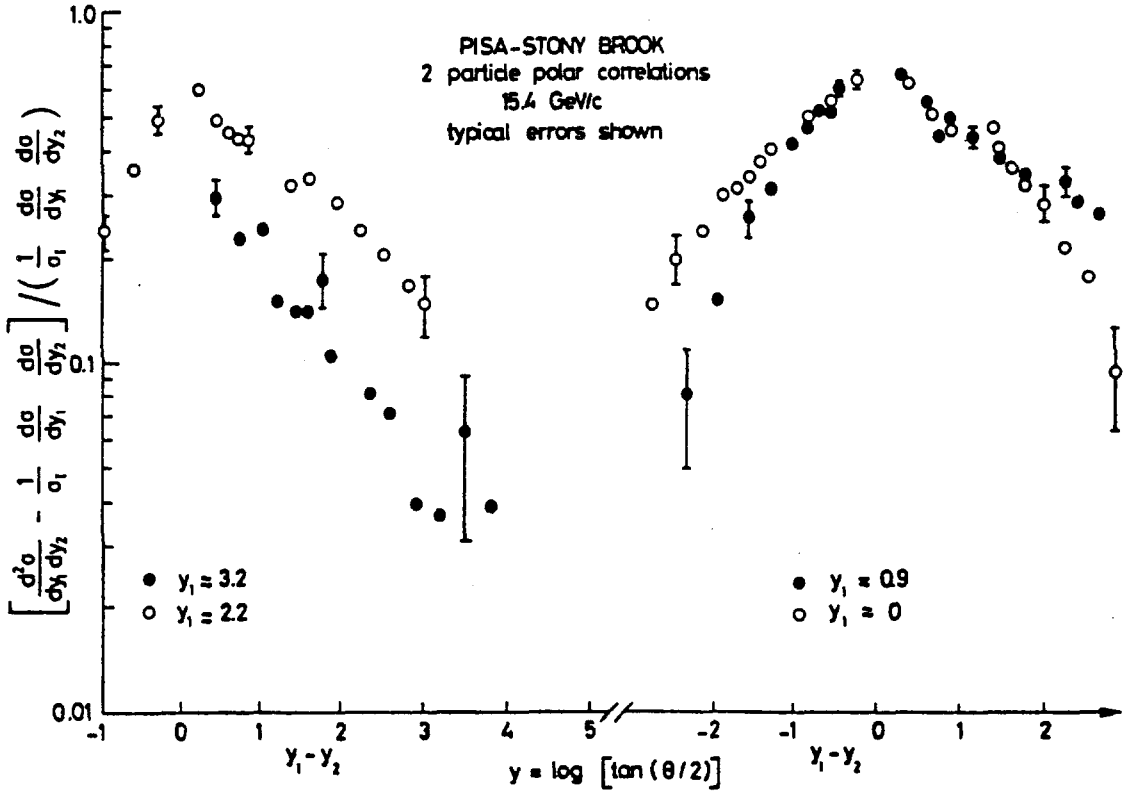

Fig. 43. Rapidity correlations between two charged secondaries as a function of their rapidity difference. Different symbols refer to different values of the rapidity of the first particle observed (73B3).

secondaries as a function of the difference in rapidity. This is done for different values of the rapidity of the first particle. It may be observed that:

(i) the correlation function has an exponential shape in $(y_1 - y_2)$ on both sides of $y_1 - y_2 = 0$, and centered at $y_1 - y_2 = 0$.

(ii) the slope of the correlation function is about 2, essentially independent of the value of y_1 ($y_1 = 0,\ 0.9,\ 2.2,\ 3.2$), but slowly dependent on energy.

These facts suggest that there is a strong short-range correlation in the rapidity variable, both in the central and fragmentation regions. It is not yet clear if long-range corrections really exist. In fact the available range in rapidity is probably not large enough for a proper study of these correlations.

4.9 Production of $\bar{d}$ and Heavier Antinuclei.

It is interesting to discuss also the production of antideuterons and the search of new particles at Serpukhov, NAL, and at the ISR.

The ratio $\bar{d}/\pi^-$ is found to be of the order of 10^{-4} at $E_{cm} = 53$ GeV (and $p_t = 0.7$ GeV/c and $x \simeq 0$. At Serpukhov energies: $\bar{d}/\pi^- \simeq 2 \times 10^{-6}$ while at BNL-AGS the ratio is 3×10^{-7} (71A3). Thus there is a considerable increase in $\bar{d}$ production as the energy grows.

Figure 44 shows the production of $\bar{p}$, $\bar{d}$, and $\overline{He}^3$ in p-nuclei collisions

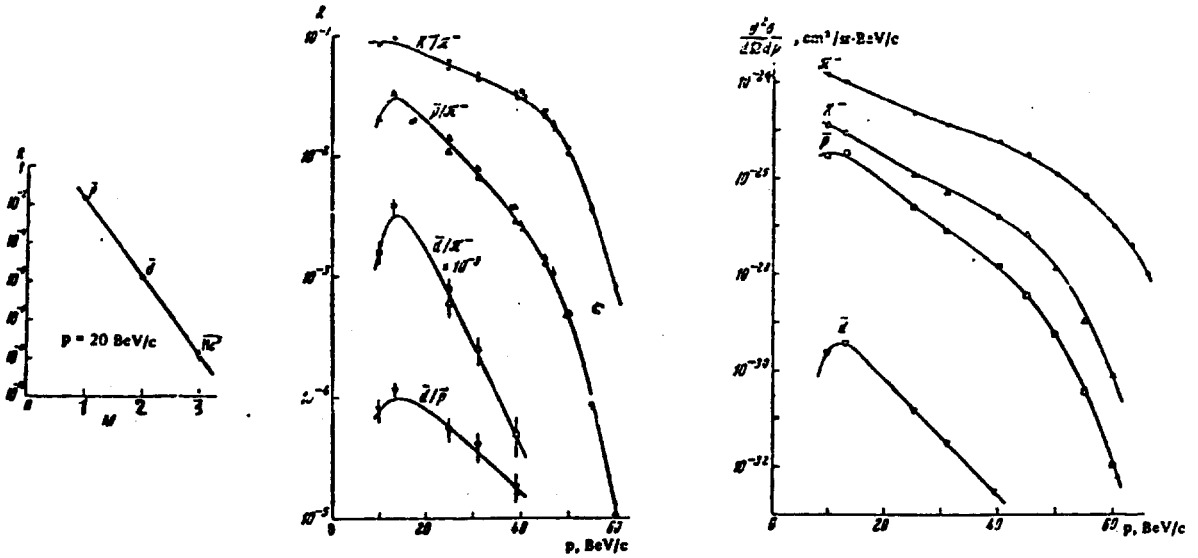

(a) (b) (c)

Fig. 44(a). Ratio of differential cross sections for production of $\bar{p}$, $\bar{d}$, and $\overline{He}^3$ relative to π^- at the 76 GeV IHEP accelerator at a secondary momentum of 20 GeV/c and a production angle of 27 mrad (71A2). (b) Particle ratios, and (c) absolute cross sections versus secondary momentum (71A3).

at p_{lab} = 70 GeV (71A2). The very strong dependence on the mass of the detected particles is of an exponential type. The detection of $\overline{He}^3$, $\bar{t}$, and heavier nuclei is at the limit of the experimental possibilities because of the small rate of production and of the high-rejection ratios required.

5. INCLUSIVE REACTIONS INITIATED BY π, γ, ETC.

In the laboratory-momentum range of 10 to 30 GeV/c there exists a wealth of information on particle production in $\pi^{\pm}p$, $K^{\pm}p$, and $\bar{p}p$ collisions. Most of the data come from bubble-chamber experiments (in some cases from the reanalysis of old films). The features observed in these experiments are quite similar to those observed in pp collisions. The differences arise from the fact that the pp system is made of two identical particles, while it is not so for the other cases. This brings about a forward-backward asymmetry between data at negative and positive x values. As a consequence people often search for a system of reference where such an asymmetry becomes minimal or zero.

Other comments and differences arise if one considers the system $ab\bar{c}$ (for the inclusive reaction $a + b \rightarrow c + X$). It seems that if $ab\bar{c}$ is an exotic system the limiting distributions are reached at lower energies than for a non-exotic $ab\bar{c}$ system. It is also clear that at these relatively low energies one has to watch out for kinematical limitations of various sort.

As an example of lower energy non-pp data we shall briefly discuss the main features of a bubble-chamber experiment performed with a beam of polarized photons (obtained by backscattering a laser beam from the 18 GeV electron beam of the SLAC accelerator) (72M3). The scatter diagram of the

events in the $\left(p_t^2,\ y_{lab}\right)$ plane for the reaction

$$\gamma + p \rightarrow \pi^- + X \tag{71}$$

at 9.3 GeV, as shown in Fig. 45, clearly indicates the cutoff in p_t, the

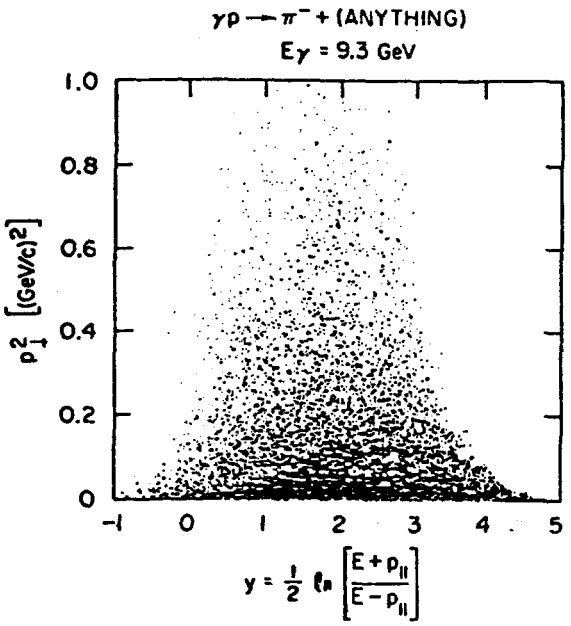

Fig. 45. Bidimentional diagram showing the density of events in the p_t^2, y_{lab} plane for the reaction $\gamma + p \rightarrow \pi^+ + X$ at 9.3 GeV (72M3).

available range in y_{lab}, and other features like the variation of the average transverse momentum with y_{lab}.

The x dependence of the invariant cross section is shown in Fig. 46, which also offers a comparison of the x distributions for π^- production in the reaction (71) and in the reactions

$$\pi^- p \rightarrow \pi^- + X \tag{72}$$

$$\pi^+ p \rightarrow \pi^+ + X \tag{73}$$

at slightly higher energies. The curves have been normalized to the respective total cross sections. The shapes of the x distributions are typical of all inclusive reactions at these intermediate energies. In particular there is

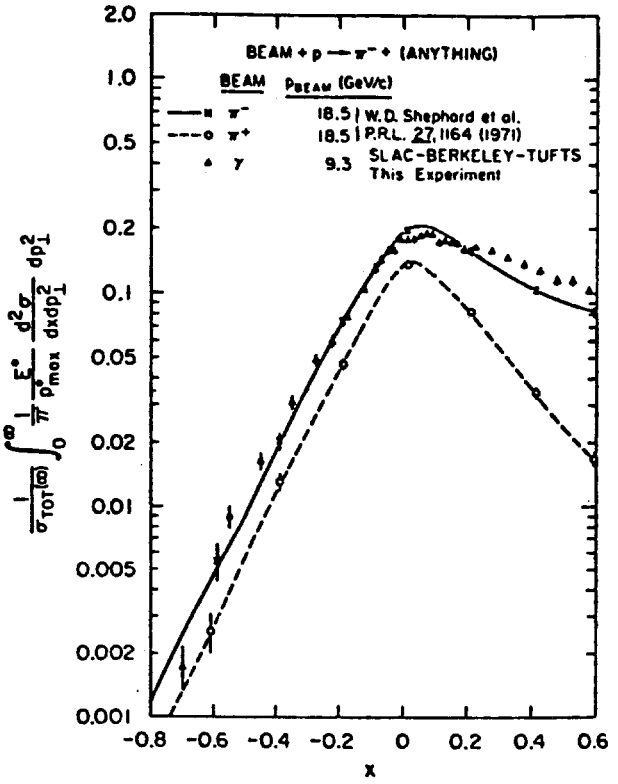

Fig. 46. A comparison of the x distributions for the reactions $\gamma p \to \pi^- + x$ and $\pi^\pm p \to \pi^- + x$ (72M3). Notice the normalization to the total cross section.

always the lack of symmetry around $x = 0$, which is due to leading particle and kinematical effects. For the inclusive reaction (71) the leading particle effects arise from the photoproduction of ρ^o

$$\gamma + p \to \rho^o + p \qquad (74)$$

which may be considered as the elastic process. The elimination of those events corresponding to ρ^o production reduces considerably the asymmetry in the x distribution by reducing the cross section for $x > 0$.

It is interesting to remark that after proper normalization the cross sections for π^- production in reactions (71) and (72) are essentially equal; both are a factor of two larger than the π^- production in (73).

The energy dependence for reaction (71) is weak; it may be parameterized with a formula ($A + B\, s^{-1/2}$), and it would seem that already at 9 GeV laboratory energy the scaling region is not too far away.

The dependence on the transverse momentum is of a gaussian type. It is found that the slope of the gaussian changes significantly with the number of prongs of the events, mainly because of phase-space effects.

Polarization effects. Since the incoming photons are 100% linearly polarized one may anticipate azimuthal correlations of the outgoing π^- with respect to the polarization vector of the incident photon. The authors find that for $x < 0.3$ there is no azimuthal dependence, while for $x > 0.3$ there is an azimuthal dependence of the form

$$\frac{d\sigma}{d\phi} = A + B \cos^2\phi \qquad (75)$$

with $B = 2.29 \pm 0.56$. At least one half of this correlation arises from the elastic ρ^o production (74).

6. THEORETICAL MODELS

We shall try to give a brief and simple-minded outline of the theoretical models used to describe particle production and try to compare them with experimental results (73C3).

Two approaches seem to have been followed to predict inclusive cross sections from a given model:

(i) the direct approach where the inclusive cross sections are obtained by summing the exclusive cross sections over the appropriate unobserved quantities;

(ii) The Mueller's approach where the inclusive cross sections, are obtained by considering appropriate discontinuities of the amplitudes for forward multi-particle elastic scattering.

These two approaches may be considered as complementary, the approach used depending on practical considerations and on the specific model considered.

The approach of Mueller is a generalization of the optical theorem, which relates the total cross section for the process a + b → anything (inclusive process of order zero) to the imaginary part of the forward scattering amplitude for the elastic process a + b → a + b. According to Mueller's hypothesis the cross section for the inclusive reaction (4) is connected to a certain discontinuity of the forward amplitude of the "elastic" three-body process

$$a + b + \bar{c} \rightarrow a + b + \bar{c}; \tag{76}$$

the situation is illustrated in Fig. 47; in formulae

$$f^{(1)}(p_c) = \frac{1}{\gamma(s)} D(p_a, p_b, -p_c) \tag{77}$$

where D is the discontinuity of the forward 3-body amplitude $M\left(s, t, M_X^2\right)$ taken across the cut of the missing mass variable M_X^2. This generalization of the optical theorem is in reality a subtle one, since the forward amplitude is not evaluated in its physical region because we have to insert the momentum of particle c and replace with its antiparticle $\bar{c}$.

Several models have been developed to describe inelastic reactions. Some are based on very general ideas, others are more phenomenological and may describe specific properties of the experimental data. Most models have

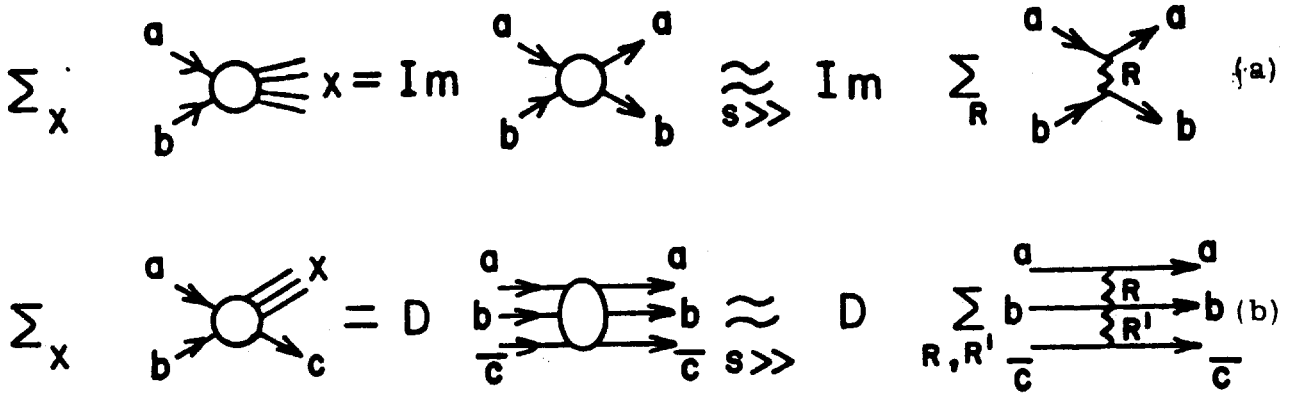

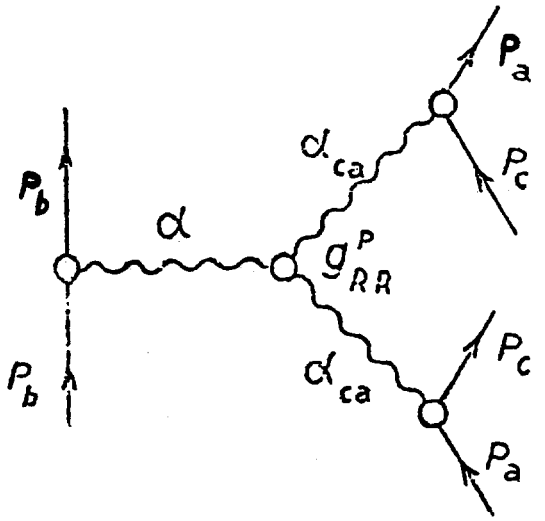

Fig. 47. Illustration of Mueller's approach of describing the inclusive one particle cross section as a discontinuity of the forward elastic three-body amplitude. (a) The graphs of Fig. 1(a) refer to total cross sections and elastic scattering. (b) The graphs of Fig. 1(b) refer to inclusive cross sections and three-body "elastic" scattering. The graphs to the right represent the "hope" that at large energies the processes are dominated by the exchange of Regge trajectories. (c) Illustration of a triple-Regge diagram.

common dominant features, like scaling, but each emphasizes a certain aspect of the situation. Since a very important phenomenological feature of inelastic collision is the cutoff in the transverse momentum distribution, we may try to classify the existing models in two classes:

(i) Models in which the transverse momentum cutoff is a deep consequence of a bootstrap hypothesis (thermodynamic models and dual models).

(ii) Models in which the transverse momentum cutoff is explicitly imposed from outside (diffraction fragmentation models, multiperipheral and Regge-exchange models, field theoretical models, and others).

The following is a list of classes of models, defined in a rather loose way (73C3):

(i) Statistical thermodynamic models. The first version of these models is due to Fermi; more refined versions have been developed later. The reaction products are considered to have originated from a state of statistical equilibrium of "fireballs", each fireball being made of other fireballs including particles and resonances. An intuitive picture of the model may be obtained from the statement that the model considers "hadron matter at the boiling point".

(ii) Diffractive fragmentation models include a number of models, like the "jet", "nova", and "fireball" models. In general these models describe a reaction in terms of the excitation of one or of both incident hadrons; these excited states carry the same quantum numbers of the corresponding incident hadrons. Figure 48 illustrates these models.

(iii) Multiperipheral and Regge exchange models are illustrated by the multiperipheral graph of Fig. 49(a), where the particles in the chain are ordered in such a way so as to minimize momentum transfers. It is this ordering which leads to the transverse momentum cutoff. Thus in a certain sense also this model could be classified as of type (i).

(iv) Field theory models. In these models the asymptotic behavior of the scattering amplitudes is described in perturbation theory by summing the

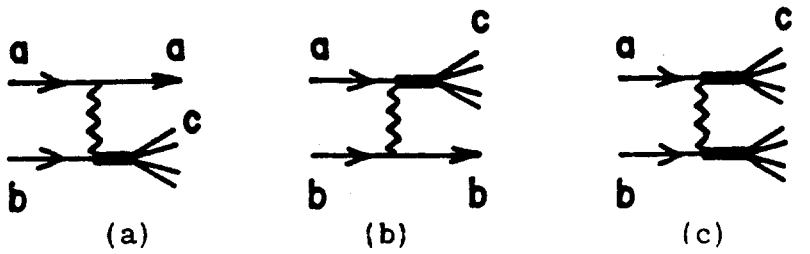

Fig. 48. Illustration of the diffraction dissociation of one particle (a, b) and of both particles (c).

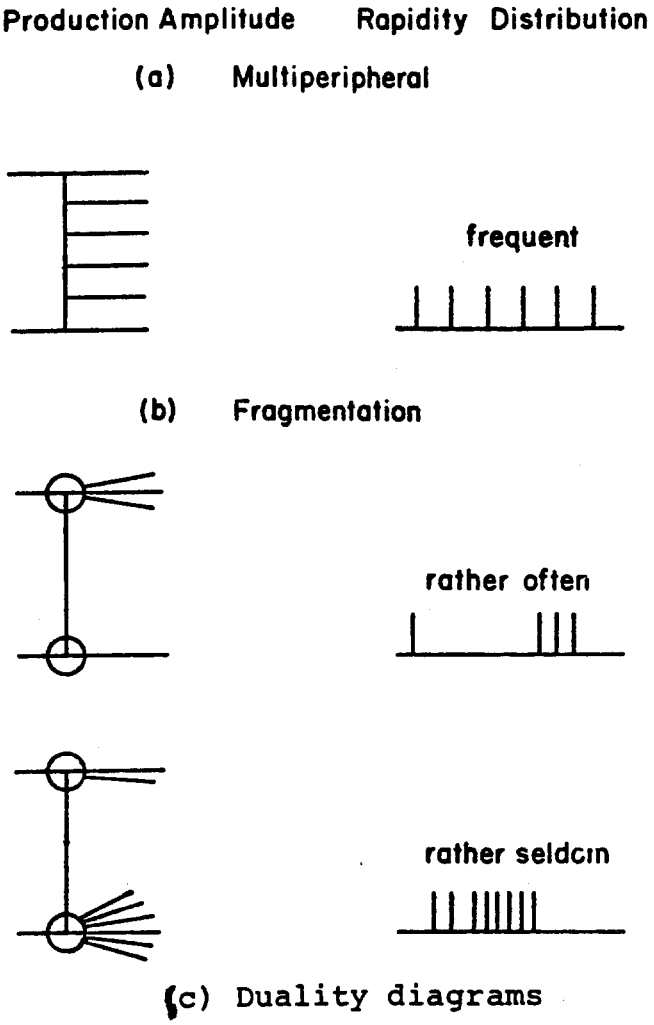

Fig. 49(a). Illustration of one graph for multiperipheral particle production and of the corresponding rapidity distribution. (b) Illustration of the fragmentation model and of the corresponding rapidity distributions. (c) Illustration of duality graphs.

leading terms of an infinite set of diagrams from which one may eventually obtain an eikonal form of the scattering amplitude.

(v) Dual models. The property of duality requires that each term contributing to the scattering amplitude is invariant under a cyclic or anticyclic permutation of the external momenta as illustrated in Fig. 49(c). As originally expressed, resonances in the s channel generate Regge trajectories in the crossed channel. It is moreover conjectured that "normal" trajectories are generated by particles and resonances, while the Pomeranchuck trajectory is built by the non-resonant background part of the amplitude.

Collisions in the central region are easily explained by thermodynamic models. One may oversimplify the picture thinking about a liquid drop at the boiling temperature out of which come the pionization particles in ever increasing number as the energy is increased. But the temperature of the liquid drop and thus the average transverse momentum of the emitted particles remain approximately constant with energy. This highest temperature, one could say the limiting temperature, has a value of about 160 MeV. During the very short time in which all the c.m. energy is concentrated in the small volume of the interaction region (of about 1 fermi), one achieves energy densities and thus mass densities about $(E_{cm}/2)$ larger than inside the nucleon. At the top ISR energy of 62 GeV the mass density reaches the extraordinary value of $\rho = m/v \simeq 10^{16}$ g cm^{-3}, about 30 times larger than inside the nucleon. Of course, in our laboratories these extreme conditions persist for a very short time, of the order of some 10^{-24} sec and we can only observe the more stable structures which survive after the hot interaction region has cooled

down. In this brief time no real statistical equilibrium may be reached, but all kinds of objects are present inside the "hot spot", which may also be called interaction region, fireball, liquid drop, etc. These considerations may have astrophysical significance since the interior of some celestial objects (may be in the black holes, in the pulsars, and in the original fireball from which our universe originated) may have situations analogous to that encountered in our high-energy phenomena. It is remarkable how often the study of the "extremely small" has relations to what happens in the study of the "extremely large".

Fragmentation models give in certain sense a picture complementary to that of the statistical models because they explain the production of particles at forward and backward angles, that is in the fragmentation regions. These models give a vivid picture of what is happening in the peripheral part of the collisions.

Multiperipheral models supplemented with duality bring about a complete description of multiparticle production. From the theoretical point of view they are the models where the general conservation laws of quantum mechanics are more easily incorporated.

Each model emphasizes one aspect of the reality and is able to explain the data in a certain range of the independent variables. The next obvious step is to consider <u>two-component models</u>, obtained by writing the scattering amplitude as the sum of two terms

$$f = f_I + f_{II} \tag{78}$$

where f_I and f_{II} are the amplitudes of one of the previous models. You have heard in the lectures of this school of the success of the two-component model including multiperipheral and diffractive parts. Also the thermodynamic model of Hagedorn et al. may be considered as a two-component model because they added collective motions to the original statistical model (Fig. 50).

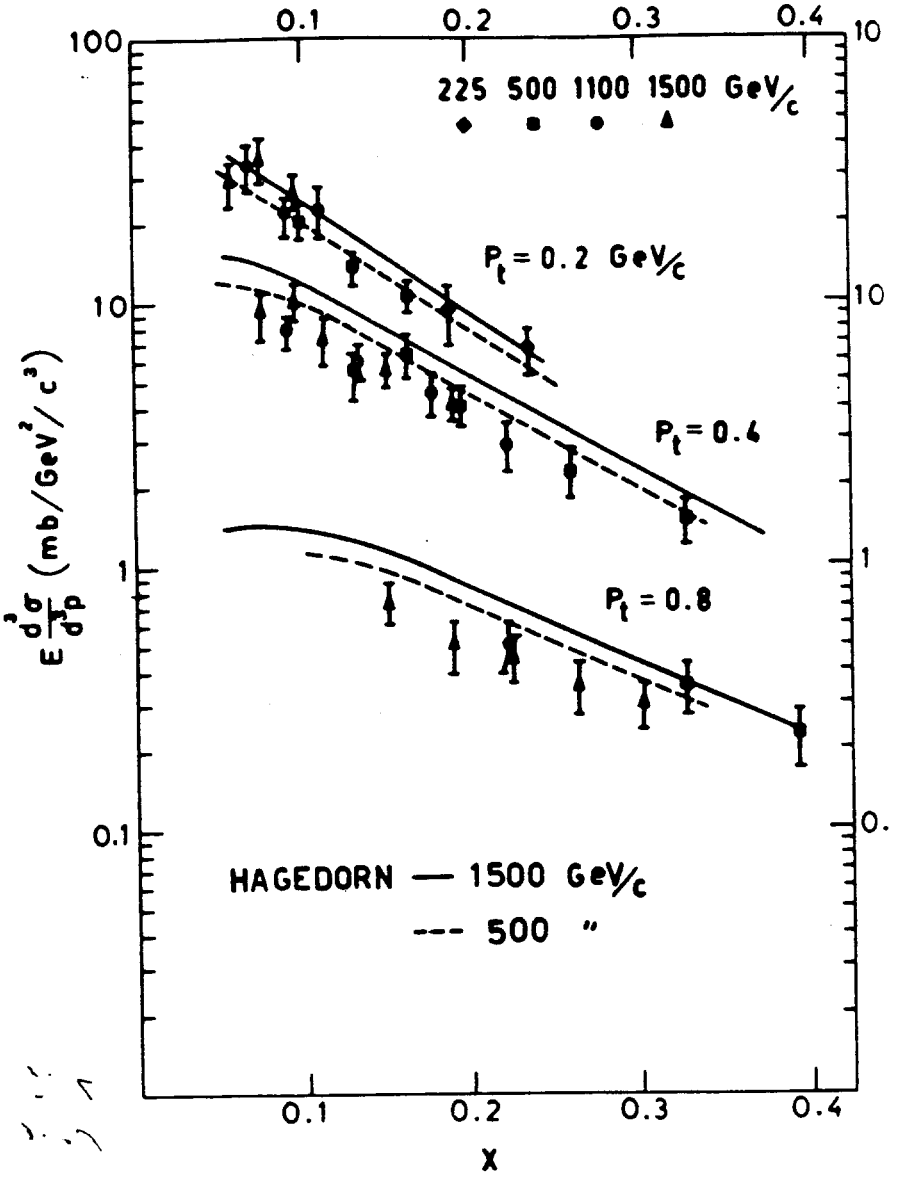

Fig. 50. Comparison of the negative pion production data at the ISR with the predictions of the thermodynamic model of Hagedorn et al.

The first obvious problem the two-component models face is with unitarity and/or double counting.

I must add that from an experimenter's point of view the most convenient model is the thermodynamic model since its authors provide detailed tables of predicted cross sections for each type of particles produced.

7. CONCLUSIONS

Let us review briefly the most important experimental features of particle production which have been established experimentally at c.m. energies above 10 GeV:

1. The exponential cutoff in the transverse momentum.
2. The weak dependence of the average value of the transverse momentum on the type of particles produced, on their rapidity, and on the total c.m. energy.
3. The approximate validity of scaling with a possible 10% deviation between lowest and highest ISR energies.
4. The approach to scaling. With increasing energy the scaling region is reached first in the fragmentation region and at higher energies in the central region. Lighter particles reach their limiting distributions earlier than heavier ones.
5. The existence of large p_t events whose energy dependence is probably large.
6. The approximate validity of the factorization property in (y_{lab}, p_t) with a possible 10% deviation.
7. The pronounced leading particle effects.

8. The existence of short-range correlations with a correlation length of 2 units of rapidity.

9. Approximate noncorrelation of the fragmentations of the two incoming particles.

10. Logarithmic increase of the multiplicities.

The theoretical models discussed in the previous section have given the framework for the explanation of these experimental facts. We now speak with familiarity of fragmentation and central regions, of scaling and limiting distributions, etc. Each model sees the reality from a certain point of view and explain some, but not all of the observed experimental features. The situation is reminiscent of that existing in nuclear physics and in the elastic scattering of elementary particles in the 5- to 20-GeV/c region. It will be difficult to discriminate among the various models of particle production; it may even turn out to be impossible.

We shall end this review with a list of problems which still need an experimental answer and which may shed light on the theoretical interpretation of high energy inelastic collisions:

1. A detailed analysis of single events is lacking.

2. More experiments at large p_t values and in general the study of rare phenomena are needed. In this context one should study the other secondaries associated with the large p_t particles.

3. There is an almost infinite amount of work to do in particle correlations. But one has to ask specific questions like: do long-range correlations exist?

4. To what accuracy scaling and factorization are valid?

5. Further studies of leading particle effects have to be done, in particular those where the resolution is sufficient to study the diffraction-type phenomena of isobar production.

6. Most of the very high-energy works have been done for pp collisions; one should study also the other types of collisions.

8. ACKNOWLEDGMENTS

For the preparation of these lectures I have used extensively the lectures and review papers of A. Bassetto, G. Cocconi, N. Costa, K. Gottfried, M. Jacob, D.R.O. Morrison, K. Potter, and H. Sens. I would like to thank A. Bussière, P. Capiluppi, O. Ferrari, A. M. Rossi, and G. Vannini for their invaluable collaboration.

9. REFERENCES

61 B1 W. F. Baker et al., Phys. Rev. Letters 7, 101 (1961). (Particle production by 10-30-GeV protons incident on Al and Be.)

61 C1 G. Cocconi et al., Lawrence Berkeley Laboratory report UCRL-10022, 1961, p. 167.

62 F1 M. Fidecaro et al., Nuovo Cimento 24, 73 (1962). (Photon production in proton-proton collisions at 23.1 GeV)

62 M1 A. C. Melissinos et al., Phys. Rev. 128, 2372 (1962). (π-meson production in 2.9-BeV p-p collisions)

64 D1 A. N. Diddens et al., Nuovo Cimento 31, 961 (1964). (Particle production in p-p collisions at 19 and 24 GeV/c)

65 D1 D. Dekkers et al., Phys. Rev. 137, 962 (1965). (Experimental study of particle production at small angles in nucleon-nucleon collisions at 19 and 23 GeV/c)

68 R1 J. T. Reed et al., Phys. Rev. 168, 1495 (1968). (Production of K^+ mesons in 2.85 and 2.4 GeV p-p collisions)

69 B1 J. Benecke et al., Phys. Rev. 188, 2159 (1969). (Hypothesis of limiting fragmentation in high energy collisions)

69 B2 Yu. B. Bushnin et al., Phys. Letters 29B, 48 (1969). (Negative particle production at the 70-GeV IHEP accelerator)

69 B3 F. Binon et al., Phys. Letters 30B, 506 (1969). (Further measurements on the production of π^- and K^- mesons and $\bar{p}$ at the 70-GeV IHEP accelerator)

69 F1 R. P. Feynman, Phys. Rev. Letters 23, 1415 (1969). (Very high energy collisions of hadrons.)

70 A1 J. A. Allaby et al., Phys. Letters 33B, 429 (1970). (Comparison of highly inelastic pp and ep scattering)

71 A1 C. W. Akerlof et al., Phys. Rev. D3, 645 (1971). (Inelastic high-energy p-p collisions)

71 A2 Yu. M. Antipov et al., Yad. Fiz. (Sov. J. Nucl. Phys.) 12, 171 (1971). (Observation of antihelium 3)

71 A3 Yu. M. Antipov et al., Yad. Fiz. (Sov. J. Nucl. Phys.) 13, 78 (1971). (Production of negative particles with low momenta by 70-GeV protons)

71 B1 H. Bøggild et al., Nucl. Phys. B27, 1 (1971). (On the production spectrum of pions in high-energy p-p collisions)

71 B2 H. Bøggild et al., Nucl. Phys. B27, 285 (1971). (Some features of particle multiplicities and momentum spectra in inelastic p-p collisions at 19 GeV/c)

71 B3 N. N. Biswas et al., Phys. Rev. Letters 26, 1589 (1971). (Longitudinal and transverse momentum distributions for π^- mesons in 18.5 GeV/c $\pi^{\pm}$p interactions)

71 C1 M. S. Chen et al., Phys. Rev. Letters 26, 1585 (1971). (Single particle distributions of π mesons produced in π^+p, K^+p, p-p, and π^-p collisions at high energies)

71 C2 G. Cocconi, Nucl. Phys. B28, 341 (1971). (Evaluation of the fluxes of secondary particles produced in high-energy proton collisions)

71 N1 G. Neuhofer et al., Phys. Letters B37, 438 (1971). (Transverse momentum distribution of photons produced in p-p collisions at the ISR)

71 R1 L. G. Ratner et al., Phys. Rev. Letters 27, 68 (1971). (Proton-proton inelastic scattering at very high energies)

72 A1 J. V. Allaby et al., CERN 70-12 (1970), and paper presented at the 4th International Conference on High-Energy Collisions, Oxford, 1972)

72 A2 M. G. Albrow et al., Phys. Letters B40, 136 (1972). (Particle production ratios at 21, 31, 45, and 53 GeV in c.m.) Phys. Letters B42, 279 (1972). (The distribution in transverse momentum of 5 GeV/c secondaries produced at 53 GeV in the c.m. system)

72 B1 A. Bertin et al., Phys. Letters B38, 260 (1972). (Negative particle production at the CERN-ISR)

72 B2 A. Bertin et al., Phys. Letters B41, 201 (1972). (Charged particle production ratios at the CERN-ISR for a transverse momentum of 0.4 GeV/c)

72 B3 A. Bertin et al., Phys. Letters B42, 492 (1972). (Charged particle production at the CERN-ISR as a function of transverse momentum)

72 B4 M. Banner et al., Phys. Letters B41, 547 (1972). (Charged particle productions at 90° in the c.m. in very high energy p-p collisions)

72 B5 J. Badier et al., Batavia (1972). (Cross-section measurement for a hyperon beam)

72 C1 G. Charlton et al., Phys. Rev. Letters 29, 515 (1972). (Charged particle multiplicity distribution from 200 GeV/c p-p interactions)

72 C2 J. V. Chapman et al., Univ. of Rochester Report UR-395 (1972). (A measurement of the charged particle multiplicity in p-p collisions at 102 GeV/c)

72 D1 F. T. Dao et al., Phys. Rev. Letters 29, 1627 (1972). (Proton-proton interactions at 303 GeV/c; multiplicity and total cross section)

72 D2 A. N. Diddens et al., Landolt-Börnstein series (1973). (Particle production in p-p interactions)

72 F1 G. Flügge et al., Batavia (1972). (Single and double photon in p-p collisions at the ISR)

72 G1 G. Giacomelli, Proc. of the 7th Rencontres de Moriond (1972). (Charged particle production at the CERN ISR)

72 G2 G. Giacomelli, Proc. of the XVI International Conference on High Energy Physics 3, 219 (1973). (Strong interactions at high energies)

72 H1 J. Hanlon et al., Phys. Rev. D6, 2698 (1972). (A comparison of the reactions p-p → $\pi^{\pm}$ + anything at 28.5 GeV/c and at 1000 GeV/c, and comments on scaling)

72 J1 M. Jacob, Batavia (1972). (Production processes at high energy - theory and experiment)

72 M1 P. K. Malhotra and R. Raghavan, Nuovo Cimento 9A, 75 (1972). (Production of kaons and baryon-antibaryons at a 10-TeV energy)

72 M2 N. J. Mück et al., Phys. Letters 39B, 303 (1972). (Pionization in p-p interactions at 12 and 24 GeV/c)

72 M3 K. C. Moffeit et al., Phys. Rev. D5, 1603 (1972). (Study of the inclusive reaction $\gamma p \rightarrow \pi^- + X$ with polarized γ at 2.8, 4.7, and 9.5 GeV)

72 M4 D.R.O. Morrison, Review of many body interactions at high energy, CERN/DPh 2/72-19.

72 N1 G. Neuhofer et al., Phys. Letters B38, 51 (1972). (Single γ-ray spectra from p-p collisions at c.m. energies from 30 to 50 GeV)

72 P1 J. Pilcher et al., Proc. of the XVI International Conference on High Energy Physics 1, 252 (1973). (Photon production at high energies and scaling)

72 P2 R. S. Panvini et al., Phys. Letters B38, 55 (1972). (Properties of the inclusive π spectrum from p-p collisions; 28.5 GeV/c to about 10^3 GeV/c)

72 S1 S. Stone et al., Phys. Rev. D5, 1621 (1972). (Some aspects of single particle and 2-particle inclusive reactions in 12.7 GeV/c K^+p and 7 GeV/c π^+p collisions)

72 S2 W. M. Sims et al., Nucl. Phys. B41, 317 (1972). (Pion spectra from the reaction p-p → $\pi^{\pm}$ + anything at 28.5 GeV/c)

72 S3 Scandinavian Bubble Chamber Collaboration, Batavia (1972). (The inclusive single particle spectra of π^-, K_S^o, and Λ^o in p-p collisions at 19 GeV/c)

73 A1 M. Antinucci et al., Nuovo Cimento Letters 6, 121 (1973). (Multiplicities of charged particles up to ISR energies)

73 A2 M. G. Albrow et al., Nucl. Phys. B51, 388 (1973). (Longitudinal momentum distributions for positive particles produced at small angles in p-p collisions at c.m. energy of 44.6 GeV)

73 A3 M. G. Albrow et al., Nucl. Phys., to be published. (The spectrum of protons produced in p-p collisions at 31 GeV total energy)

73 A4 M. G. Albrow et al., Phys. Letters B42, 279 (1973); B44, 207 (1973).

73 A5 B. Alper et al., Batavia (1972). (Inclusive particle production in the rapidity range 0 to 1 at the CERN ISR)

73 A6 B. Alper et al., Phys. Letters B44, 521 (1973). (Production of high transverse momentum particles in p-p collisions in the central ragion at the CERN ISR); Phys. Letters B44, 527 (1973). (Particle composition at high transverse momenta)

73 A7 J. Anderson et al., Phys. Letters, to be published. (Energy dependence of the inclusive cross section for the reaction $\pi^+ d \rightarrow \pi^- + X$ at large transverse momenta)

73 A8 M. Antinucci et al., Proc. of the 1973 Vanderbilt International Conference. (Particle production at medium angles at the CERN ISR)

73 A9 V. V. Ammosov et al., Nucl. Phys. B58, 77 (1973). (Charged particle multiplicity distributions for 33.8 GeV/c $k^- p$ and 50 GeV/c $\pi^- p$ interactions)

73 A10 M. G. Albrow et al., Nucl. Phys. B56, 333 (1973). (Negative particle production in the fragmentation region at the CERN ISR)

73 A11 H. Abarbanel, Lectures at the 1973 Canadian Institute of Particle Physics. (Model building in hadron physics)

73 A12 K. Abe et al., 1973 Meeting of the APS Division of Particles and Fields, Berkeley, California, August 13-17. (Measurement of $pp \rightarrow p + X$ between 50 and 400 GeV/c)

73 B1 W. Bartel et al., 1973 Heidelberg Conference of German Physical Society. (Study of the inclusive reaction $p\text{-}p \rightarrow n + X$ at the CERN ISR)

73 B2 M. Banner et al., Phys. Letters B44, 537 (1973).

73 B3 G. Bellettini et al., Phys. Letters B45, 69 (1973). (Experimental test of limiting fragmentation at the ISR)

73 B4 D. Bogert et al., Vanderbilt Conference, 1973. (π^-p interactions at 205 GeV/c)

73 B5 O. Balea et al., Budapest preprint KFKI-73-17 (1973). (Production of γ quanta in π^-N interactions at 40 GeV/c)

73 B6 S. Barish et al., National Accelerator Laboratory Report NAL-Conf-73/25-EXP and 1973 Aix-en-Provence Conference. (pp interactions at 205 GeV/c).

73 C1 D. C. Carey et al., 1973 Vanderbilt Conference and 1973 Aix-en-Provence Conference. (Large transverse momentum production of γ rays at NAL)

73 C2 S. Childress et al., Phys. Rev. Letters, to be published. (Inelastic p-p scattering at 200 GeV)

73 C3 G. Costa and P. Pasti, Revista Brasileira de Fisica (1973), to be published.

73 C4 P. Capiluppi et al., Nucl. Phys., to be published. (High energy particle production as function of momentum transfer)

73 C5 CERN-Columbia-Rockefeller collaboration, F. W. Büsser et al., 1973 Vanderbilt Conference. (Production of π^0 at large transverse momenta)

73 C6 Y. Cho et al., Phys. Rev. Letters 31, 413 (1973). (Inclusive π^- distributions from 205 GeV/c p-p interactions)

73 C7 D. Cline et al., Phys. Rev. Letters 31, 491 (1973). (High-transverse momentum secondaries and rising total cross sections in cosmic-ray interactions)

73 C8 C. Quigg, Lectures at the 1973 Canadian Institute of Particle Physics. (Two-component models of particle production)

73 C9 J. W. Cronin et al., Paper presented at the 1973 Aix-en-Provence Conference.

73 D1 H. Dibon et al., Phys. Letters, to be published. (Rapidity correlations in inclusive two-particle production at ISR energies)

73 D2 F. T. Dao et al., Phys. Rev. Letters 30, 34 (1973). [Proton-proton interactions at 303 GeV/c; inclusive measurement of $\Delta^{++}(1236)$ resonance]

73 D3 F. T. Dao et al., National Accelerator Laboratory Reports NAL-Pub-73/21-EXP and NAL-Conf-73/31-EXP. (Proton-proton interactions at 303 GeV/c; inclusive studies of γ, K_S^o, and Λ^o production)

73 D4 M. Deutschmann et al., Nucl. Phys. B, to be published. (Transverse spectra in $\pi^{\pm}p$ and K^-p interactions between 8 and 16 GeV/c)

73 D5 F. T. Dao et al., Phys. Letters B45, 73 (1973). (pp interactions at 303 GeV/c: production angle distribution)

73 D6 F. T. Dao et al., National Accelerator Laboratory Report NAL-Pub-73/37-EXP, to be published. (Study of charged multiplicity distributions in high-energy collisions)

73 D7 F. T. Dao et al., National Accelerator Laboratory Report NAL-73/20-EXP. (pp interactions at 303 GeV/c: tests of scaling in single particle $\pi^{\pm}$ and proton distributions)

73 E1 J. Engler et al., to be published. (Measurement of inclusive neutron spectra from p-Be up to 24 GeV/c incident momentum)

73 E2 J. Engler et al., to be published.

73 F1 France-USSR collaboration, 1973 Vanderbilt Conference. (Inclusive neutral kaon and lambda production in 69 GeV pp interactions); (Photon production in 69-GeV pp interactions)

73 H1 V. Hungerbuehler et al., National Accelerator Laboratory Report NAL-Pub-73/16-EXP, to be published. (Σ^- production in high-energy proton interactions)

73 R1 L. G. Ratner et al., to be published. (Measurement of p-p inclusive cross sections at very high energy)

73 S1 F. Sannes et al., Phys. Rev. Letters 30, 766 (1973). (Study of the inclusive reaction $p + p \rightarrow p + X$ between 40 and 260 GeV/c using an internal H_2 jet target)

73 S2 P. Slattery et al., 1973 Vanderbilt Conference. (pp collisions at 102 GeV/c)

TABLE 4.1 Summary of models, types of experiments, and the predictions made by various models.

Experiment	Model					Beam energy region
	(a) Mueller analysis	(b) Multiperipheral	(c) Diffractive fragmentation	(d) Statistical thermodynamical	(e) Cheng-Wu	
(1) Average multiplicity $\langle n(E)\rangle$	$\langle n(E)\rangle = a \ln E + b$		No prediction; can accommodate any reasonable behavior	$\langle n\rangle$ grows faster than $\ln E$	$\langle n\rangle \propto s^a$, $a>0$	$E>E_p$
(2) Multiplicity distribution $P(n)$	No prediction	Roughly Poisson	$P(n) \propto n^{-3}$ if $\langle n\rangle \propto \ln E$	No prediction	?	$E>E_p$
Partial cross sections $\sigma_n(E)$	No prediction	$(K \ln s)^{n-2} s^{-K}/(n-2)!$, $K = 2-2\alpha_M(0) \approx 1$	Constant	No prediction	?	$E>E_p$
(3) One-particle spectra: limiting fragmentation?	Yes	Yes	Yes	Yes	No; $\rho(q) \propto s^a$	$E>E_f$
(4) One-particle spectra: central plateau?	Yes	Yes	No prediction; can be accommodated	Not in present version; can be accommodated	Yes	$E>E_p$
(5) One-particle spectra: factorization in fragmentation regions	Yes	Yes	?	No prediction	?	$E>E_f$
(6) One-particle spectra: factorization in plateau region	Yes	Yes	No	No prediction	?	$E>E_p$
(7) Two-particle spectra: correlations?	Only short-range correlations, if Regge poles≫Regge cuts.		No prediction	No prediction	?	$E>E_f$
(8) Diffraction dissoc. into high missing mass	$\propto g_{PPP}^2$, triple Pomeron coupling	g_{PPP} small or zero	"Favored"	No prediction	?	
(9) $\sigma_{tot}(E)$	$\sigma \propto$ const. or $s^{-\epsilon}$, $\epsilon \ll 1$.		Constant	No prediction	$\sigma \propto \ln^2 s$	